Western Washington University
Western CEDAR

WWU Graduate School Collection | WWU Graduate and Undergraduate Scholarship

Fall 2018

The Effects of Forecasted Climate Change on Mass Wasting Susceptibility in the Nooksack River Basin

Kevin Knapp
Western Washington University, k6knapp@gmail.com

Follow this and additional works at: https://cedar.wwu.edu/wwuet

 Part of the Geology Commons

Recommended Citation

Knapp, Kevin, "The Effects of Forecasted Climate Change on Mass Wasting Susceptibility in the Nooksack River Basin" (2018). *WWU Graduate School Collection*. 807.
https://cedar.wwu.edu/wwuet/807

This Masters Thesis is brought to you for free and open access by the WWU Graduate and Undergraduate Scholarship at Western CEDAR. It has been accepted for inclusion in WWU Graduate School Collection by an authorized administrator of Western CEDAR. For more information, please contact westerncedar@wwu.edu.

The Effects of Forecasted Climate Change on Mass Wasting Susceptibility in the Nooksack River Basin

By

Kevin L. Knapp

Accepted in Partial Completion
Of the Requirements for the Degree
Master of Science

ADVISORY COMMITTEE

_____

Chair, Dr. Robert Mitchell

_____

Dr. Doug Clark

_____

Dr. Eric Grossman

GRADUATE SCHOOL

_____

Dr. Gautam Pillay, Dean

Master's Thesis

In presenting this thesis in partial fulfillment of the requirements for a Master's degree at Western Washington University, I grant to Western Washington University the non-exclusive royalty-free right to archive, reproduce, distribute, and display the thesis in any and all forms, including electronic format, via any digital library mechanisms maintained by Western Washington University.

I represent and warrant this is my original work and does not infringe or violate any rights of others. I warrant that I have obtained written permissions from the owner of any third party copyrighted material included in these files.

I acknowledge that I retain ownership rights to the copyright of this work, including but not limited to the right to use all or part of this work in future works, such as articles or books.

Library users are granted permission for individual, research and non-commercial reproduction of this work for education purposes only. Any further digital posting of this document requires specific permission from the author.

Any copying or publications of this thesis for commercial purposes, or for financial gain, is not allowed without my written permission.

Kevin L. Knapp

November 19, 2018

The Effects of Forecasted Climate Change on Mass Wasting Susceptibility in the Nooksack River Basin

A Thesis
Presented to
The Faculty of
Western Washington University

In Partial Completion
Of the Requirements for the Degree
Master of Science

By
Kevin L. Knapp
November 2018

Abstract

The Nooksack River in Whatcom County, Washington is an essential fresh water resource for industry, agriculture, municipalities and serves as vital fish habitat. Like many mountainous watersheds in the western Cascades, the Nooksack Basin is susceptible to shallow mass wasting and debris flows because of its steep slopes, young glaciated terrain, and storms with high intensity precipitation. Understanding how projected reductions in snowpack and increased winter rainfall will affect mass-wasting susceptibility in the Nooksack basin is important, because sediment produced mass wasting will jeopardize valuable aquatic and fish habitat, increase flooding risk in the Nooksack River, and affect estuarine and coastal dynamics.

With a projected 60% decrease in snowpack and increase in the snowline elevation by the 2075 climate normal, there will be an increase in exposed forest roads, harvestable forest areas, and previously mapped landsides, which are all documented to increase sediment delivery to streams. Retreating glaciers will produce at least 2 km^2 of exposed moraines, which have the potential to erode, fail and provide additional sediment to streams, especially during large storm events coinciding with minimum snowpack during the fall and early spring seasons. I applied a static infinite-slope ArcGIS model and a dynamic, probabilistic mass-wasting model integrated into the Distributed Hydrology Soil Vegetation Model (DHSVM) to the Nooksack River watershed to determine areas susceptible to mass wasting into the 21st century. Susceptibility maps produced by the models indicate an increase in regions susceptible to slope failure during the winter months in snow free areas at higher elevations later in the 21st century. Slope failure susceptibility increased with soil saturation, which is anticipated with higher intense winter rainfall events. Slopes greater than about 30^o with thick regolith deposits and lower soil mechanical strength, e.g., sand, loamy sand, sandy loam, silt, moraines, glacial outwash and former landslide deposits were correlated with higher mass-wasting susceptibility. The simpler static ArcGIS infinite-slope model yielded comparable results to the more complex probabilistic method integrated into the DHSVM for identifying areas susceptible to mass wasting.

Acknowledgements

My research was supported by the Nooksack Indian Tribe, the Geology Department at Western Washington University, and the Western Washington University Office of Research and Sponsored Programs.

I would like to thank my advisor and thesis committee chair, Robert Mitchell, for his absolute dedication to helping me through this project and his support during my time at WWU. I am very grateful for the guidance of Dr. Mitchell, who has provided the necessary coursework and tools for myself and other students to progress into proficient geoscientists. Thank you to Doug Clark for providing productive feedback during the writing process, as well as valuable insight into components of my project through the lens of a geomorphologist. Thank you to Eric Grossman, who provided meaningful feedback, observations and insights during my project. My committee members were willing to lend an ear when needed during their busy schedules, and I am very appreciative of this. I am grateful for research funding provided by the Nooksack Indian Tribe, which was essential to the success of my project. The support of Oliver Grah and Jezra Beaulieu of the Nooksack Indian Tribe was indispensable, and I am grateful to be a part of research working towards assisting local salmon populations and communities. Special thanks to Ryan Murphy for his previous Master's thesis work and for providing invaluable digital data pertaining to the Nooksack Basin. To my WWU cohort that I had the opportunity to grow with during my time at WWU, I thank you for your sense of community and ability to appreciate the graduate school experience.

Table of Contents

Abstract.....iv

Acknowledgements.....v

List of Tables.....viii

List of Figures.....ix

1.0 Introduction.....1

2.0 Background.....3

2.1 Geologic Setting.....3

2.2 Topography.....5

2.3 Regional Hydrology and Climate.....6

2.4 Climate Projections.....7

2.5 Forest Harvesting and Hillslope Processes.....8

2.6 Previous Work on Mass Wasting in the Nooksack Watershed.....9

2.7 Slope Stability.....10

2.7.1 Overview.....10

2.7.2 Infinite-Slope Equation.....10

3.0 Methods.....13

3.1 Digital Watershed Characteristics.....13

3.1.1 Digital Elevation.....13

3.1.2 Surface Geology and Soil.....14

3.1.3 Landcover.....16

3.2 Forecasted Snow and Landscape Change.....17

3.3 ArcGIS Infinite-Slope Modeling.....18

3.3.1 ArcGIS Model.....18

3.3.2 Static Mechanical Properties.....18

3.3.3 Modeling Scenarios.....19

3.4 DHSVM Infinite-Slope Modeling.....20

3.4.1 DHSVM Hydrology Model.....20

3.4.2 DHSVM Sediment Module.....20

3.4.3 Probabilistic Mechanical Properties.....22

3.4.4 Modeling Scenarios 23
3.5 Statistical Analysis 23
4.0 Results 25
4.1 Forecasted Snow and Landscape Change 25
4.2 Infinite-Slope Analysis 26
4.2.1 Static (ArcGIS) Infinite-Slope Results 26
4.2.2 DHSVM Infinite-Slope Results 27
5.0 Discussion 31
5.1 Forecasted Snowlines and Sediment Source Increases 31
5.2 Static Modeling Sensitivity and Uncertainty 32
5.3 Forecasted Storm Effects on Mass Wasting 34
5.4 Mass-Wasting Susceptibility Mapping 36
6.0 Conclusion 37
7.0 References 39
8.0 Tables 48
9.0 Figures 67

List of Tables

Table 1. Basin and glacial areas in the upper basins of the Nooksack River.....48
Table 2. Mechanical soil characteristics used in static infinite-slope modeling 49
Table 3. NOAA to DHSVM landcover classifications 50
Table 4. Mechanical vegetation characteristics used in static and probabilistic modeling...51
Table 5. Probability distributions of mechanical soil characteristics.....52
Table 6. Landscape changes from historical to projected 2075 median snow coverages.....53
Table 7. Static modeling results of susceptible areas at 10 m and 1 m resolutions 54
Table 8. Area of digitized moraine deposits for historical and projected landscapes.....55
Table 9. InfoVal weights from static results 56
Table 10. Cumulative precipitation values for fall storms 57
Table 11. Cumulative precipitation values for winter storms 58
Table 12. Areal snow coverage during DHSVM storm events.....59
Table 13. Saturation extent resulting from DHSVM storm events 60
Table 14. Area of failure probabilities for historical and projected storm events.....61
Table 15. Change in area of failure probabilities between historical and projected storm Events.....62
Table 16. InfoVal weights of saturation percent and surficial unit classes from winter storms.....63
Table 17. InfoVal weights of slope, soil depth, and vegetation classes from winter storms.....64
Table 18. InfoVal weights from fall storms 65
Table 19. Area of very high susceptibility derived from InfoVal weights for storm events 66

List of Figures

Figure 1. Nooksack River basin study area map.....67
Figure 2. Elevation of the upper Nooksack Basin 68
Figure 3. LiDAR derived slope map of the upper Nooksack Basin 69
Figure 4. Digitized landslide deposits within the upper Nooksack Basin 70
Figure 5. Soil depth raster for the upper Nooksack Basin 71
Figure 6. Soil coverage shapefiles used for the upper Nooksack Basin 72
Figure 7. Surficial unit shapefiles used for the upper Nooksack Basin 73
Figure 8. NOAA landcover classification raster.....74
Figure 9. Resampled DHSVM landcover classification raster 75
Figure 10. ModelBuilder workflow of static infinite-slope model 76
Figure 11. Modeled median snow coverages and elevation bands in the Upper Nooksack Basin 77
Figure 12. Roads and harvestable forest areas with median historical and projected snow coverages.....78
Figure 13. Digitized landslide deposits with median historical and projected snow coverages.....79
Figure 14. Static modeling results of historical scenario 80
Figure 15. Static modeling results of projected scenario 81
Figure 16. Static modeling results with historical and projected moraine deposits and glacier extents 82
Figure 17. Failure probabilities associated with the January 2009 storm event 83
Figure 18. Failure probabilities associated with the January 2089 storm event 84
Figure 19. Failure probabilities associated with the December 2096 storm event 85
Figure 20. Failure probabilities associated with the October 2003 storm event.....86
Figure 21. Failure probabilities associated with the October 2089 storm event.....87
Figure 22. Very high susceptibility associated with the January 2009 storm event 88
Figure 23. Very high susceptibility associated with the January 2089 storm event 89
Figure 24. Very high susceptibility associated with the October 2003 storm event.....90
Figure 25. Very high susceptibility associated with the October 2089 storm event.....91

Figure 26. Very high susceptibility and failure probability areas from the January 2089 storm event.....92
Figure 27. Very high susceptibility associated with the December 2096 storm event and static modeling results.....93

1.0 Introduction

The forecasted loss in snowpack area and increase in snowpack elevation into the 21st century have important implications for runoff and mass-wasting susceptibility. Each year, rivers of the western Cascades and Olympic Mountains deliver millions of tons of sediment to the Salish Sea (Czuba et al., 2011). Common sources of sediment include glaciers, mass wasting, forestry roads, erosion from farm fields, streambank erosion, and resuspension of sediment previously deposited on streambeds (Anderson et al., 2018; Brown, 2011). In high elevations, snow-dominated zones typically mitigate runoff as a result of the refreezing of water deep within the snowpack, or snow can attenuate percolation through the snowpack (Brunengo et al., 1992). In the Pacific Northwest (PNW), evidence shows that sediment input to rivers, including the Nooksack River, is expected to increase in the upcoming century as a result of continued glacier recession, a smaller snowpack area, increased winter rainfall and runoff, and more mass wasting (Moore et al., 2009; Mote and Salathé Jr., 2010; Lee et al., 2016; Mitchell et al., 2016). This is problematic, because an increase in sediment input within the Upper Nooksack basin will jeopardize valuable aquatic and fish habitat and historical restoration efforts, river morphology and flooding risk in the Nooksack River, and affect estuarine and coastal dynamics. Currently, there has not been an attempt to analyze the mass-wasting susceptibly in the Nooksack basin as the result of forecasted loss in snowpack area into 21st century.

The Nooksack River originates on the northern and western slopes of Mt. Baker in the North Cascades mountain range of Washington State and drains an approximately 2300 km^2 watershed into Bellingham Bay in the Salish Sea (Figure 1). The Nooksack River is a critical resource that provides valuable habitat for a variety of endangered salmon species. Fish species, including salmon, require suitable stream temperatures, stream flows and sediment regimes to flourish. Because of their ectothermic makeup and spawning process, salmon are particularly vulnerable to climate change (Isaak et al., 2010). Effects of climate change on streamflow, stream temperature, and sediment could potentially degrade the physiology, growth and distribution of salmon species in the Nooksack basin. In particular, the amount of suspended sediment within a river can affect the overall health of salmon. Elevated turbidity, an indicator of fine sediment concentration, are associated with reductions in egg-fry survival and have the potential to modify the behavior of rearing and holding salmon, resulting in the increased mortality and/or reduced productivity of salmon habitats (Brown, 2011; EPA, Nooksack Indian

Tribe and Tetra Tech, 2015). Therefore, it is essential to assess the potential impacts of increased sediment production in order to structure planning aimed towards protecting future salmon populations. Although bedload sediment affects redd and riffles of fish species and will likely increase as a result of the changing climate, bedload is more difficult to quantify and is not assessed in my project (Lee et al., 2016).

The value of the Nooksack River as a fresh water resource and valuable habitat for endangered salmon species has caused water managers and stakeholders to voice concern over the climate variability of the basin and how future climate change might affect the region's snowpack, glaciers, stream functions and fish habitats. Historically, streamflow in the Nooksack River basin has been largely controlled by fall and winter precipitation, with the timing of spring snowmelt and glacial meltwater being determined by antecedent snowpack and seasonal weather. As the climate warms, changes in the ratio of rain to snow precipitation, in the timing and amount of total precipitation, timing of snowmelt, and seasonal changes in soil moisture content will all modify timing and magnitude of streamflow (Dickerson-Lange and Mitchell, 2013). Historical winter snow coverage (1981 – 2010) is generally restricted to elevations above 500 to 1000 m in the Nooksack River basin. With winter snowpack predicted to decrease in area and increase in elevation compared to historical averages, the area available for rapid rainfall-driven runoff and mass wasting is expected to increase (Mitchell et al., 2016).

Exposed landscapes resulting from glacier recession are another potential source of sediment input to the Nooksack River. Several glacier mass balance and modeling studies in the Nooksack Basin and the PNW have documented the significant historical retreat of glaciers, with retreat expected to continue as the climate continues to warm (Pelto and Brown, 2012; IPCC, 2013; Riedel et al., 2015; Murphy, 2016). Glacier recession exposes large sources of unstable sediment, including mass failures from over-steepened valley walls (Moore et al., 2009). Mass failures can be generated on moraines that result from glacier retreat, exposing unconsolidated sediments that are vulnerable to both rapid and extensive erosion and entrainment into fluvial systems (Leggat et al., 2015). Varying amounts of unconsolidated materials are present in many of the headwaters of streams in the North and Middle Fork basins, which are stored in moraines, river terraces, and debris flow deposits (United States Department of Agriculture, 2006). Erosion and mass wasting of these unconsolidated deposits comprise an important source of both course and fine sediment, with additional fine sediment being sourced from glacial meltwater. The

retreat of glaciers results in a lowered shear strength and removal of lateral support of adjacent material, which can lead to especially large mass-wasting events (Tucker et al., 2014; Nielsen and Grah, 2015). Because of the potential effects of receding glaciers and decreased snowpack on sediment mobilization in the basin, the timing, magnitude, and turbidity of streamflow in the Nooksack River is anticipated to change in impactful ways throughout the 21st century.

The focus of my study is restricted to the upper Nooksack sub-basins, which is the dominant sediment source for the lower river and is susceptible to naturally occurring mass wasting as a result of its geology, lithology, and glacial history (Anderson et al., 2018; Weatherly, 2005). The steep slopes and high amounts of precipitation lead to frequent shallow mass-wasting events in the upper Nooksack River, increasing the likelihood for flooding and the amount of river sedimentation. The potential effects of forecasted climate changes on mass wasting in the upcoming decades have not been fully explored. As a proxy for predicting an increase in sediment fluxes to streams, I applied static and probabilistic infinite-slope numerical models to evaluate the potential effects of forecasted climate change on mass-wasting events in the Nooksack River basin. I also assess the models' overall effectiveness as tools for mass-wasting susceptibility mapping.

2.0 Background

2.1 Geologic Setting

Bedrock geology in the Nooksack basin consists of sedimentary, metamorphic, and igneous rocks (Tabor et al., 2003). Although shallow mass-wasting events are the focus of my study, several bedrock units within the upper Nooksack basin are susceptible to deep-seated landslide failures, providing chronic and episodic sediment inputs into rivers and streams. The Eocene Chuckanut Formation, composed of sandstone, mudstone, siltstone, and minor coal seams, has a propensity for deep-seated landsliding in the region due to wide-spread and abundant discontinuities (Malick, 2018). In the South Fork Nooksack Basin, deep-seated landslides are common on slopes underlain by early Cretaceous Darrington Phyllite, as foliation associated with the phyllite and schist compositions can lead to widespread cracking and pull-apart blocks (Tabor et al., 1989). The area has experienced both strike-slip and extension faulting since the Cretaceous Period, with the location of these faults and rock types in the basin coinciding with both major and minor landslides (United States Department of Agriculture,

2006). Historically, there have also been various types of debris flows generated by volcano eruption or collapse, glacial outburst floods, and moraine mass wasting (Tucker et al., 2014). Holocene-aged lahars and large debris flows have been deposited in the Middle Fork basin. For example, in May 2013, a large debris flow (~100,000 m^3) was initiated on a young moraine near the toe of the Deming Glacier, with the resulting slug of sediment affecting turbidity in the entire reach of the river (Tucker et al., 2014). Smaller-volume debris flows of volcanic clastic sediments are recurrent and deposited as terraces in upper tributary stream valleys, with recent events occurring in Rocky Creek and Rainbow Creek (Tucker et al., 2014; Mount Baker Volcano Research Center, 2018)

The major landforms that control stream and hillslope processes in the upper Nooksack watershed are mainly the result of the most recent ice-sheet advance in combination with local postglacial modification of the landscape (Booth et al., 2003). The last major glaciation of Whatcom County culminated approximately 15,000 - 20,000 years ago in the late Pleistocene, when thick ice sheets related to the advance of the Cordilleran ice sheet filled valleys in the Nooksack basin, covering the region up to at least 2000 m above mean sea level (Booth, 1991). Advancement and retreat of this ice sheet deposited a variety of glacial sediments in the upper Nooksack River basin. These glacial sediments are collectively named drift, which refers to any deposit of glacial origin, and can be divided into several units: outwash deposits – well-sorted sand and gravel deposited by streams flowing from advancing and retreating ice sheets; and till deposits – unsorted sand, gravel, silt and clay deposited below the ice sheet (Booth et al., 2003). Mount Baker remains moderately glaciated today, hosting the largest contiguous network of glaciers in the North Cascades mountain range, approximately 3400 hectares, in the North and Middle Fork basins (Pelto and Brown, 2012; Murphy, 2016). Alpine glaciers on Mt. Baker have modified the landscape since the last major glaciation and deposited moraines - poorly-sorted sand, gravel, silt and boulders deposited at the edges and terminus of glaciers upon their advancement and retreatment (Booth et al., 2003). Extensive, thick alluvial deposits and series of river terraces are found in the more gently sloping valleys of each sub-basin, as streams have been actively down-cutting since the last glaciation. Characterizing the location and properties of these recent geologic deposits is critical to assessing slope susceptibility, as the stratigraphy of glacial and unconsolidated deposits on sloping hillsides is intimately associated with mass

wasting and landslide events, and as a result sediment production to streams and rivers (Booth et al., 2003).

Recent landslide hazard mapping on Mt. Baker was conducted around glaciers on Mt. Baker and to provide insight on the implications for sediment transport in the Nooksack River (Nielsen and Grah, 2015). Landforms and geomorphic events were identified from 1940 to 2013 using historical airphotos and GIS layers. A total of 294 mass-wasting landforms were identified and mapped and digitized into a GIS. The highest hazard areas were identified along the toes of receding glaciers and steep slopes located on cirque walls, arêtes, and horns (Nielsen and Grah, 2015). While many types of landslides were identified, debris flows were found to be the dominant mass-wasting process on Mt. Baker, making up almost 70% of the total landslide counts documented. Most mass wasting occurred between 1986 and 1991, coinciding with a time when glaciers were experiencing a faster rate of recession compared to previous years (Nielsen and Grah, 2015). Moraines at the toes of the Deming and Mazama glaciers were classified as extremely active and are thought to contribute large amounts of sediment to the North and Middle Forks of the Nooksack River, respectively (e.g., Tucker et al., 2014).

2.2 Topography

The upper Nooksack River basin (~1550 km^2) consists of three major forks, the South Fork Nooksack (South Fork), Middle Fork Nooksack (Middle Fork), and North Fork Nooksack (North Fork) that converge as the river exits the Cascade foothills near Deming, WA. Elevation in the upper Nooksack basin ranges from approximately 67 meters near Deming, WA, to 3286 meters at the summit of Mt. Baker (Figure 2). The North and Middle forks contain much higher elevations in comparison to the South Fork; approximately 49% of both the North and Middle Fork basins are greater than 1000 m above sea level, while the South fork only has approximately 25% above this elevation (Table 1). Peak elevations in the North and Middle forks reach over 3000 m, while the maximum elevation is just over 2000 m in the South Fork. The difference in elevation results in a lack of glaciers in the South Fork and approximately 25.8 km^2 and 7.6 km^2 of glacial ice in the North and Middle forks, respectively (Table 1). Channel gradients for the three forks are relatively steep, exceeding 5% in the mid to upper reaches and decreasing to around 0.5% or less near Deming (Weatherly, 2005). Hillslopes within the basin

vary from nearly flat in the river valleys to greater than 80 degrees, with the majority of steep canyons adjacent to the river channels having slopes between 30 and 45 degrees (Figure 3).

2.3 Regional Hydrology and Climate

The maritime climate of the PNW produces mild winters having long periods of light to moderate intensity precipitation, and generally dry and cool summers. The PNW is also strongly influenced by climatic events such as the Pacific Decadal Oscillation and El Niño Southern Oscillations (Mantua and Hare, 2002; Deser et al., 2012). The Nooksack basin is classified as a transient rain-snow basin, i.e., basins having an average winter temperature within about 5°C of freezing and a ratio of snow water equivalent (SWE) to precipitation of 0.1 – 0.4 from October – March (Dickerson-Lange and Mitchell, 2013). Precipitation can change from snow to rain over small temperature increases in transient basins, so they are particularly vulnerable to warming climates (Mauger et al., 2015; Murphy, 2016). The topographic relief of the Nooksack River basin causes extensive climate variability due to orographic effects. During the 1981–2010 climate normal, average annual precipitation varied from about 820 mm near sea level to 5655 mm near the summit of Mt. Baker, and had a basin mean of about 2290 mm (PRISM Climate Group, 2017). Extreme precipitation events are possible, an example being the U.S. record snowfall of 28.96 m at the Mt. Baker Ski Area (elevation of 1280 m) occurred during the 1998 – 1999 winter (Mass, 2015). The observed mean annual temperatures in the PNW have increased 0.6 – 0.8°C since the early 20th century, while precipitation during the same time period has increased overall, but these trends are small in comparison to natural variability (Mote et al., 2014).

The melting of seasonal snowpack in the North Cascades provides substantial spring and summer flows for all three forks, while glaciers located within the North and Middle Fork basins supply late summer flow (Dickerson-Lange and Mitchell, 2013; Murphy, 2016). Because of lower elevations in the glacier free South Fork basin, streamflow is dominated by snowmelt and rain. From 2006 to 2017 the average annual discharge of the Nooksack River at North Cedarville, WA, located at the western edge of the upper basin, was approximately 107 cubic meters per second (cms; Figure 1; United States Geological Survey, 2018). Historical peak flows are attributed to Pacific storms that generate rain-on-storm events during the late fall and early winter, e.g., a maximum discharge of approximately 1610 cms was recorded on November 10,

1990 at Ferndale, WA (Dickerson-Lange and Mitchell, 2013; United States Geological Survey, 2018).

High intensity storms and rain-on-snow events that trigger many slope failures generally occur between October and March. The duration and magnitude of these high intensity storms is variable, while most are characterized by a significant amount of precipitation falling in a period of less than one day to three days, with three-day cumulative precipitation being identified as a landslide initiating threshold (Chleborad et al., 2006). In the early 1980s, El Niño caused greater-than-normal precipitation in mountainous regions and a significant increase in landslide activity (Turner and Schuster, 1996; Lu and Godt, 2013). Very saturated conditions result in positive pore water pressures that decrease the shear strength of unconsolidated deposits triggering mass-wasting events (Sidle and Bogaard, 2016).

2.4 Climate Projections

The variability in topography throughout Washington State produces a range of local climate zones and precipitation received throughout the year. Climate change is expected to affect each of these climate zones differently (Salathé Jr. et al., 2010). The PNW region is projected to warm rapidly during the 21st century relative to 20th century average climate. Global climate models (GCMs) used in the International Panel on Climate Change (IPCC) Fifth Assessment Report project temperatures to increase as much 1.7 – 4.7°C for the 2050s relative to 1950 – 1999 (Snover et al., 2013). In the Nooksack River basin, average winter temperatures for the 2050s are projected to increase by 2.2°C for moderate carbon emission scenarios and 2.8°C for severe carbon emission scenarios relative to 1970 – 1999 (Morgan et al., 2017).

Climate projections for the PNW anticipate seasonal changes in precipitation, with increases during the winter months and decreases during the summer months (Mote and Salathé Jr., 2010; Abatzoglou et al., 2014; Nature Conservancy and the Climate Impacts Group, 2016). The change in annual amount of precipitation is projected to be small, with more precipitation falling as rain rather than snow and summer precipitation projected to decrease by as much as 30% by the end of this century as greenhouse gas emissions continue to increase (Mote and Salathé Jr., 2010; Mote et al., 2014). Extreme rainfall events are anticipated to increase in intensity and frequency, with models stating the heaviest 24-hour rainfall events in the PNW will intensify by an average of 22% and occur seven days per year, on average, compared to two days

per year historically (1970 – 1999) by the 2080s (Nature Conservancy and the Climate Impacts Group, 2016). As a result, soil water content on December 1st, which is used as an indicator of winter landslide hazard, is expected to increase up to 35% in the 2040s relative to 1970 – 1999 along the western Cascade slopes (Mauger et al., 2015).

Modeling by Murphy (2016) in the Nooksack basin predicted a reduced snowpack in the Nooksack basin as a result of more precipitation falling as rain rather than snow. The increase in winter precipitation caused more runoff, and increased winter stream flows, doubling by 2075. Winter runoff is expected to be more rapid and higher in magnitude, which will result in an increased risk of flooding, soil erosion and mass-wasting events during the wetter winter months (Jiménez Cisneros et al., 2014; Mitchell et al., 2016). Recent studies in the Skagit River drainage suggest that the current 100-year flood will increase in magnitude by 26% and recur every 22 years by the 2040s (Lee et al., 2016). As a result of these larger floods that occur more frequently, a six-fold increase in sediment load during peak winter flow periods is projected by the 2080s (Lee et al., 2016). Murphy (2016) also predicted a significant decrease in both the areal extent and thickness of ice, with smaller glaciers disappearing completely. As glaciers recede there will be an increased exposure of unconsolidated, lateral moraine deposits that are readily erodible and have a propensity for shallow landslides as heavy rainfall events become more frequent and intense (Mauger et al., 2015; Lee et al., 2016).

2.5 Forest Harvesting and Hillslope Processes

Deforestation and the corresponding forest roads have been well documented to increase flooding, erosion, and landslide activity (Fredriksen, 1970; Peak Northwest, 1986; Turner and Schuster, 1996; Montgomery et al., 1998; Montgomery et al., 2000; Barik et al., 2017). Forestry practices have caused a documented increase in the frequency and absolute number of slope failures since 1940, with the approximately 90% of the observed landslides in Canyon Creek, a tributary of the North Fork, being associated with roads and clearcuts (Weatherly, 2005). An assessment of sediment delivery to streams in the Skookum and Cavanaugh Creek watersheds, located in the South Fork Nooksack River, found that 35% of the sediment delivered to streams was from road-related mass wasting and runoff from roads (Lummi Nation Natural Resources Department, 2012). The high density of forest roads in the nearby North Fork Stillaguamish River basin, some of which are placed on unstable geology and steep slopes, contribute to

increases in surface runoff and erosion pulses during periods of rain (Brown et al., 2011). The removal of vegetation leads to a decrease in root cohesion and associated shear strength over time, leading to increased sediment transport and susceptibility to landsliding (Montgomery et al., 2000; Lu and Godt, 2013). Furthermore, riparian logging destabilizes stream banks and slopes, which can lead to landslides that introduce fine sediment into surface water (Brown, 2011).

2.6 Previous Work on Mass Wasting in the Nooksack Watershed

Several studies have focused on mass wasting in the Nooksack watershed to better understand landslide hazards and sediment sources, as well as their effects on downstream sediment transport, aggradation, and flooding (Peak Northwest, 1986; Kirtland, 1995; Weatherly, 2005, Lummi Nation Natural Resources Department, 2015). To assist the Whatcom County Public Works Department in constructing a sediment management plan for the Nooksack River, a summary of sediment delivery to streams within the upper Nooksack River basin was completed by KCM, Inc., and compared to other published results (Weatherly, 2005). While these results quantified the average annual sediment delivery to streams by drainage area, there are multiple limitations to these findings. The available data for the Nooksack River streams are focused on only one or a few sub-drainages and results show that estimated sediment production varies wildly between streams, as there is a range of more than two orders of magnitude (Weatherly, 2005). For the creeks studied in the upper Nooksack basin, the greatest potential sources of sediment in the next five to 10 years were additional failures from inner gorges, clear-cut units, and roadfills (Peak Northwest, 1986). An assessment of sediment delivery for the Skookum and Cavanaugh Creek watersheds, located in the South Fork Nooksack River found that 65% of the sediment delivered to streams was a result of natural mass-wasting processes, 35% was from forest road effects (Lummi Nation Natural Resources Department, 2012). Overall, estimating sediment delivery to streams is difficult, with estimates usually having large uncertainties. Studies tend to focus on areas of high concern, or high sediment delivery, essentially neglecting other areas and skewing results that might be used to generalize results across the entire watershed (Weatherly, 2005).

Steeper headwater basins act as fine sediment sources within each sub-basin of the upper Nooksack Basin, as indicated from United States Geological Survey (USGS) sediment monitors

(Anderson et al., 2018). Average sediment yields of the entire Nooksack River (1,150 tons/mi^2/yr) are comparable with yields estimated in nearby basins such as the Sauk River (1,450 tons/mi^2/yr; Jaeger et al., 2017) and Stillaguamish River (1,740 tons/mi^2/yr; Anderson et al., 2017). Sediment yields in the upper basins of the Nooksack (2,000 – 2,500 tons/mi^2/yr; Anderson et al., 2018) were estimated to be similar to yields in the upper Nisqually River (3,100 tons/mi^2/yr; Czuba et al., 2012). Therefore, fine sediment in the Nooksack is produced at a rate comparable to, or slightly lower than, similar basins in the Salish Sea region. Fine sediment yields in the glaciated North and Middle Forks of the Nooksack basin were found to be very similar to yields from the unglaciated South Fork, which may be a function of the extent of continental glaciation and the subsequent production of extensive glacial till and glacio-lacustrine sediment commonly found in the South Fork Nooksack (Anderson et al., 2018). However, glaciated and unglaciated basins showed differences in grain size distributions. The North and Middle Forks produced fine sediment composed of about 60 – 70% sand, while the South Fork was composed of about 30 – 40% sand (Anderson et al., 2018).

2.7 Slope Stability

2.7.1 Overview

The stability of a slope is influenced by many controlling factors, such as the geometry of the slope, material strength within the soil matrix, root cohesion, and hillslope hydrology (Burton and Bathurst, 1998). Typically, these controlling factors work in combination, meaning that slope stability and therefore landslide occurrence should not be considered in terms of one individual factor. Slope failure can occur when external stresses on a soil mass exceed the strength of the soil, suggesting that slope stability can be evaluated by calculating the balance of forces acting on a soil or rock mass. One of the most common methods to quantify the force balance is a limit equilibrium analysis, which defines the state at which shear stress and shear strength are in equilibrium (Stead and Coggan, 2012).

2.7.2 Infinite-Slope Equation

The Hammond et al. (1992) infinite-slope stability model is used to calculate the factor of safety (FS) and screen for areas susceptible to broad-scale shallow landslides. Infinite slope mass-wasting events are generally less than three meters in depth and occur quickly in response

to triggering mechanisms, such as increases in pore pressures from rain events (Baum et al., 2007; Burton and Bathurst, 1998; Lu and Godt, 2013). An infinite-slope analysis is applicable when a soil mantle overlies an impermeable layer of bedrock or a denser soil layer (drainage barrier), the most common failure types found in the mountainous West (Hammond et al., 1992; Sidle et al., 1985). An infinite-slope analysis is a commonly used modeling application because it is computationally simple, input variables can be easily measured and are widely available in the literature, and it models the failure mechanism most common in forest watersheds (Wu and Sidle, 1995; Doten and Lettenmaier, 2004).

The basis of the infinite-slope equation is the Mohr-Coulomb failure criterion, with added variables considering the loading stress from overlying vegetation weight and changes in the effective stress and soil weight from static water table heights. A detailed derivation and force diagram can be found in Appendix A of Hammond et al. (1992). The infinite-slope equation for a cohesive, partially saturated soil is given by

$$FS = \frac{C_r + C_s + [q_0 + \gamma_m D + (\gamma_{sat} - \gamma_w - \gamma_m) D_w] cos^2 \alpha tan\varphi}{[q_0 + \gamma_m D + (\gamma_{sat} - \gamma_m) D_w] cos\alpha sin\alpha} \qquad (1)$$

where FS is the factor of safety representing the ratio of the shear strength to the driving stress. Here, C_r is root cohesion (kPa), C_s is soil cohesion (kPa), α is the slope angle (degrees), φ is the friction angle (degrees), q_0 is vegetation surcharge (kg/m^2), γ_m is unsaturated soil weight (kg/m^3), γ_{sat} is saturated soil unit weight (kg/m^3), γ_w is water unit weight (kg/m^3), D is the total soil thickness (m), and D_w is the saturated soil thickness (m). Root cohesion is the additional strength supplied by vegetation through the binding effects of roots in soil. Soil cohesion refers to the any additional strength in the soil, which typically includes electrostatic attraction between soil particles, intergranular cementation, and negative pore pressure due to matric suction within the unsaturated zone (Lu and Godt, 2013). The friction angle quantifies the coefficient of friction between individual grains and is defined as the maximum slope angle achieved before a soil mass fails independent of cohesion effects. Vegetation surcharge defines the overlying weight of vegetation acting on a soil mass.

The infinite-slope equation operates on several assumptions. The water table and failure plane are assumed to be parallel to the ground surface, which is generally true because of a high

hydraulic conductivity contrast between the soil and the drainage barrier (Hammond et al., 1992). For simplicity, only a single soil layer is considered. The failure plane is assumed to be infinite in extent, the length is much longer than the thickness; therefore values for root cohesion and soil shear strength reflecting conditions along the true failure plane should be used, not just along the drainage barrier (Hammond et al., 1992). The last assumption made is that the infinite-slope equation is a two-dimensional analysis, meaning that resistance along the sides of the failure is negligible in comparison to resistance along the base. When comparing two-dimensional analysis with three-dimensional analysis of block models, it was shown that the infinite-slope model gives the same results with blocks having widths greater than approximately 9 m, with the two-dimensional analysis producing conservative results with narrower failures (Hammond et al., 1992). Therefore, using 1-m inputs might predict lower factors of safety compared to 10 m resolution results.

Generally, the infinite-slope equation is most sensitive to changes in slope, soil cohesion, root cohesion, soil depth, and groundwater-soil depth ratio, moderately sensitive to changes in the friction angle, and the least sensitive to changes in tree surcharge, saturated unit weight (Hammond et al., 1992; Doten and Lettenmaier, 2004). The FS in Equation (1) increases with increasing soil cohesion, root cohesion, and friction angle, and decreases with increasing slope, soil depth, water table height, soil unit weight, and vegetation surcharge. When the value for soil depth is decreased, the FS becomes more sensitive to soil and root cohesion and less sensitive to friction angle and groundwater-soil depth ratio (Hammond et al., 1992). An extensive review on the sensitivity of infinite-slope equation parameters is in Chapter 3.3 of Hammond et al (1992).

Prompted by significant damages as a result of landslides in the late 1990s, the City of Seattle and the USGS applied infinite-slope analysis with an extensive landslide record to compare actual landslide locations with those predicted by modeling, ultimately producing a landslide hazard map of the city. Generally, many of the steep slopes associated with glacial deposits were found to be highly susceptible to slope failures, with the lowest FS values in areas where geologic units have low shear strengths (Harp et al., 2006). The similar geologic deposits and common landslide failure mechanisms in the Seattle area provide insight to infinite-slope failures in nearby forested watersheds, such as the Nooksack basin.

Following the shallow landslide susceptibility protocol of Burns et al. (2012), the Washington State Department of Natural Resources (WADNR) began a landslide mapping

project to help local communities within the state become more resilient to landslide hazards through the accurate identification of landslide deposits and the prediction of where landslides might occur in the future (Mickelson et al., 2017). The WADNR follows a streamlined landslide identification protocol (SLIP) mapping procedure to digitize shallow and deep-seated landslides (Burns et al., 2012; Mickelson et al., 2017). The WADNR also uses a simplified version of infinite-slope equation (Equation 1) for shallow landslide susceptibility analysis. They ignore root cohesion and use a uniform soil type and thickness with constant mechanical strength values (Mickelson et al., 2017). The WADNR will be applying the susceptibility tools to the Nooksack basin starting in the fall of 2018.

3.0 Methods

3.1 Digital Watershed Characteristics

I examined mass-wasting susceptibility in the upper Nooksack basin using two different modeling approaches that employ the infinite-slope algorithm outlined by Hammond et al. (1992)—a static ArcGIS raster-based method, and a dynamic probabilistic approach that is integrated in the DHSVM hydrology model (Doten and Lettenmaier, 2004). I applied two modeling approaches in part to compare the different outcomes of the models and to assess the relative model skill and the utility of using the simpler, more user-friendly static ArcGIS model as a means to determine mass-wasting susceptibility. Both models require grid-based digital inputs that characterize the spatial and mechanical attributes of soils and vegetation of the basin, which I summarize below.

3.1.1 Digital Elevation

Newly acquired, 3-ft resolution LiDAR (Light Distance and Ranging) covering most of the upper basin was obtained through the WADNR to represent elevations throughout the upper Nooksack basin (McWethy, 2016). The LiDAR was produced using an aircraft-mounted scanning laser rangefinder and processed to remove tree canopy to produce high resolution bare earth topography (Puget Sound LiDAR Consortium, 2006). The original 3-ft LiDAR was converted to sub-1 m resolution for consistent units. Due to the missing coverage of newly acquired LiDAR in the North Fork basin, a coarser 10 m resolution digital elevation model (DEM) was used to produce a dataset covering the entire study area (Figure 3). The 1 m LiDAR

was resampled to a 10 m DEM to create the optimal input resolution for mass-wasting analysis for the two models. Using the slope tool within ArcGIS and the DEMs I created slope angle raster grids. Both 10 m and 1 m resolutions were used as inputs for the static ArcGIS infinite-slope model to allow for comparisons between resolutions.

3.1.2 Surface Geology and Soil

To characterize the surficial geology of the upper Nooksack basin I used a combination of publically available digital geology and soil maps. GIS shapefiles of local surface geology and landslides are available for download from the WADNR (Washington Division of Geology and Earth Resources, 2016). I selected a 1:100,000-scale geologic map of the study area due to the data having the highest resolution of mapped surface deposits that covered the entirety of the upper basin. The original geology shapefile contained polygons and associated attributes of bedrock and surficial units. I used a shapefile outlining DNR mapped debris flows and shallow landslides to represent landslide deposits in the basin and added shallow landslides on Mount Baker mapped in a recent mass-wasting inventory by Nielsen and Grah (2015). Additionally, I followed the SLIP mapping procedure used by the WADNR to identify and digitize more landslide deposits within the upper Nooksack basin. Through the interpretation of LiDAR derivatives (e.g., hillshade, slope angle, etc.) in a GIS, the SLIP mapping procedure categorizes the confidence of the landslide deposit being mapped and streamlines the identification process by omitting detailed attributes that are usually associated with landslide inventories (Mickelson et al., 2017). High confidence landslides were marked by a polygon that encompasses the entire landslide (headscarp, side scarps, etc.) and are the only confidence category added to the complete landslide inventory (Figure 4).

Quaternary-aged unconsolidated to semi-consolidated units were queried from the original geology shapefile based on their available mechanical strength literature values and propensity for shallow mass-wasting failures. Deposits used from the original shapefile include alluvium (Qa), continental glacial drift (Qad), alluvial fan deposits (Qaf), continental glacial outwash (Qgoe), glacial till (Qgt), landslide deposits (Qls), and talus deposits (Qta). The original geology shapefile included the extent of glaciers, which were not up to date with current glacier extents, as they had receded in the basin since the mapping was produced. To rectify this, I used publicly available color orthophotos to digitize and update the extent of glaciers.

As glaciers recede, they expose unconsolidated and unvegetated sediments (e.g., moraines and outwash), which are susceptible to erosion and slope failure. Moraines were not identified in the initial geologic map shapefile, so I used color orthophotos and LiDAR to identify and digitize moraines (Qm) in the geologic shapefile. Because actual moraine thicknesses are unknown, I used a constant moraine thickness of 3 meters to be consistent with the WADNR's application of their infinite-slope model (Figure 5; Mickelson et al., 2017). Using projected glacier extents centered on 2080 in the North Fork and Middle Fork basins after Murphy (2016), I altered the extent of glaciers to simulate future landscape conditions. A decadal average of glacier extents centered on 2080 modeled using aggressive carbon emission scenarios was used to represent conditions in the late 21st century. Moraine deposits that were digitized to represent historical conditions were extended to signify additional moraine buildup as a result of historical glacier retreat. The attitude of nearby bedrock was a key factor on the decision to extend previously mapped historical moraine deposits, which limited how many deposits were extended. All moraine deposits were classified as Qm and assigned the same mechanical characteristics and constant soil thickness, regardless of their representation of historical or projected landscapes (Table 2 and 5). While mechanical soil characteristics representing moraines are difficult to estimate due to their heterogeneity, I used literature values to estimate the angle of friction and cohesion values (Table 2 and 5; Lebourg et al., 2004).

Soil data are available in shapefile format from the United States Department of Agriculture (USDA) Natural Resource Conservation Service (NRCS) Geospatial Data Gateway and USDA Forest Service databases (USDA Forest Service, 1991; Soil Survey Staff, 2016). The USDA NRCS provides soil coverage in the form of soil survey geographic (SSURGO) shapefiles. The SSURGO shapefiles are separated by state counties and the Nooksack watershed extends into both Whatcom and Skagit Counties, so separate soil SSURGO shapefiles were downloaded and clipped to the basin extent. The SSURGO shapefiles were selected because mapping unit symbols attached to polygons in the attribute table can be correlated to the Unified Soil Classification System (USCS) designation, which I use for engineering purposes.

The SSURGO shapefiles only cover the western extents of the upper Nooksack basin, terminating at the boundary of the Mt. Baker-Snoqualmie National Forest. To complete the soil coverage in the basin I combined the SSURGO shapefiles with soil resource inventory (SRI) shapefiles downloaded through the USDA Forest Service (Figure 6; USDA Forest Service,

1991). The SRI was originally mapped on aerial photos in 1976 at a 1:62,500 scale and digitally traced and scanned using a 1:1 scale in 1991 (USDA Forest Service, 1991).

Soil depth grids were established using a Python/ArcGIS script developed for the DHSVM (Figure 5; Ning Sun, personal communication). The script uses a scheme that assigns a soil thickness for each grid cell based on the DEM in a basin, i.e., high elevations are assigned thin soil depths and low relief regions are assigned thicker soil depths determined by a user defined minimum and maximum soil thickness. The soil depth grids were created for each sub-basin and represented at 10 m and 1 m resolutions. Two ranges of soil depths (0.76 – 3.5 m, 2.0 – 3.5 m) were created to analyze the effect of soil depth on slope stability. While the script-generated soil depth grid is difficult to verify at the basin scale and has a significant control on mass wasting, the range of soil depth is realistic and more applicable when compared to using a constant depth soil grid or a constant depth to failure, e.g., that used by the WADNR (Mickelson et al., 2017). Constant soil depths representing digitized moraine deposits in the upper reaches of the basin were used in place of the original, thin soil depths produced by the Python script.

Using the Web Soil Survey available through the USDA NRCS I paired the SSURGO soil types with Unified Soil Classification System (USCS) soil types and added a USCS class in the attribute table. The USCS is a soil classification system applied in engineering and geology to describe the grain size distribution of a soil using a letter designation. For example, the USCS classification for SW would designate a soil as a well-graded sand. The queried geologic units, SSURGO shapefiles, and SRI shapefile were merged together to produce a final surficial shapefile (Figure 7), which is converted to raster format at the appropriate resolution for use in the static ArcGIS and DHSVM models.

3.1.3 Landcover

I used Washington State 2011 land cover data from the National Oceanic and Atmospheric Association (NOAA) collected using 30 m resolution Landsat Thematic Mapper and Landsat Enhanced Thematic Mapper satellite imagery (NOAA, 2011). The NOAA data includes land cover class groups of developed land, agricultural land, grassland, forest land, scrub land, barren land, wetlands, water and ice, with nested land cover classes within each group (Figure 8). The original 30 m resolution raster was resampled to 10 m and 1 m resolution rasters to conform to necessary input resolutions for the static model. NOAA land cover

classifications are different from the land cover classifications used in DHSVM, therefore the original raster values associated with NOAA land cover classes were converted to the appropriate DHSVM land cover values (Table 3; Figure 9). General differences between the NOAA and DHSVM land cover classifications include different assigned values and broader DHSVM classifications that include multiple NOAA classifications. For example, DHSVM defines grassland to include NOAA classifications of pasture/hay, palustrine emergent wetland and grassland. In addition to this, DHSVM defines bare as NOAA classifications of developed open space, unconsolidated shore, and bare land. A detailed description of creating a land cover raster that is compatible with DHSVM can be found in the work of previous researchers (e.g., Dickerson, 2010; Murphy, 2016).

3.2 Forecasted Snow and Landscape Change

I estimated the forecasted loss in snowpack area and increase in snowpack elevation into 21st century using the results of Mitchell et al. (2016). They used the calibrated DHSVM of Murphy (2016) to generate, and average, winter snow water equivalent (SWE) raster outputs produced over thirty-year simulations surrounding the years 1995, 2050 and 2075. The historical period was modeled using a gridded meteorological forcing data set (1981-2010; Livneh et al., 2015). Forecasted modeling applied a single GCM (CSIRO-Mk3-6-0 with RCP 8.5) which closely approximates the median of the 10 GCMs applied by Murphy (2016). January 1 was used as the output day for computing SWE rasters because historically January is a high precipitation time of the year, and one of the coldest. With increasing temperatures towards the end of the 21st century, Mitchell et al. (2016) predicted that the winter snowline would be restricted to elevations above 1200 - 1500 m.

Using ArcGIS software and the snowmap results of Mitchell et al. (2016), I quantified the percent increase in area experiencing reduction in snowpack coverage. Within these projected snow-free areas, I used available GIS data and examined the increase in factors that are related to mass wasting. I quantified the increase in area of slopes greater than 25° based on Doten et al. (2006), harvestable forest areas (acquired from Ken Pierce, personal communication), the length of forest roads, and mapped landslides (WADNR, 2017).

3.3 ArcGIS Infinite-Slope Modeling

3.3.1 ArcGIS Model

Using ModelBuilder and the raster calculator in the ESRI ArcGIS 10.4 software suite, I developed an infinite-slope model based on the modified Hammond et al. (1992) infinite-slope equation (Equation 1) to calculate the FS at each cell within a watershed (Figure 10). The ModelBuilder is a tool in ArcGIS that facilitates repetitive processing of digital data sets. Raster inputs and output grid cells are at the resolution of the DEM. Raster inputs include the LiDAR-derived DEM, slope angle, internal angle of friction, soil cohesion, root cohesion, dry unit weight, saturated unit weight, water unit weight, and soil depth. A ratio of the water table height to the total depth of soil is selected to represent the saturation amount at each cell throughout the basin.

3.3.2 Static Mechanical Properties

To apply the model, I had to add mechanical attributes to my soil and vegetation grids. I used ArcGIS to manually add attribute table columns representing friction angle, soil cohesion, dry unit weight, and saturated unit weight for each polygon based on available literature values. Given the proximity and similar glacial geologic history, values applied to landslide-prone geologic deposits in the Seattle area were assigned to similar deposits in the Nooksack basin (Koloski et al., 1989; Savage et al., 2000; Harp et al., 2006). Shear strength values used for Seattle geologic deposits were selected based on an archived database of shear strength tests, and are near the average values reported.

I applied typical USCS literature values for soil cohesion, friction angle, and dry unit weight to the soils and geologic deposits in Figure 7 (Table 2). Saturated unit weight values were approximated from a typical relationship between dry and saturated soil weights observed in the literature (Koloski et al., 1989; Geotechdata.info, 2013). To establish the mechanical properties of the SRI soils, polygons were matched to either the closest USCS classification or geologic deposit. The soil survey type (SST) attribute column listed descriptions of soil using the USDA Textural Soil Classification. Parent material (PM) described the underlying geologic material or deposit, such as glacial till and glacier deposited fresh sands and gravels. Based on the information from both the SST and PM attribute columns, I manually input the most appropriate USCS classification or geologic deposit and associated literature mechanical attributes. I used a

method for switching from the USDA to USCS soils outlined by García-Gaines and Frankenstein (2015). A constant value raster of 9.81 $\frac{kN}{m^3}$ was used for the specific weight of water and a constant ratio of water table height relative to soil depth was selected and applied to the soil depth grid to produce water table depth at each cell.

Using the polygon to raster tool in ArcMap, the surficial shapefile was converted to individual rasters representing the internal angle of friction, soil cohesion, dry unit weight and saturated unit weight across the basin used as inputs to the modified infinite-slope algorithm (Equation 1; Figure 10). Separate watershed boundaries and digital datasets for the North, Middle and South forks of the Nooksack River applied by Murphy (2016) were created to better capture local variability in each sub-basin.

I assigned static root cohesion values to the DHSVM vegetation classes (Figure 9) based on prior mass-wasting modeling in mountainous regions (Hammond et al., 1992; Montgomery et al., 1998; Doten and Lettenmaier, 2004; Table 4). Although the DHSVM mass-wasting model considers vegetation surcharge, it was omitted from my static infinite slope mass-wasting algorithm because the FS is not very sensitive to vegetation surcharge (Hammond et al., 1992). I validated the outputs of the ArcGIS static model by manually calculating individual raster values at twenty 10 m pixels throughout the basin.

3.3.3 Modeling Scenarios

To better understand the sensitivity of input variables on mass-wasting susceptibility, I employed the static ArcGIS raster-based method on the entire upper Nooksack basin assuming no snow coverage. I used two variable soil depths and water table to soil depth ratios (D_w/D) of 0.7 and 0.95. To display the effects of forecasted climate change on mass-wasting susceptibility, I analyzed differences between historical and projected snowpack coverages. I also applied different resolutions for input rasters (1 m and 10 m) to evaluate the influence of spatial scale to FS and slope susceptibility outputs. I calculated and compared susceptible areas for different modeling scenarios to estimate the relative influence of each variable.

3.4 DHSVM Infinite-Slope Modeling

3.4.1 DHSVM Hydrology Model

The DHSVM is a physically based, spatially distributed hydrology model that was developed at the University of Washington and the Pacific Northwest National Lab for mountainous watersheds (Wigmosta et al. 1994). The model has been used extensively in the PNW to examine the impact of land use and climate change on streamflow (e.g., Stork et al., 1998; Leung and Wigmosta, 1999; Bowling et al., 2000; Elsner and Hamlet, 2010; Battin et al., 2007; Cuo et al., 2011; Dickerson-Lange and Mitchell, 2013; Murphy, 2016). The DHSVM requires digital grids of spatially variable watershed characteristics, including a DEM, soil type, soil thickness, vegetation, and stream networks. Hydrology was modeled in the Nooksack basin at a 50 m resolution. The DHSVM utilizes physical relationships and a sub-daily (3-hr) time series of meteorological input data including temperature, precipitation, wind speed, humidity, and short-wave and long-wave radiation to model the flux of water and energy at the pixel scale of the DEM; excess water is routed through a stream network. Historical meteorological inputs will include observational gridded daily data developed by Linveh et al., (2013) that were disaggregated into 3-hr time steps and bias corrected (Murphy, 2016.

Future hydrology with the DHSVM employed meteorological data from GCMs downscaled to the Nooksack basin. The downscaled future climate data developed by Abatzoglou and Brown (2012) using the multivariate adaptive constructed analogs method (MACA) were trained with the same grid point data of Linveh et al., (2013). To calibrate for an observed cold bias derived from a constant temperature lapse rate in the historical Livneh data, a delta method correction (e.g., Sperna Weiland et al., 2010; Watanabe et al., 2012) was applied to all Livneh cells within each sub-basin to adjust to PRISM temperature normal (Murphy, 2016). The downscaled data compared well with observational temperature data from SNOTEL stations within each sub-basin, indicating a more realistic representation of monthly temperatures (Murphy, 2016).

3.4.2 DHSVM Sediment Module

The DHSVM sediment module was developed as a component to the DHSVM hydrology model (Doten et al., 2006). Hydrology outputs are redistributed over a higher-resolution DEM grid (i.e., 10 m) to estimate mass wasting, sediment delivery and channel transport in

mountainous, forested watersheds. Mechanical soil and vegetation properties are assigned to grid cells and, in combination with outputs from the hydrology model, sediment flux is simulated by four processes: mass wasting, hillslope erosion, road erosion, and channel routing. Mass wasting is the only process of the sediment module applied in my analysis.

The DHSVM sediment module is computationally intensive, therefore it is set up to run during the time step that coincides with the greatest basin saturation (a DHSVM output) during a storm even. The basin saturation is the percentage of the number of pixels in the basin with a water table to soil depth ratios (Dw/D) greater than 0.85. A screening process throughout the basin is applied to limit computations to critical areas. The algorithm ensures that a grid cell is a potential sediment source and meets a user-defined minimum surface slope angle for mass wasting. The DHSVM uses 10º as a conservative value, even though Doten et al. (2006) noted that slope stability theory indicates shallow landslides are infrequent on slopes less than 25° (e.g., Sidle et al., 1985; Reneau and Dietrich, 1987; Burton and Barhurst, 1998).

All cells that meet our criteria are subject to a FS analysis based on the infinite-slope model, using a Monte Carlo style simulation to incorporate the variability and uncertainty of many input parameters (Hammond et al., 1992). The mass-wasting algorithm generates stochastic results of slope failure using predetermined probability distributions for four parameters that define shear strength and loading on a hillslope: soil cohesion, friction angle, root cohesion and vegetation surcharge (Doten et al., 2006). Random soil and vegetation values are chosen from these probability distributions and applied in the infinite-slope failure algorithm (Equation 1) in an iterative process. I used 1000 iterations per cell, which is typically used as a sufficient amount to incorporate spatial variability of input parameters and produce reproducible results (Hammond et al., 1992). The final output is a cell-by-cell probability of failure for a particular storm event, calculated by the following equation:

$$P = \frac{m}{n} \tag{2}$$

where P is the probability of failure ranging from 0 to 1, m is the number of iterations for which failure was calculated, and n is the total number of iterations. Probabilistic models prove to be advantageous over static models because they incorporate uncertainty and variability associated

with the prediction of slope stability, quantifying heterogeneities that are inherent in natural systems (Hammond et al., 1992).

3.4.3 Probabilistic Mechanical Properties

The DHSVM sediment module assigns a probability distribution and range of values to each soil and vegetation class for soil cohesion, friction angle, root cohesion and vegetation surcharge. Normal, triangular and uniform probability distributions are used by the DHSVM to define mechanical properties assigned to soil and vegetation classes (Doten et al., 2006). A normal probability distribution is defined by a mean and a standard deviation. Normal distributions are typically used to describe a process in which values are distributed about one "true" value that is observed from laboratory work on a single soil or vegetation type (Hammond et al., 1992).

Triangular and uniform distributions are typically used for parameters that are poorly understood. Triangular distributions are defined by a minimum, maximum and a mode. The mode is the most likely value, while the probability is near zero at the minimum and maximum values. Triangular distributions are useful when limited field information is available, yet there is enough information to define probable values for the mode and range (Hammond et al., 1992). Uniform distributions are defined by a minimum and maximum value, making every value within the defined range equally likely. A uniform distribution is appropriate in describing heterogeneous materials that typically have minimum and maximum values that can be approximated from limited field information (Hammond et al., 1992).

I use a combination of parameters derived from PNW studies investigating slope stability, DHSVM literature, and mechanical soil characteristic literature to determine parameters for each soil and vegetation class (Doten and Lettenmaier, 2004; Hammond et al., 1992; Geotechdata.info, 2013). Soil classes included geologic units and USCS soil type designations, while DHSVM vegetation classes were matched to the closest vegetation parameters used in Doten et al., 2006 (Table 4 and 5). Mechanical characteristics used by Barik et al. (2017) in the Olympic Mountains compared relatively well with the mechanical characteristics that I applied in the Nooksack basin.

3.4.4 Modeling Scenarios

The probability of failure was analyzed for two historical and five forecasted storm events. Storm events were chosen throughout the 21st century during the months of October, December, January, and February. The timing of storm events was selected to provide a comparison of mass wasting with differing snow coverages and at various stages throughout the century. October was included because, historically, large storms can occur before the onset of significant snowpack resulting in high-peaked flood events. Winter storms were chosen to examine how the basin would respond as it receives more rain than snow into the 21st century during the months with the highest precipitation. Storm events that resulted in highly saturated basin conditions were selected to represent hydrologic conditions that would increase the probability of shallow mass-wasting events. To isolate these conditions, precipitation outputs from the CSIRO-Mk3-6-0 GCM and RCP8.5 meteorological time series were screened to identify high intensity precipitation events with values greater than 0.015 meters of precipitation during a single three-hour time step. A total of seven storm events were selected based on the greatest basin saturation extent during the previously selected high intensity precipitation events. The DHSVM outputs a basin average precipitation magnitude at every time step. These values were used to sum antecedent precipitation magnitudes of varying durations for each storm event.

3.5 Infinite-Slope Data Analysis

Outputs of the static ArcGIS model are rasters of FS values at every grid cell in the basin. Using ArcGIS I isolated cells having FS values less than 1.5 to create maps that could be used as a susceptibility tool. I used these maps to quantify actual areas having values > 1.5 by summing pixels at the respective resolution. Each DHSVM storm event simulation produced an output raster of the probability of failure, ranging from 0 to 1, on a cell-by-cell basis over the three-hour time step (storm event). I used ArcGIS to query probability values greater than 0.25 to create maps that isolate locations of higher failure probability, and to limit the amount of data that I used for my infinite-slope analysis. To analyze the change in modeled failure probabilities through the 21st century, I calculated differences in failure probabilities (0.25 – 1.0, 0.75 – 1.0) between historical and projected storms. To isolate the effect of snowpack conditions on failure probability outputs, I analyzed the fall and winter storms separately.

In addition to the above maps, I employed another technique applied by Saha et al.

(2005) using the van Westen (1997) Information Value (InfoVal) method to create mass-wasting susceptibly maps based on the DHSVM outputs. The area of static FS outputs and DHSVM probability of failure outputs within a certain area of segmented sections of a class layer (e.g., slope angle or geologic unit) was calculated to produce a weighted value that assesses which factors have the greatest effect on failure probabilities. For example, the range of slopes within a basin can be segmented into various classes that are each weighted against failure probabilities. Weights of a specific class are determined by the following equation:

$$W_i = ln \frac{Class\ density}{Map\ density} \quad (3)$$

where W_i is the weight given to the *i*th class of a specific class layer (e.g., 15 - 30° in the class of slope). Class density is the landslide density within the specific class, or the number of landslide pixels in a segmented class divided by the total number of pixels in the same class. Map density is the landslide density within the entire class layer; in my case it is either the FS output (< 1.5) from the static model or the probability of failure output (0.25 to 1.0) from the DHSVM. The natural logarithm is applied to account for the large variation in weights. Generally, positive weights are associated with higher susceptibility to failures and negative weights are associated with lower susceptibility to failure (Saha et al., 2005).

After weights were calculated, they were assigned to the segmented sections of each class to produce weighted class maps. All weighted class maps were then overlain and added together to produce a Landslide Susceptibility Index (LSI). The LSI values have an associated range that need to be segmented in order to generate a Landslide Susceptibility Zonation (LSZ) map. Following the methodology of Saha et al. (2005), the cumulative frequency curve of LSI values were segmented into five classes that represent a near-equal distribution. The five classes represent landslide susceptibility zones: very low, low, moderate, high and very high.

The resulting LSZ map displays a combination of factors responsible for landslide susceptibility. For my study, I selected class layers that are generally well-known to have a large effect on slope susceptibility and factors that are more sensitive within the Hammond et al. (1992) infinite-slope equation. Soil depth, saturation percentage, slope angle, landcover and surficial coverage (soils and geologic deposits) were the layers selected to be segmented into classes and weighted to produce LSZ maps. To assess the change in landslide susceptibility

throughout the 21st century and isolate highly susceptible areas associated with particular storms, LSZ maps were produced based off of the intersection of class layers and failure probabilities (0.25 – 1.0) of each DHSVM storm event and compared. The creation of LSZ using DHSVM failure probabilities provide an additional tool for slope susceptibility assessment, as the resulting failure probabilities and LSZ maps take into account similar attributes associated with slope failures of the DHSVM. I also compared the static and probabilistic results to assess locations and patterns of susceptible areas.

An additional output from each DHSVM is a raster of the accumulated SWE at the time step of the modeled storm. I used raster outputs of SWE during each storm event as a proxy for snow coverage, and used them to assess changes in areal snow coverage throughout the basin and 21st century. I filtered the SWE rasters by eliminating SWE values less than 0.1 m to eliminate thin snow coverages.

4.0 Results

4.1 Forecasted Snow and Landscape Change

On average, there is a 60% reduction in area covered by snow in January later in the 21st century based on the snow coverages produced by Mitchell et al. (2016), increasing the area available for runoff and mass-wasting susceptibility through the winter (Table 6; Figure 11). The newly exposed snow-free area has an increase in slopes that have angles greater than 25°, predominately in the North and South Fork basins. Relative to the historical landscape, the length of forest roads exposed in the future is projected to increase ~ 67% across the three sub-basins (Table 6; Figure 12; WADNR, 2017). Areas designated as commercial or rural forestry that have the potential to be harvested will increase by 80% from the historical to projected landscape as a result of decreasing snowpack, mainly in the Middle and South Fork basins (Table 6; Ken Pierce, personal communication; Berry, 2017). The increase in average winter snowline elevation will expose mapped landslide deposits to mid-winter rain, primarily in higher elevations (>1000 m; Figure 13). An area of 21.4 km^2 classified as previously mapped landslides becomes exposed by the 30-year normal surrounding 2075. The average slope measurement of mapped landslide deposits within the exposed area is 23.4°, suggesting that most of the previously mapped landslides within the Upper Nooksack basin are located on slopes that are known to be prone to failures.

4.2 Infinite-Slope Analysis

4.2.1 Static (ArcGIS) Infinite-Slope Results

Assuming a snow free landscape, the static infinite-slope modeling results indicate a larger percentage of areas susceptible to shallow slope failure (FS < 1.5) when using inputs with finer topographic resolution, more saturated soil conditions, and thicker soils input variables. All scenarios in each sub-basin showed a significant increase in susceptible areas with the thicker soil depth raster (2.0 – 3.5 m) as compared to the thinner soil depth raster (0.76 – 3.5 m), mainly because thicker, saturated soils on steeper slopes produce lower FS values. The greatest change in susceptible area was observed in the Middle Fork basin when applying thicker soils compared to thinner soils, whereas the South Fork basin showed the least amount of change of the three upper basins (Table 7).

The application of 1 m resolution compared to 10 m resolution produced an increase in areas susceptible to shallow slope failure for all modeling scenarios and within each sub-basin (Table 7; Figure 14). When applying finer resolution, the largest increase in susceptible areas from the coarser resolution scenarios were observed in the South and Middle Fork basins (Table 7; Figure 14). Increasing the saturation level of the soils resulted in an increase of susceptible areas within each upper basin, regardless of the resolution and soil thickness scenario applied (Table 7). Susceptible areas were found to be less sensitive to changes in fine resolution input parameters compared to coarse resolution input parameters. For example, the susceptible area increased by an average of 27.9% when increasing saturation levels using 10 m resolution inputs when compared to 1 m resolution inputs, which increased by an average of 18.7% (Table 7).

I also assessed the FS < 1.5 areas after placing the historical and forecasted snow coverages on the FS map generated using the thinner soil depth raster (0.76 – 3.5 m) and a very high ratio of water table to soil depth (0.95). As a result of the increase in snow-free area, the projected landscape had 130% more susceptible area than the historical landscape (Figure 15). Most of the susceptible area increases are observed in the higher elevation regions of the Middle and South Fork basins. Increases in susceptible areas within the projected landscape are also a result of the exposure of the new moraine areas I digitized. The total area of digitized moraines within the North Fork and Middle Fork basins based on Murphy's (2016) 2080 projected glacier extents increased by at least 1.74 km^2, with the most increases occurring within the North Fork

basin (Table 8; Figure 16). Compared to other deposits, moraine deposits produce exceptionally low factor of safety results (Figure 16). The increase in moraine deposits, which have a propensity for mass-wasting failures, will likely lead to an increase in sediment entrainment and overall slope failure when exposed to fall storm events.

To provide a comparison between modeling methods, InfoVal weight (described in the Methods) were calculated using 10 m resolution grids and on areas where FS < 1.5. Positive weights are associated with higher susceptibility to shallow failures and negative weights are associated with lower susceptibility (Saha et al., 2005). Weights for slopes indicate that regions with moderate, steep, and very steep slopes (30 - 45°, 45 - 60°, 30 - 45°, 60°+) have the highest failure susceptibility, with the lowest susceptibility being associated with very shallow slopes (0 - 15°; Table 9). High failure susceptibility was observed with thin soil depths (0.76 – 1.0 m) for all upper basins, while thick soil (2.0 – 3.5 m) depth weights calculated in the North and South Fork basins indicate very low failure susceptibility (Table 9). Moderate soil depths (1.0 – 2.0 m) produced weights close to zero in value, indicating these soils are potentially susceptible to shallow failures (Table 9). The highest positive weights calculated were for thin soil depths and the lowest negative weights calculated were for thick soil depths in the North and South Forks. Highly susceptible soils associated with static results were observed to be sand (SW), loamy sand (GP, GM), sandy loam (ML-MG), silt (ML), muck (PT), talus (Qta), and moraine (Qm) deposits, while lower landslide susceptibility was indicated in sand (Qgoe), loamy sand (SM-SG, Qls), sandy loam (Qaf, SM), silt (Qgt), sandy clay (Qad), and organic (OH) deposits (Table 9). Weights for NOAA landcover classes indicate that regions covered by large conifers and shrubland have the highest failure susceptibility, while all other regions have low susceptibility, with the lowest susceptibility associated with broadleaf, bedrock, water, and ice regions (Table 9).

4.2.2 DHSVM Infinite-Slope Results

The basin average cumulative precipitation amounts were calculated for each sub-basin for 72-hour, 48-hour, 24-hour and 12-hour time periods prior to peak saturation extents for each of the seven storms (Table 10-11). The greatest amount of 72-hour cumulative precipitation was attributed to the January 2009 storm, with an average of 0.29 meters across all basins (11.4 inches); the least amount of 72-hour cumulative precipitation was received from a modeled

February 2041 storm, with an average of 0.12 meters (4.72 inches; Table 11). The highest amount of precipitation received 12 hours prior to the onset of a storm was an average of 0.098 meters across all basins (3.86 inches) during the December 2096 storm, while the least amount of 12-hour precipitation received was an average of 0.036 meters (1.42 inches) during the January 2009 storm (Table 11). A pattern was not observed in the spatial distribution of total cumulative precipitation between storm events, although several winter storms (January 2009, January 2018, January 2089) produced the highest precipitation amounts in the South Fork basin (Table 11).

I also processed the cumulative SWE raster outputs of DHSVM produced at the time of each storm. Significant differences in fall and winter snow coverages were observed, as well as snow coverages throughout the 21st century. Snow coverage during fall storms was minimal, with a total area of 38.5 km^2 during the October 2003 storm declining to 3.5 km^2 during the October 2089 storm (Table 12). Snow coverage decreased from 1,411 km^2 during the January 2009 storm to 60.1 km^2 during the December 2096 storm, indicating a strong decreasing winter snowpack despite winter seasons maintaining more snow coverage compared to fall seasons (Table 12). Note that the unusually large snow area that developed during the 2009 storm is a result of a large area of lowland snow that was relatively shallow and short lived. Snow coverages in the snow-dominated North and Middle Fork basins are greater than snow coverage in the lower elevation, rain-dominated South Fork basin for all storm events.

The varying precipitation storm characteristics and snow coverages resulted in different saturation extents (Table 10-13). Saturation extent is an output of the DHSVM and is defined as the percentage of cells within a basin where the water table depth is equal to or greater than 85% of the soil depth. The historical January 2009 storm produced the lowest three-basin average saturation extent of 43.6%, while the projected December 2096 storm produced the highest average saturation extent of 78.5% (Table 13). Fall storms produced exceptionally high saturation extents, suggesting that a reduced snow coverage contributes to highly saturated conditions. Projected storms in the latter half of the century produced some of the highest saturation extents when compared to historical and early century storms (Table 13). Winter storms produced varying average saturation extents of 43.6% (January 2009), 58.7% (February 2041), and 76.1% (January 2018), suggesting that antecedent precipitation has a direct effect on saturation extent and snowpack conditions throughout the century directly affect the saturation

extent observed during each storm (Table 11-13). For most storm events, saturation extent was greatest in the South Fork basin and lowest in the Middle Fork basin (Table 13).

The total area of failure probabilities between 0.25 – 1.0 calculated for each storm event indicates that the most failure probabilities occur within the South Fork basin, while the least amount of failure probabilities occurs within the North Fork basin (Table 14). In general, projected winter storm events produced significantly more failure probabilities than the historical winter storm (Table 14). The historical and projected fall storm events resulted in a similar area of failure probabilities between 0.25 – 1.0, which were exceptionally high when compared to late-century winter storm events (Table 14). The change in the total area of failure probabilities (0.25 – 1.0) calculated between storm events indicate the greatest increase from historical to late-century projected storms during the winter months. The majority of failure probability changes observed from historical to projected winter storms occur in the higher elevation areas of each upper basin, where the projected winter snowline has increased, and the areal snow coverage has decreased (Figure 17-19).

The change between the January 2009 storm event and projected January 2089 and December 2096 storm events resulted in an average increase between sub-basins of 243% and 283%, respectfully (Figure 17-19). Furthermore, the same comparisons between storms of high failure probabilities (0.75 – 1.0) showed an average increase of 344% and 313% (Table 15). Changes in failure probability areas between the January 2009 and February 2041 storms showed a very small average increase in comparison to other winter storms (Table 15). The projected October storm showed very minimal failure probability increases compared to the historical storm, likely due to similar saturation extents and areal snow coverages (Table 12-13 and 15; Figure 20-21). The greatest increase in the area of failure probability (0.25 – 1.0; 0.75 – 1.0) for all comparisons was observed in the Middle Fork basin, while the smallest increase in failure probability was observed in the South Fork basin (Table 15).

I estimated InfoVal weights in areas with failure probabilities between 0.25 and 1.0 for each storm event. Weighted calculations indicate the highest failure susceptibility associated with moderate to steep slopes (30 - 45°, 45 - 60°) and the lowest failure susceptibility associated with very shallow slopes (0 - 15°) for each storm event (Table 16-18). Probabilistic weights are consistently negative for slopes less than 30° and greater than 60°, with an exception being the positive weight for slopes 15 - 30° calculated from the January 2009 storm in the North Fork

basin. This can likely be attributed to more failures being restricted to lower elevations due to the larger snow coverage (Table 12 and 16). InfoVal weights associated with soil depths indicate that thin to moderate soil depths have a higher susceptibility to failures compared to thick soil depths, in part because they thin soils occur on steeper slopes. Thick soils in the Middle Fork basin consistently produced the highest slope susceptibilities in comparison to other basins, while thick soils in the North and Middle Forks tend to yield lower susceptibilities compared to thin and moderate soil depths (Table 16-18). InfoVal weights also indicate an increase in slope susceptibility with increasing saturation. All storms either produced extremely low weights or no failure probability pixels within cells containing saturation percentages between 0.1 and 0.7, while producing positive weights for soils that are very saturated to fully saturated (0.7 – 1.0; Table 16-18). Weights associated with landcover indicate that broadleaf, large mixed stand, and shrubland classes have consistently high failure susceptibility for all storms and within each upper basin, while landcover classes for large conifers, ice, sparse/open/agriculture, rock and water are consistently indicative of low failure susceptibility for all modeling scenarios (Table 16-18).

Individual InfoVal weights calculated for soil depth, soil saturation, slope angle, landcover and surficial coverage were added to create LSZ maps that represent failure susceptibility, similar to Barik et al. (2017). To comprehend changes in fall and winter failure susceptibility throughout the upcoming century, I compared differences between historical and late-century projected LSZ maps. Saha et al. (2005) defined five LSZ map classes: very low, low, moderate, high and very high. I chose to compare only the 'very high' susceptible areas throughout the century and between sub-basins (Figure 22-25). In the North Fork, the January 2089 and December 2096 storms saw a decrease in very susceptible areas of 24.1% and 10.5%, respectively when compared to the 2009 storm (Table 19). In the Middle Fork, very susceptible areas increased by 71.6% in the January 2089 storm, while very susceptible areas decreased by 24.4% in the December 2096 storm (Table 19). An increase of very susceptible areas was observed for both projected storms in the South Fork basin, with an average increase of 13.4% compared to the historical winter storm (Table 19). Comparisons between the historical October 2003 and projected October 2089 storms also showed differences in very high susceptible areas for each upper basin. Very high susceptible areas increased by 22.9% between fall storms in the North Fork basin, while these areas decreased by 52.5% and 1.17% in the Middle Fork and

South Fork basins, respectfully (Table 19). Visual comparisons of very high susceptible areas indicate that common surficial units are glacial outwash (Qgoe), loamy sand (GM, Qa), landslide (Qls), silt (ML), and moraine (Qm) deposits, with many deposits located along the outer edges of river valleys, presumed to be river bluffs (Figure 22-25).

5.0 Discussion

5.1 Forecasted Snowlines and Sediment Source Increases

The 60% reduction in snow coverage across all basins projected for 2075 will expose landscape that will be vulnerable to higher intensity storm events and subsequent sediment production (Table 6). A large increase in harvestable forest lands will be exposed during the winter months, especially in the Middle and South Forks (Table 6). If these lands are harvested in the future, they will present a higher sediment source risk. The effects of forest harvesting on mass wasting was not a focus of my study, yet removal of vegetation is known to have a significant effect on mass wasting and movement of sediment (Montgomery et al., 1998; Montgomery et al., 2000; Roering et al., 2003; Joshua et al., 2003). Sidle and Bogaard (2016) found an increase in landslide rate of about 2-10 fold compared to undisturbed forests approximately three to 15-20 years after forest harvesting as a result of a reduction in root cohesion and increased infiltration. The length of forest roads exposed to winter rainfall will increase by an average of 67% as the snowline increases in elevation into the 21st century. Forest roads increase surface runoff through the interception and redirection of surface runoff and subsurface flow, while also acting as an additional source of surface sediment (Table 6; Doten and Lettenmaier, 2004; Brown, 2011). In addition to sediment production from the initiation of mass-wasting movements on road cutslopes, culvert failures resulting from trapped sediment and debris can lead to increases in sediment delivery to streams (Flannagan, 1999; Wemple et al., 2001).

Previously mapped landslide deposits that will be exposed as a result of the increasing average winter snowline elevation may reactivate and be a source for sediment delivery (Figure 13). Landslide deposits are known to currently be serving as sediment sources in smaller watersheds within the upper Nooksack basin (e.g., Lummi Nation Natural Resources Department, 2012). The South Fork has abundant landslide deposits derived from structurally weak glacial deposits, which act as sediment sources due to their frequent failures (Nooksack

Natural Resources Department, 2016). Previous landslide deposits are the most probable sites for new landslides, as older deposits in a remolded state have a lower strength than the original soil (Selby, 1982; Hammond et al., 1992).

As expected, my mapped moraine deposits based on Murphy's 2080 ice extents produce low FS values by the ArcGIS model, and are susceptible to mass wasting (Figure 15-16). Although moraine deposits are more at risk to erosion and mass wasting when snow coverage is minimal or non-existent (i.e., during fall and spring storm events), some moraines will be exposed to high intensity precipitation events in the winter months as the snowline increases in elevations. Due to their instability and unconsolidated makeup, moraines deposits exposed to high intensity precipitation events will be the most susceptible to failure. In addition to slope failure, sediment from recently deglaciated moraines is also readily mobilized, transported, and deposited by other mass-wasting processes (O'Connor et al. 2001).

As the snowline increases there is a 38% increase in exposed areas with slopes greater than 25° in the upper Nooksack basin (Table 6). According to my static modeling FS < 1.5 maps and LSZ maps generated from my DHSVM modeling, these areas are more susceptible to failure compared to more gently sloping landscapes (Figure 15 and Figure 23). InfoVal weights resulting from my static modeling and probabilistic results (failure probability 0.25 – 1.0) also indicate that steeper slopes (30 - 60°) have the highest failure susceptibility. Correlating this increase in mass-wasting potential to actual sediment production is not within the scope of my project, but it will no doubt be one of the largest sediment sources to streams within the Upper Nooksack basin.

5.2 Static Modeling Sensitivity and Uncertainty

The exceptionally large study area of the upper Nooksack basin requires more generalization of model input variables, specifically; there are limitations and uncertainties associated with the scale of the surficial geology and soil mapping and other publically available digital data that I used in the model. As a result of these uncertainties, FS values do not necessarily follow the general stability thresholds, e.g., a slope with a calculated FS of 0.9 could not fail, while a slope with a calculated FS of 1.1 could fail (Hammond et al., 1992). A finer resolution of input grids would reduce uncertainly, but at this point, the only grid available at a finer resolution is the 1 m LiDAR. My static infinite-slope modeling results within all three

upper basins show that finer resolution inputs based on the LiDAR, produced an increase in total area having a FS < 1.5. Given that the slope angle is a key indicator for predicating infinite-slope failures, having a LiDAR coverage for determining slope angles in watersheds is essential.

Mechanical strengths values assigned to each deposit will affect associated FS results and InfoVal weights. I used literature values based on similar deposits and modeling studies. For example, I used a soil cohesion value of 19.2 kPa for landslide deposits based on Harp et al. (2006). While the assigned cohesion value is acceptable, the cohesion of landslide deposits is variable and more conservative literature values are available. Landslide cohesion values can vary based on the age of the landslide deposit and subsequent breakdown of material. Using cohesion-less values (e.g., Mickelson et al., 2017) allows for a more realistic, yet conservative representation of susceptibility with respect to landslide deposits, which are prone to additional failures through reactivation. The uncertainties associated with unconsolidated deposits can be decreased with additional validation using field measurements. While certain field values, such as soil depth, would be more difficult to verify in an expansive area, mechanical characteristics of soils specific to the field area would result in a more accurate representation of slope stability. Specifically, in-situ tests of site-specific mechanical properties (soil cohesion, angle of friction, root cohesion) associated with unique geologic or soil deposits would reduce model uncertainty through the refinement of probability distributions. The logical place to start would be the deposits that I found to be correlated to higher failure susceptibility, such as glacial outwash (Qgoe), loamy sand (GM, Qa), landslide (Qls), silt (ML), and moraine (Qm) deposits.

More susceptible areas were predicted when thicker minimum soil depths (2.0 m) were applied at higher elevations compared to thinner minimum soil depths (0.76 m; Table 7) because of how I estimated the water table depth in the static model. For example, if the D_w/D ratio is 0.95, the water table is 95% of the soil thickness, regardless how thick the soil. A nearly saturated thick soil at a steep angle would yield a lower FS than a nearly saturated thin soil. Moreover, for a constant soil thickness, a higher D_w/D ratio results in a lower FS value. Hammond et al. (1992) documented this in their sensitivity analysis. They also found that the FS becomes less sensitive to the D_w/D ratio when the soil depth is decreased. The addition of water into the soil increases the weight acting on the matrix and decreases grain-to-grain contact through buoyancy forces, effectively decreasing the overall shear strength and increasing the propensity for slope failures (Dhakal and Sidle, 2004; Sidle and Bogaard; 2016). As such, when I

apply a D_w/D of 0.95, there is a greater potential for infinite-slope failures (Table 7). My motivation for examining the infinite-slope susceptibility using a minimum soil depth of 2 m, even at high elevations in the basins, was based on the fact that the WADNR is currently using a simplified version of Equation (1) and assumes a 10 ft (~3 m) failure depth to assess susceptible mass-wasting regions (Mickelson et al., 2017). Aside from moraine deposits, I consider 2 m soil thicknesses to be unrealistically thin at high elevations in mountainous regions, meaning the WADNR model will predict more regions with low FS values at higher elevations.

The InfoVal analysis that I used to weight variables has limitations as a result of the relative magnitudes of the map and class densities in Equation (3). Given that the InfoVal method takes into account the overall area, deposits with limited coverage could produce abnormally low weights. For example, surficial units such as glacial outwash and landslide deposits that are likely susceptible to failure, produced lower weights and failure susceptibility than expected, primarily because both deposits make up relatively small areas within the upper Nooksack basin (Table 9; Figure 7). Also, despite conifer landcover having relatively high root cohesion values, InfoVal weight calculations indicate high failure susceptibility associated with conifers within each upper basin (Table 4 and 9). This is most likely attributed to the high percentage of overall conifer coverage with respect to other landcover classes, which would alter the associated weights by allowing for more potential intersection with susceptible areas. Slope categories in my analysis were defined by 15° intervals and my results revealed negative InfoVal values for the 15-30 ° category. Although Doten et al. (2006) noted that shallow landslides are infrequent on slopes less than 25°, it is possible that the failure risk could be higher for slopes between 15-30 °.

5.3 Forecasted Storm Effects on Mass Wasting

Increases in failure probabilities during winter months are attributed to the substantial decreases in areal snow coverage coinciding with increases in basin-wide saturation extent driven by cumulative precipitation increases. These conditions will lead to a subsequent increase in sediment delivered to streams. Despite 72-hour cumulative precipitation being greater for the January 2009 storm in comparison to the January 2089 and December 2096 storms, the resulting saturation extents for the projected storms are much greater than the saturation extent for the historical storm due to differences in snow coverage (Table 11-13). A relatively small increase in

failure probability occurred between the historical and forecasted October storms, which can most likely be attributed to the small difference in saturation extents due to the lack of snow coverage in October (Table 13 and 15).

The variability in storm characteristics, particularly differences between 72-hour and 12-hour cumulative precipitation amounts, can affect the sensitivity of mass-wasting susceptibility because most shallow failures occur from high groundwater pressures resulting from previous rainfall accumulation (Lu and Godt, 2013). Scientists are aware of the relationship between rainfall thresholds and shallow slope failures and have developed tools for risk assessment purposes in the Seattle region (e.g., Chleborad et al., 2006; Godt et al., 2006: Baum and Godt, 2010; Scheevel et al., 2017). Based on these works, the WADNR has developed a web-based tool for predicting mass-wasting risk using real-time rainfall (WADNR, 2018). The influence of rainfall on mass wasting is evidenced by my DHSVM modeling. For example, the average difference between the 72-hour and 12-hour cumulative precipitation amounts for the February 2041 storm was 0.052 m, which resulted in a low saturation extent (Table 11 and 13). The area of failure probabilities between 0.25 and 1.0 under these conditions was 2.31 km^2 (Table 14). The January 2018 storm produced an average difference of 0.13 m between 72-hour and 12-hour cumulative precipitation amounts, and a high saturation extent, resulting in 6.2 km^2 of failure probabilities between 0.25 and 1.0 (Tables 11-12 and 14). More areas with failure probabilities between 0.25 and 1.0 were predicted with future winter storms than the fall storms, with the February 2041 storm event being an exception likely related to relatively low cumulative precipitation amounts and resulting saturation extents (Table 11 and Table 13-14). While forecasted October storms are less likely to produce more failures than mid-winter storms due to anticipated lower saturation extents, higher amounts of precipitation earlier in the water year would act to precondition soil saturation levels and produce more failures, for example during rainfall events in November.

Approximately half of the total storm events show that the highest 72-hour cumulative precipitation amounts were received in the South Fork basin (Table 10-11). Subsequent saturation extents in the South Fork basin are typically the highest among the three upper basins as well as a result of the relatively lower elevations that receive more rain than snow (Table 1 and Table 10-11 and Table 13). The relatively high cumulative precipitation amounts and saturation extents, as well as minimal snow coverage becoming almost nonexistent by the end of

the century, likely makes the South Fork basin more sensitive to increases in mass-wasting susceptibility (Table 12). This increase in landslide susceptibility suggests a higher frequency of episodic and chronic sediment inputs to streams and rivers in the upper Nooksack basin, and the necessity for a sediment management plan focused on protecting local salmon populations.

With regard to the DHSVM modeling, in addition to the soil and landcover limitations mentioned above with regards to the static model, Murphy (2016) pointed out a number of uncertainties associated with the hydrology modeling. Specifically, the disaggregation of extrapolated daily meteorology grids, generalizations about several climate parameters associated with GCM climate forecasts, and the relatively coarse resolution of the GCM climate forecasts introduce uncertainty into the hydrology modeling (Murphy, 2016). Note too, that all historical and forecasted simulations use the same 2011 NOAA landcover. Projected landcover changes such as harvesting or tree growth, and subsequent changes in rooting depths and root cohesion are not considered. None the less, the model serves as a rigorous tool for estimating the probability of failure and making qualitative, relative comparisons between the stability of hillslopes, and for identifying areas that should be selected for additional analysis.

5.4 Mass-Wasting Susceptibility Mapping

The output of the DHSVM mass-wasting model are pixel locations that have a high probability of failure, which are typically isolated in small areas because of soil heterogeneities in mechanical properties and degrees of saturation (Figure 17-21). Hence, they do not serve well as susceptibility maps. As such, I produced the LSZ maps to identify areas having similar failure attributes as the factors associated with the high failure probabilities produced by the DHSVM (Figure 26). The susceptible areas derived from LSZ maps are more extensive hence serve as broader, less specific tool for slope susceptibility assessment (Figure 26). Note, however, that the range of LSI values generated for the maps are based off of failure probabilities, which were split into five equal intervals, with the top twenty percent representing very high susceptible areas (Saha et al., 2005). Therefore, very high susceptible areas are not represented by the same LSI values, which are dictated by the snow coverage and precipitation characteristics of the related storm. Very high susceptible areas give an indication of the most susceptible areas based on the unique storm characteristics, and should be used as a general comparison between storm events.

An advantage of applying the more complex DHSVM mass-wasting model is that it accounts for uncertainty and variability in the soil and vegetation mechanical properties and for more natural soil-water conditions produced by the hydrology model in the DHSVM (Doten et al., 2006). To determine the effectiveness of applying the simpler static ArcGIS method as a tool for infinite-slope susceptibility mapping, I compared overlapping areas from the FS < 1.5 map with the LSZ map generated from outputs for a late century winter storm. Within the North, Middle and South Fork basins, 79.9%, 78.2%, and 54.7%, respectively, of 'very high' susceptible areas fall within susceptible areas (FS < 1.5) derived from static modeling (Figure 27). The lower percentage in the South Fork basin may be due to the distribution of soil depths in the lower relief South Fork basin relative to the higher relief Middle and North Fork basins. While static modeling produces more susceptible areas than highly susceptible areas from LSZ maps, isolated areas identified by both methods could be regions to focus additional study. Given the reasonable correlation between the two models, the static ArcGIS would serve as a reasonable first-order tool for identifying susceptible slopes. The static model does however, account for a more realistic soil-thicknesses, unconsolidated deposit mechanical strength variability, and vegetation root cohesion strength variability in a watershed, unlike the WADNR infinite-slope model.

6.0 Conclusion

Projected warming and changes in precipitation are likely to drive significant increases in mass-wasting susceptibility and subsequent sediment production in the Nooksack basin affecting water quality, salmon habitat and flood hazard risk. Modeling indicates that snowpack will develop later in the fall, melt out earlier in the spring, with winter snowpack restricted to higher elevations into the 21st century. As the snowpack diminishes, there will be a significant increase in forest roads, and harvestable forest area exposed to winter rainfall. While these elements increase sediment production, the variability of their effects rely heavily on complex human decisions. There will be a large increase in slopes measuring greater than 25° and previously mapped landslides, which are documented to increase mass-wasting in drainages feeding tributaries of the Nooksack River. Glaciers will retreat leaving at least an additional 2 km^2 of exposed moraines that have the potential to erode and fail, primarily during large storm events when the snowpack is at a minimum in the fall and early spring. Susceptibility maps produced by

the static ArcGIS model and the DHSVM sediment module indicate an increase in regions susceptible to slope failure during the winter months in snow free areas at higher elevations. As expected, higher mass-wasting susceptibility was associated with more saturated slopes greater than about 30° having thicker deposits with lower mechanical strength, e.g., sand (SW), loamy sand (GP, GM), sandy loam (ML-MG), silt, moraines, glacial outwash (Qgoe) and former landslide deposits. The more user-friendly static ArcGIS raster-based method proved to be a useful tool for identifying highly susceptible areas that have the potential to deliver sediment to steams, compared to the more rigorous and complicated probabilistic method integrated into the DHSVM hydrology model. Identifying susceptible areas with such models can assist hazard planning, and mitigating the effects of sediment on fish habitat and protecting future salmon populations.

7.0 References

Abatzoglou, J.T., and Brown, T.J., 2012, A comparison of statistical downscaling methods suited for wildfire applications: *International Journal Climatology*, Vol. 32, pp. 772–780, doi 10.1002/joc.2312

Abatzoglou, J.T., Rupp, D.E., and Mote, P.W., 2014, Seasonal Climate Variability and Change in the Pacific Northwest of the United States: *Journal Climate*, Vol. 27, pp. 2125–2142, doi: 10.1175/JCLI-D-13-00218.1

Anderson, S.W., Keith, M.K., Magirl, C.S., Wallick, J.R., Mastin, M.C., and Foreman, J.R., 2017, *Geomorphic response of the North Fork Stillaguamish River to the State Route 530 landslide near Oso, Washington*: U.S. Geological Survey Scientific Investigations Report 2017–5055, 85 p., https://doi.org/10.3133/sir20175055

Anderson, S.W., Konrad, C.P., Grossman, E.E., Curran, C., 2018, *Sediment storage and transport in the Nooksack River basin from 2006-2015*, USGS Scientific Report 2018.

Barik, M.G., Adam, J.C., Barber, M.E., and Muhunthan, B., 2017, Improved landslide susceptibility prediction for sustainable forest management in an altered climate: *Engineering Geology*, Vol. 230, pp. 104-117.

Battin, J., Wiley, M.W., Ruckelshaus, M.H., Palmer, R.N., Korb, E., Bartz, K.K., and Imaki, H., 2007, *Projected impacts of climate change on salmon habitat restoration*. Proceedings of the National Academy of Sciences of the United States of America, Vol. 104, No. 16, pp. 6720-6725.

Baum, R.L., and Godt, J.W., 2010, Early warning of rainfall-induced shallow landslides and debris flows in the USA: *Landslides*, Vol. 7, No. 3, pp. 259–272. https://doi.org/10.1007/s10346-009-0177-0

Baum, R., Harp, E., and Highland, L., 2007, *Landslide Hazards in the Seattle, Washington area*: U.S. Geological Survey Fact Sheet 2007-3005, 4 p.

Berry, K., 2017, *Skagit County Comprehensive Plan and Zoning Districts*: Skagit County GIS data set, available at http://skagitcounty.net/Departments/GIS/Digital/compplan.htm

Booth, D.B., 1991, Glacier Physics of the Puget Lobe, Southwest Cordilleran Ice Sheet: *Géographie physique et Quaternaire*, Vol. 45, No. 3, pp. 301–315. doi:10.7202/032877ar

Booth, D.B., Haugerud, R.A., and Troost, K.G., 2003, *Restoration of Puget Sound Rivers:* University of Washington Press, Seattle, WA. Chapter 2 in: Montgomery, D.R., S. Bolton, D.B. Booth, and L. Wall (eds.), The geology of Puget Sound lowland rivers, pp. 15-45.

Bowling, L.C., Storck, P., and Lettenmaier, D.P., 2000, Hydrologic effects of logging in western Washington, United States: *Water Resources Research*, Vol. 36, No. 11, pp. 3223-3240.

Brown, J., 2011, *The impact of fine sediment pollution on Chinook survival to emergence in the North Fork Stillaguamish River*: Stillaguamish Tribe of Indians, Natural Resources Department. 39 p.

Brunengo, M.J., Smith, S.D., Bernath, S.C., 1992, *Screening for watershed analysis - a GIS-based method of modeling water input from rain-on-snow storms, for management and regulation of clearcut forest harvest*: Washington Department of Natural Resources, Forest Practices Division. Open-file report 92-2.

Burns, W.J., Madin, I.P., Mickelson, K.A., 2012, *Protocol for shallow-landslide susceptibility mapping*: Oregon Department of Geology and Mineral Industries Special Paper 45, 38 p.

Burton, A., and Bathrust, J.C., 1998, Physically based modelling of shallow landslide sediment yield at a catchment scale: *Environmental Geology*, Vol. 35, No. 2-3, pp. 89-99.

Chleborad, A.F., Baum, R.L., and Godt, J.W., 2006, *Rainfall thresholds for forecasting landslides in the Seattle, Washington, area—Exceedance and probability*: U.S. Geological Survey Open-File Report 2006–1064, 31 p., http://pubs.usgs.gov/of/2006/1064/

Cuo, L., Pagano, T.C., and Wang, Q.J., 2011, A Review of Quantitative Precipitation Forecasts and Their Use in Short to Medium Range Streamflow Forecasting: *Journal Hydrometeorology,* Vol. 12, No. 5, pp. 713-728.

Czuba, J.A., Magirl, C.S., Czuba, C.R., Grossman, E.E., Curran, C.A., Gendaszek, A.S., and Dinicola, R.S., 2011, *Sediment Load from Major Rivers into Puget Sound and its Adjacent Waters*: United States Geological Survey Fact Sheet 2011-3083. 4 p.

Czuba, J.A., Olsen, T.D., Czuba, C.R., Magirl, C.S., and Gish, C.C., 2012, *Changes in sediment volume in Alder Lake, Nisqually River Basin, Washington, 1945–2011*: U.S. Geological Survey Open-File Report 2012–1068, 30 p.

Deser, C., Knutti, R., Solomon, S., and Phillips, A.S., 2012, Communication of the role of natural variability in future North American climate: *Nature Climate Change*, Vol. 2, pp. 775–779, doi: 10.1038/nclimate1562

Dhakal, A. S., and Sidle, R. C., 2004, Pore water pressure assessment in a forest watershed: simulations and distributed field measurements related to forest practices: *Water Resources Research*, Vol. 40, No. 2, pp. 757-776.

Dickerson, S.E., 2010, *Modeling the effects of climate change forecasts on streamflow in the Nooksack River basin*: M.S. Thesis, Department of Geological Sciences, Western Washington University, Bellingham, WA, 132 p.

Dickerson-Lange, S.E. and Mitchell, R., 2013, Modeling the effects of climate change projections on streamflow in the Nooksack River basin, Northwest Washington: *Hydrological Processes*. DOI: 10.1002/hyp.10012

Doten, C.O., and Lettenmaier, D.P., 2004. Prediction of Sediment Erosion and Transport with the Distributed Hydrology-Soil-Vegetation Model: *Water Resources*, Technical Report No. 178

Doten, C.O., Bowling, L.C., Lanini, J.S., Maurer, E.P., and Lettenmaier, D.P., 2006, A spatially distributed model for the dynamic prediction of sediment erosion and transport in mountainous forested watersheds: *Water Resources*, Vol. 42, No. 4, W04417, doi: 10.1029/2004WR003829

Elsner, M.M., and Hamlet, A., 2010, *Macro-scale Hydrologic Model Implementation*: Columbia Basin Climate Change Scenarios Project (PI: Alan F. Hamlet), University of Washington, Seattle, WA, 31 pp, available from: http://www.hydro.washington.edu/2860/report/

EPA, Nooksack Indian Tribe, and Tetra Tech, Inc., 2015, *Webinar: Qualitative Assessment Findings and Recommendations, May 19, 2015*. A part of the project: Qualitative Assessment: Evaluating the Impacts of Climate Change on Endangered Species Act Recovery Actions for the South Fork Nooksack River, WA, Draft Final, March 2015.

Flannagan, S., 1999, *Woody debris transport through low-order stream channels of northwest California – Implications for road stream crossing failure*: MS thesis, Humboldt State University, Arcata, California, 114 p.

Fredriksen, R. L., 1970, *Erosion and sedimentation following road construction and timber harvest on unstable soils in three small western Oregon watersheds*: U.S. Department of Agriculture Forest Service Research Paper PNW-104, 15 p.

García-Gaines, R.A. and Frankenstein, S., 2015, USCS and the USDA Soil Classification System: Development of a Mapping Scheme: *Engineer Research and Development Center, Hanover, NH, Cold Regions Research and Engineering Laboratory*, UPRM and ERDC Educational and Research Internship Program, U.S. Army Corps of Engineers, 46 p.

Geotechdata.info, 2013, *Angle of friction*: Available at http://geotechdata.info/parameter/angle-of-friction.html

Geotechdata.info, 2013, *Cohesion*: Available at http://geotechdata.info/parameter/cohesion.html

Geotechdata.info, 2013, *Dry unit weight*: Available at http://geotechdata.info/parameter/soil-dry-unit-weight.html

Godt, J.W., Baum, R.L, and Chleborad, A.F., 2006, Rainfall characteristics for shallow landsliding in Seattle, Washington, USA: *Earth Surface Processes and Landforms*, Vol. 31, No. 1, pp. 97–110, https://doi.org/10.1002/esp.1237

Hammond, C., Hall, D., Miller, S., Swetik, P., 1992, *Level I Stability Analysis (LISA) Documentation for Version 2.0.*: United States Department of Agriculture Intermountain Research Station General Technical Report INT-285, 190 p.

Harp, E.L., Michael, J.A., and Laprade, W.T., 2006, *Shallow-Landslide Hazard Map of Seattle, Washington*: U.S. Geological Survey Open-File Report 2006-1139, 20 p.

IPCC, 2013, *Climate Change 2013*: *The Physical Science Basis. Contribution of Working Group I to the Fifth Assessment Report of the Intergovernmental Panel on Climate Change* [Stocker, T.F., D. Qin, G.-K. Plattner, M. Tignor, S.K. Allen, J. Boschung, A. Nauels, Y. Xia, V. Bex and P.M. Midgley (eds.)]. Cambridge University Press, Cambridge, United Kingdom and New York, NY, USA, 1535 pp., doi:10.1017/CBO9781107415324

Isaak, D.J., Luce, C.H., Rieman, B.E., Nagel, D.E., Peterson, E.E., Horan, D.L., Parkes, S., and Chandler, G.L., 2010, Effects of climate change and wildlife on stream temperatures and salmonid thermal habitat in a mountain river network. *Ecological Applications*, Vol. 20, No. 5, pp. 1350-1371.

Jaeger, K.L., Curran, C.A., Anderson, S.W., Morris, S.T., Moran, P.W., and Reams, K.A., 2017, *Suspended sediment, turbidity, and stream water temperature in the Sauk River Basin, Washington, water years 2012–16*: U.S. Geological Survey Scientific Investigations Report 2017–5113, 47 p., https://doi.org/10.3133/sir20175113

Jiménez Cisneros, B.E., Oki, T., Arnell, N.W., Benito, G., Cogley, J.G., Doll, P., Jiang, T., and Mwakalila, S.S., 2014, *Freshwater Resources*, In: Field, C.B., Barros, V.R., Dokkken, D.J., Mach, K.J., Mastrandrea, M.D., Bilir, T.E., Chatterjee, M., Ebi, K.L., Estrada, Y.O., Genova, R.C., Gimma, B., Kissel, E.S., Levy, A.N., MacCracken, S., Mastrandrea, P.R., and White, L.L. (eds.) Climate Change 2014: Impacts, Adaption and Vulnerability. Part A: Global and Sectoral Aspects. Contribution of Working Group II to the Fifth Assessment Report of the Intergovernmental Panel on Climate Change, Cambridge University Press, Cambridge, pp. 229-269.

Kirtland, Jeffrey A., 1995, *Sediment Production and Delivery in the Upper South Fork Nooksack River, Northwest Washington, 1940-1991*: M.S. Thesis, Department of Geology, Western Washington University, Bellingham, WA, 149 p.

Koloski, J.W., Schwarzm, S.D., and Tubbs, D.W., 1989, *Geotechnical Properties of Geologic Materials*: Washington Division of Geology and Earth Resource Bulletin 78, Engineering Geology in Washington, Vol. 1.

Lebourg, T., Riss, J., Pirard, E., 2004, Influence of morphological characteristics of heterogeneous moraine formations on their mechanical behavior using image and statistical analysis: *Engineering Geology*, Vol. 73, No. 1-2, pp. 37-50.

Lee, S.Y., Hamlet, A.F., Grossman, E.E., 2016, Impacts of Climate Change on Regulated Streamflow, Hydrologic Extremes, Hydropower Production, and Sediment Discharge in the Skagit River Basin: *Northwest Science*, Vol. 90, No. 1, pp. 23-43.

Leggat, M.S., Owens, P.N., Stott, T.A., Forrester, B.J., Dery, S.J., Menounos, B., 2015, Hydro-meterological drivers and sources of suspended sediment flux in the pro-glacial zone of the retreating Castle Creek Glacier, Cariboo Mountains, British Columbia, Canada: *Earth Surface Processes and Landforms*, Vol. 40, No. 11, pp. 1542-1559.

Leung L.R., and Wigmosta, M.S., 1999, Potential climate change impacts on mountain watersheds in the Pacific Northwest: *Journal American Water Resources Association*, Vol. 35, No. 6, pp. 1463–1471. doi: 10.1111/j.17521688.1999.tb04230.x

Livneh, B., Bohn, T.J., Pierce, D.W., Munoz-Arriola, F., Nijssen, B., Vose, R., Cayan, D.R., and Brekke, L., 2015, A spatially comprehensive, hydrometeorological data set for Mexico, the U.S. and Southern Canada 1950–2013: *Scientific Data*, Vol. 2, No. 150042, doi: 10.1038/sdata.2015.42

Lu, N., and Godt, J.W., 2013, *Hillslope Hydrology and Stability*: Cambridge University Press, Cambridge, 458 p.

Lummi Nation Natural Resources Department, 2012, *Logging Road and Sediment Production Assessment for the Skookum and Cavanaugh Creek Watersheds of the South Fork Nooksack River*: Lummi Natural Resources Department, 79 p.

Lummi Nation Natural Resources Department, 2015, *Current and Historic Sediment Production, Storage, and Delivery to the South Fork Nooksack Within the Elk Flats Sub-basin:* Lummi Natural Resources Department, 49 p.

Malick, G., 2018, *Geologic Development and Ongoing Activity of the Van Zandt Landslide Complex, Northwest WA, USA*: M.S. Thesis, Department of Geology, Western Washington University, Bellingham, WA, 96 p.

Mantua, N.J., and Hare, S.R., 2002, The Pacific Decadal Oscillation: *Journal of Oceanography*, Vol. 58, No. 1, pp. 35–44.

Mass, C., 2015, *The Winter of 2070*: Available at http://cliffmass.blogspot.com/2015/02/the-winter-of-2070.html

Mauger, G.S., Casola, J.H., Morgan, H.A., Strauch, R.L., Jones, B., Curry, B., Busch Isaken, T.M., Whitely Binder, L., Krosby, M.B., and Snover, A.K., 2015, *State of Knowledge: Climate Change in Puget Sound*: Climate Impacts Group, University of Washington, Seattle, WA, doi: 10.7915/CIG93777D

McWethy, G., 2016, *Upper Nooksack Basin—LiDAR data*: Washington Division of Geology and Earth Resources Digital Data.

Mickelson, K.A., Jacobacci, K.E., Contreras, T.A., Biel, A., Slaughter, S.L., 2017, *Landslide inventory, susceptibility, and exposure analysis of Pierce County, Washington*: Washington Geological Survey Report of Investigation 39, 16 p.

Mitchell, R., Murphy, R., Bandaragoda, C., and Grah, O., 2016, *Impacts of Forecasted Climate Change on Snowpack in the Nooksack River Basin*, presented at the 2016 Mountain Climate (MtnClim) Conference, Leavenworth, WA, October 17-21, 2016.

Montgomery, D. R., Schmidt, K. M., Dietrich, W. E., and Greenberg, H., 2000, Forest clearing and regional landsliding: *Geology*, Vol. 28, No. 4, pp. 311–314.

Montgomery, D.R., Sullivan, K., Greenberg, H.M., 1998, Regional test of a model for shallow landsliding: *Hydrological Processes*, Vol. 12, No. 6, pp. 943-955.

Moore, R.D., Fleming, S.W., Menounos, B., Wheate, R., Fountain, A., Stahl, K., Holm, K., Jakob, M., 2009, Glacier change in western North America: influences on hydrology, geomorphic hazards and water quality: *Hydrological Processes,* Vol. 23, No. 1, pp. 42-61.

Morgan, H., Norheim, R., and Krosby, M., 2017, *Maps of Climate and Hydrologic Change for the Nooksack River Watershed*: Climate Impacts Group, University of Washington.

Mote, P.W., and Salathé Jr., E.P., 2010, Future climate in the Pacific Northwest: *Climatic Change*, Vol. 102, No. 1-2, pp. 29–50, doi: 10.1007/s10584-010-9848-z

Mote, P., Snover, A.K., Capalbo, S., Eigenbrode, S.D., and Littell, J., 2014, Northwest. In Melillo, J., Richmond, T.C., and Yohe, W. (Eds), *Climate Change Impacts in the United States: The Third U.S. National Climate Assessment*. U.S. Global Change Research Program, 841 p.

Mount Baker Volcano Research Center, 2018, *Eruptive History*: Available at mbvrc.wwu.edu/eruptions/

Murphy, R.D., 2016, *Modeling the Effects of Forecasted Climate Change and Glacier Recession on Late Summer Streamflow in the Upper Nooksack River Basin*: M.S. Thesis, Department of Geology, Western Washington University, Bellingham, WA, 95 p.

National Oceanic and Atmospheric Administration, 2011, *C-CAP Washington 2011-Era Land Cover Map*: National Oceanic and Atmospheric Administration's Ocean Service, Coastal Services Center.

Nature Conservancy and the Climate Impacts Group, 2016, *Adapting to Change: Climate Impacts and Innovation in Puget Sound*, Morse, J., Israel, J., Whitley Binder, L., Mauger, G., and Snover, A.K (Eds), The Nature Conservancy, Seattle, WA. 24 p.

Nielsen, K., and Grah, O., 2015, *Mass Wasting Inventory around Glaciers Located in the Nooksack Watershed on Mount Baker*: Report prepared for the Nooksack Indian Tribe, 19 p.

Nooksack Natural Resources Department, 2016, *Nooksack Indian Tribe 2016 Sediment Assessment Report for the Nooksack River Watershed.* Draft, 114 p.

O'Connor, J.E., Hardison, J.H., Costa, J.E., 2001, *Debris flows from failures of neoglacial-age moraine dams in the Three Sisters and Mount Jefferson wilderness areas*, Oregon, US: Geological Survey Professional Paper 1606, 93 p.

Peak Northwest, 1986, *Nooksack River Basin Erosion and Fishery Studies: Boulder Creek, Canyon Creek, Cornell Creek, Howard Creek, Racehorse Creek*. Report prepared for Lummi Tribal Fisheries Department, 110 p.

Pelto, M., and Brown, C., 2012, Mass balance loss of Mount Baker, Washington glaciers 1990–2010: *Hydrological Processes*, Vol. 26, No. 17, pp. 2601–2607.

Pierce, K., 2017, personal communication, Washington State Department of Fish and Wildlife, 1111 Washington St. SE, Olympia, WA, 98501.

PRISM Climate Group, 2017, *30-Year Normals*, Oregon State University: Available at http://prism.oregonstate.edu

Puget Sound LiDAR Consortium, 2006, *Airborne LiDAR data set*, *Puget Sound Region*: Electronic data set, available at http://pugetsoundlidar.ess.washington.edu/

Reneau, S.L., and Dietrich, W.E., 1987, *Size and location of colluvial landslides in a steep forested landscape*: IAHS Publication 165, pp. 39-48.

Riedel, J.L., Wilson, S., Baccus, W., Larrabee, M., Fudge, T.J., Fountain, A., 2015, Glacier status and contribution to streamflow in the Olympic Mountains, Washington, USA: *Journal Glaciology*, Vol. 61, No. 225, pp. 8-16, doi: 10.3189/2015JoG14J138

Roering, J.J., Schmidt, K.M., Stock, J.D., Dietrich, W.E., and Montgomery, D. R., 2003, Shallow landsliding, root reinforcement, and the spatial distribution of trees in the Oregon Coast Range: *Canadian Geotechnical Journal*, Vol. 40, No. 2, pp. 237-253, doi: 10.1139/t02-113

Saha, A.K., Gupta, R.P., Sarkar, I., Arora, M.K., Csaplovics, E., 2005, An approach for GIS-based statistical landslide susceptibility zonation – with a case study in the Himalayas: *Landslides*, Vol. 2, No. 1, pp. 61-69.

Salathé Jr., E.P., Leung, L.R., Qian, Y., and Zhang, Y., 2010, Regional climate model projections for the State of Washington: *Climatic Change*, Vol. 102, No. 1-2, pp. 51-75.

Savage, W.Z., Morrissey, M.M., Baum, R.L., 2000, *Geotechnical Properties for Landslide-Prone Seattle-Area Glacial Deposits*: U.S. Geological Survey Open-File Report 00-228, 5 p.

Scheevel, C.R., Baum, R.L., Mirus, B.B., and Smith, J.B., 2017, *Precipitation thresholds for landslide occurrence near Seattle, Mukilteo, and Everett, Washington*: U.S. Geological Survey Open-File Report 2017–1039, 51 p., https://doi.org/10.3133/ofr20171039

Selby, M.J., 1982, *Hillslope Materials and Processes*, Oxford University Press, Oxford, 480 p.

Sidle, R.C., and Bogaard, T.A., 2016, Dynamic Earth System and Ecological Controls of Rainfall Initiated Landslides: *Earth Science Reviews*, Vol. 159, No. 1, pp. 275-291, doi: 10.1016/j.earscirev.2016.05.013

Sidle, R.C., Pearce, A.J. and O'Loughlin, C.L., 1985, *Hillslope stability and land use*, Water Resources Monograph Series, Vol. 11, American Geophysical Union, Washington, D.C., 140 p.

Snover, A.K, Mauger, G.S., Whitely Binder, L.C., Krosby, M., and Tohver, I., 2013, *Climate Change Impacts and Adaptation in Washington State: Technical Summaries for Decision Makers*: State of Knowledge Report prepared for the Washington State Department of Ecology. Climate Impacts Group, University of Washington, Seattle. 130 p.

Soil Survey Staff, 2016, *Skagit County ESRI Soil Shapefile, Soil Survey Geographic (SSURGO) Database*: Available at https://sdmdataaccess.sc.egov.usda.gov

Soil Survey Staff, 2016, *Whatcom County ESRI Soil Shapefile, Soil Survey Geographic (SSURGO) Database*: Available at https://sdmdataaccess.sc.egov.usda.gov

Sperna Weiland, F.C., Van Beek, L.P.H., Kwadijk, J.C.J., and Bierkens, M.F.P., 2010, The ability of a GCM-forced hydrological model to reproduce global discharge variability: *Hydrology and Earth System Sciences*, Vol. 14, No. 8, pp. 1595–1621.

Stead, D., and Coggan, J., 2012, Numerical modeling of rock-slope instability. In Clague, J.J., and Stead, D. (Eds), *Landslides: Types, Mechanisms and Modeling*. Cambridge University Press, Cambridge, 144 p.

Tabor, R.W., Booth, D.B., Vance, J.A., and Ford, A.B., 1989, *Geologic Map of the Sauk River 30-by 60-Minute Quadrangle*, *Washington*: U.S. Department of the Interior, U.S. Geological Survey, Geologic Investigations Series I-2592, scale 1:100,000.

Tabor, R.W., Haugerud, R.A., Hildreth, W., and Brown, E.H., 2003, *Geologic Map of the Mount Baker 30- by 60-Minute Quadrangle, Washington*: U.S. Department of the Interior, U.S. Geological Survey, Geologic Investigations Series I-2660, scale 1:100,000.

Tucker, D.S., Scott, K.M., Grossman, E.E., Linneman, S., 2014, *Mount Baker lahars and debris flows, ancient, modern, and future*: GSA Field Guides, Vol. 38, pp. 33-52.

Turner, K.A., and Schuster, R.L., 1996, *Landslides: Investigation and Mitigation*: National Academy Press, Washington, D.C., Transportation Research Board Special Report 247, 673 p.

van Westen, C.J., 1997, *Statistical landslide hazard analysis*. In: Application guide, ILWIS 2.1 for Windows. ITC, Enschede, Netherlands, pp. 73–84.

WADNR, Washington Department of Natural Resources, 2017, *DNR Active Roads Feature Service*: Available at http://geo.wa.gov/datasets/bfdb0455c3b24aa6ae46c9502f814c25_5

WADNR, Washington Department of Natural Resources, 2018, *Shallow Landslide Hazard Forecast Map*: Available at www.dnr.wa.gov/slhfm

Washington Division of Geology and Earth Resources, 2016, *Landslides and landforms--GIS data*: Available at: dnr.wa.gov/publications/ger_readme_landslides_landforms.htm

Washington Division of Geology and Earth Resources, 2016, *Surface geology, 1:100,000--GIS data*: Available at: dnr.wa.gov/publications/ger_metadata_100k_surface_geology_geodatabase.htm

Watanabe, S., Kanae, S., Seto, S., Yeh, P.J.-F., Hirabayashi, Y., and Oki, T., 2012, : *Journal Geophysical Research*: *Atmospheres*, Vol. 117, No. D23, pp. D23114, doi: 10.1029/2012JD018192

Weatherly, H., 2005, *Nooksack River Sediment Management Plan: Summary of Background Information*: Kerr Wood Leidal, prepared for Whatcom County Flood Control Zone District. 144 p.

Wemple, B.C., Swanson, F.J., and Jones, J.A., 2001, Forest Roads and Geomorphic Process Interactions, Cascade Range, Oregon: *Earth Surface Processes and Landforms*, Vol. 26, No. 2, pp. 191-204.

Wigmosta, M.S., Vail, L.W., and Lettenmaier, D.P., 1994, A distributed hydrology-vegetation model for complex terrain: *Water Resources Research*, Vol. 30, No. 6, pp. 1665–1679.

Wu, W., and Sidle, R. C., 1995, A distributed slope stability model for steep forested basins: *Water Resources Research,* Vol. 31, No. 8, pp. 2097-2110.

United States Department of Agriculture, 2006, *Middle Fork and South Fork Nooksack Rivers Watershed Analysis*: USDA, Forest Service Pacific Northwest Region, 150 p.

United States Department of Agriculture, 2015, *Whatcom County Colored Digital* Orthophoto: USDA, scale 1:12,000.

United States Department of Agriculture Forest Service, 1991, *Mt. Baker-Snoqualmie National Forest Soil Resource Inventory Shapefile*: USDA, scale 1:62,500, available at https://www.fs.fed.us/r6/data-library/gis/mtbaker-snoqualmie/

United States Geological Survey, 2018, *Discharge at USGS 12210700 Nooksack River at North Cedarville, WA*: Available at b//waterdata.usgs.gov/wa/nwis/inventory/?site_no=12210700&agency_cd=USGS.

8.0 Tables

Table 1. Total basin areas (km^2), areas above 500, 1,000, 1,500, and 2,000 meters, and glacial area in each of the three upper basins of the Nooksack River.

	Basin Area	Area > 500m	Area > 1000m	Area > 1500m	Area > 2000m	2009 Glacier Area
North Fork	817.1	230.5	366.2	128.6	18.6	25.8
Middle Fork	259.7	220.1	127.0	27.9	7.2	7.6
South Fork	475.8	310.6	118.1	8.8	0.04	0.0

Table 2. Average mechanical soil characteristics assigned to surficial units used in the static infinite-slope equation.

Surficial Unit	c (kPa)	φ (°)	γ(kN/m^3)	γ_s (kN/m^3)
CL (Clay Loam)	20.0	27	18.8	20.1
CL-ML (Silty Clay)	18.0	25	18.8	20.1
GM (Loamy Sand)	0.0	35	21.5	24.0
GP (Loamy Sand)	0.0	36	20.5	24.0
ML (Silt)	0.0	33	18.8	20.1
ML-MG (Sandy Loam)	0.0	35	18.8	20.1
ML-MS (Silty Loam)	0.0	36	18.8	20.1
OH (Organic)	10.0	22	18.8	20.1
OL (Organic)	10.0	25	18.8	20.1
PT (Muck)	0.0	10	18.8	20.1
Qa	0.0	32	18.8	20.1
Qad	19.2	33	18.7	21.2
Qaf	9.6	30	18.8	20.1
Qgo(e)	14.4	34	18.7	21.2
Qgt	28.7	30	18.8	20.9
Qls	19.2	32	18.8	20.1
Qm	5.0	38	18.8	20.1
Qta	0.0	36	18.8	20.1
SM (Sandy Loam)	22.0	34	20.5	24.0
SM-SC (Sandy Clay Loam)	20.0	31	19.5	23.0
SM-SG (Loamy Sand)	18.0	32	20.0	24.0
SW (Sand)	0.0	35	20.5	24.0

Table 3. Conversion of NOAA landcover classification to DHSVM landcover classification.

NOAA Landcover Classification	DHSVM Landcover Classification
2, Developed, High Intensity	13, Developed
3, Developed, High Intensity	13, Developed
4, Developed, High Intensity	13, Developed
5, Developed, Open Space	12, Bare
6, Cultivated Crops	11, Cropland
7, Pasture/Hay	10, Grassland
8, Grassland/Herbaceous	10, Grassland
9, Deciduous Forest	4, Deciduous Forest
10, Evergreen Forest	1, Evergreen Needleleaf
11, Mixed Forest	5, Mixed Forest
12, Scrub/Shrub	8, Closed Shrub
13, Palustrine Forested Wetland	4, Deciduous Forest
14, Palustrine Scrub/Shrub Wetland	8, Closed Shrub
15, Palustrine Emergent Wetland	10, Grassland
16, Estuarine Forested Wetland	4, Deciduous Forest
17, Estuarine Scrub/Shrub Wetland	8, Closed Shrub
18, Estuarine Emergent Wetland	10, Grassland
19, Unconsolidated Shore	12, Bare
20, Barren Land	12, Bare
21, Open Water	14, Water
22, Palustrine Aquatic Bed	14, Water
23, Estuarine Aquatic Bed	14, Water
24, Tundra	20, Ice
25, Perennial Ice/Snow	20, Ice

Table 4. Root cohesion (kPa) and vegetation surcharge ($\frac{kg}{m^2}$) values applied to vegetation coverages in the ArcGIS and DHSVM models.

Parameter (ArcGIS Vegetation)		Deterministic	Probability Distribution	Range	Mean / Mode	Standard Deviation
Large Conifer (1)	Root Cohesion	7.0	Triangular	12 - 23	17.0	-
	Vegetation Surcharge	-	Uniform	48.9 – 195.4	-	-
Mixed Stand (5)	Root Cohesion	7.0	Triangular	2 - 17	9.5	-
	Vegetation Surcharge	-	Uniform	48.9 – 195.4	-	-
Urban (13)	Root Cohesion	0.0	Normal	-	2000	0.0
	Vegetation Surcharge	-	Normal	-	0.0	0.0
Broadleaf (4)	Root Cohesion	7.0	Triangular	2 - 13	5.5	-
	Vegetation Surcharge	-	Uniform	48.9 – 195.4	-	-
Barren (12)	Root Cohesion	0.0	Normal	-	2000	0.0
	Vegetation Surcharge	-	Normal	-	0.0	0.0
Shrubland (8)	Root Cohesion	4.0	Triangular	2 - 6	4.0	-
	Vegetation Surcharge	-	Uniform	0 - 5	-	-
Cropland (11)	Root Cohesion	1.0	Triangular	1 - 2	-	-
	Vegetation Surcharge	-	Uniform	0 - 5	-	-
Rock (12)	Root Cohesion	0.0	Normal	-	2000	0.0
	Vegetation Surcharge	-	Normal	-	0.0	0.0
Water (14)	Root Cohesion	0.0	Normal	-	2000	0.0
	Vegetation Surcharge	-	Normal	-	0.0	0.0
Grassland (10)	Root Cohesion	1.0	Triangular	2 - 6	4.0	-
	Vegetation Surcharge	-	Uniform	0 - 5	-	-

Table 5. Probability distributions of cohesion (kPa) and friction angle (degrees) applied to surficial units used in DHSVM.

Parameter		Probability Distribution	Range	Mean / Mode	Standard Deviation
Sand (SW)	Cohesion	Normal	-	0.75	0.25
	Friction Angle	Normal	-	33.0	1.5
Sand (Qgoe)	Cohesion	Normal	-	0.75	0.25
	Friction Angle	Normal	-	33.0	1.5
Loamy Sand (SM –SG)	Cohesion	Normal	-	12.0	7.0
	Friction Angle	Normal	-	33.0	1.5
Loamy Sand (GP)	Cohesion	Normal	-	0.75	0.25
	Friction Angle	Uniform	32 - 44	-	-
Loamy Sand (GM)	Cohesion	Normal	-	0.75	0.25
	Friction Angle	Uniform	30 - 40	-	-
Loamy Sand (Qa)	Cohesion	Normal	-	0.75	0.25
	Friction Angle	Uniform	30 - 35	-	-
Loamy Sand (Qls)	Cohesion	Uniform	7.5 - 13	-	-
	Friction Angle	Uniform	25 - 32	-	-
Sandy Loam (Qaf)	Cohesion	Normal	-	9.75	5.0
	Friction Angle	Uniform	27 - 35	-	-
Sandy Loam (SM)	Cohesion	Normal	-	18.0	7.0
	Friction Angle	Uniform	30 - 35	-	-
Sandy Loam (ML-MG)	Cohesion	Normal	-	9.75	5.0
	Friction Angle	Uniform	27 - 35	-	-
Silty Loam (ML-MS)	Cohesion	Normal	-	12.75	7.0
	Friction Angle	Uniform	29 - 38	-	-
Silt (ML)	Cohesion	Normal	-	7.0	3.0
	Friction Angle	Uniform	27 - 41	-	-
Silt (Qgt)	Cohesion	Uniform	20 - 40	-	-
	Friction Angle	Uniform	35 - 45	-	-
Sandy Clay Loam (SM – SC)	Cohesion	Uniform	8 - 25	-	-
	Friction Angle	Uniform	30 - 38	-	-
Clay Loam (CL)	Cohesion	Uniform	4 - 10	-	-
	Friction Angle	Uniform	25 - 32	-	-
Sandy Clay (Qad)	Cohesion	Uniform	7.5 - 13	-	-
	Friction Angle	Uniform	25 - 32	-	-
Silty Clay (CL-ML)	Cohesion	Uniform	7.5 - 13	-	-
	Friction Angle	Uniform	25 - 32	-	-
Organic (OH)	Cohesion	Normal	-	22.0	8.0
	Friction Angle	Uniform	17 - 35	-	-
Organic (OL)	Cohesion	Normal	-	22.0	8.0
	Friction Angle	Uniform	22 - 32	-	-
Muck (PT)	Cohesion	Normal	-	10.0	7.0
	Friction Angle	Uniform	17 - 35	-	-
Talus (Qta)	Cohesion	Normal	-	0.75	0.25
	Friction Angle	Normal	-	33.0	1.5
Loamy Sand (Qm)	Cohesion	Normal	-	0.75	0.25
	Friction Angle	Uniform	30 - 40	-	-
Water	Cohesion	Normal	-	2000	0.0
	Friction Angle	Normal	-	45.0	0.0
Bedrock	Cohesion	Normal	-	2000	0.0
	Friction Angle	Normal	-	45.0	0.0

Table 6. Landscape changes from historical to projected 2075 median snow coverages within each upper basin

Basin	Period	Snow Coverage		Slopes > 25°		Roads		Forest Practices	
		% Basin	% Reduction	% Basin	% Increase	Basin (km)	% Increase	Basin (km^2)	% Increase
South Fork	Historical	52	-	23.4	-	650	-	166.5	-
	Projected	19	-63	31.2	33.3	1101	69.4	306.9	84.3
Middle Fork	Historical	63	-	37.6	-	219	-	74.6	-
	Projected	23	-65	48.6	39.3	499	82.6	131.3	76.0
North Fork	Historical	64	-	24.7	-	973	-	240.3	-
	Projected	31	-51	37.1	50.2	`454	49.4	310.4	29.2

Table 7. ArcGIS results, area (km^2) of FS < 1.5, for each upper basin with varying grid resolution (10 m and 1 m), soil depth, and water table to soil depth ratio (D_w/D).

	Soil Depth Range (m)	D_w/D = 0.7 (10m)	D_w/D = 0.7 (1m*)	D_w/D = 0.95 (10m)	D_w/D = 0.95 (1m*)
NF	0.76 – 3.5	157.7	218.0	203.4	264.3
	2.0 – 3.5	277.6	354.0	317.0	385.6
MF	0.76 – 3.5	48.3	76.0	61.9	91.9
	2.0 – 3.5	91.7	129.7	103.9	137.7
SF	0.76 – 3.5	74.0	124.3	93.6	141.6
	2.0 – 3.5	114.5	173.5	133.3	188.9

*10 m resolution used where 1 m resolution was not available

Table 8. Area of digitized moraine deposits (km^2) for historical and projected landscapes within the North and Middle Fork basins.

	Historical (2017)	Projected (2080)
NF	2.50	4.04
MF	2.28	2.58

Table 9. InfoVal weights calculated from ArcGIS static results (FS < 1.5) for failure factors within each upper basin.

Classes	NF	MF	SF
Slopes 0 - 15°	-3.29	-4.50	-2.67
Slopes 15 - 30°	-0.36	-0.50	-0.09
Slopes 30 - 45°	0.88	0.78	1.02
Slopes 45 - 60°	0.86	0.55	0.82
Slopes 60+°	0.37	0.01	0.44
1 (Sand, SW)	-	-	0.01
2 (Sand, Qgoe)	-5.77	-4.67	-3.91
3 (Loamy Sand, SM-SG)	-5.26	-3.06	-
4 (Loamy Sand, GP)	0.58	0.64	1.24
5 (Loamy Sand, GM)	0.72	0.70	0.81
6 (Loamy Sand, Qa)	-0.94	-0.47	-1.70
7 (Loamy Sand, Qls)	-3.99	-3.30	-3.74
8 (Sandy Loam, Qaf)	-3.39	-3.36	-2.91
9 (Sandy Loam, SM)	-4.06	-3.64	-4.49
10 (Sandy Loam, ML-MG)	0.46	0.52	1.01
11 (Silty Loam, ML-MS)	0.49	-0.11	-0.20
12 (Silt, ML)	0.80	1.09	1.32
13 (Silt, Qgt)	-4.64	-3.18	-4.99
14 (Sandy Clam Loam, SM-SC)	-0.71	0.75	-3.00
15 (Clay Loam, CL)	-3.00	-	-3.00
16 (Sandy Clay, Qad)	-5.22	-5.11	-4.91
17 (Silty Clay, CL-ML)	-3.00	-3.00	-
18 (Organic, OH)	-0.95	-4.64	-2.75
19 (Organic, OL)	-1.93	-2.50	-2.79
22 (Muck, PT)	1.11	0.82	1.37
23 (Talus, Qta)	0.96	1.12	0.95
24 (Loamy Sand, Qm)	0.96	1.00	1.45
Soil Depth 0.76 - 1 m	0.40	0.16	0.41
Soil Depth 1.0 - 2.0 m	-0.09	-0.03	0.07
Soil Depth 2.0 - 3.5 m	-2.42	-0.77	-3.43
1 (Large Conifer)	0.10	0.13	0.11
4 (Broadleaf)	-0.54	-0.32	-0.35
5 (Mixed Stand)	-0.18	-0.16	-0.30
8 (Shrubland)	0.28	-0.01	0.14
10 (Grassland)	-0.24	-0.34	-0.42
11 (Cropland)	-0.25	0.27	-0.63
12 (Rock)	-0.66	-0.82	-0.21
13 (Urban)	-0.46	0.49	-0.21
14 (Water)	-1.30	-2.54	-1.70
20 (Ice)	-2.43	-4.91	-2.40

Table 10. Cumulative precipitation values for fall storms within each upper basin used in DHSVM.

	North Fork		Middle Fork		South Fork	
10/20/2003	Meters	Inches	Meters	Inches	Meters	Inches
72 hours	0.160	6.311	0.177	6.961	0.166	6.553
48 hours	0.128	5.057	0.141	5.567	0.134	5.290
24 hours	0.090	3.561	0.101	3.957	0.099	3.887
12 hours	0.057	2.233	0.063	2.495	0.063	2.487
10/26/2089						
72 hours	0.243	9.556	0.280	11.034	0.264	10.397
48 hours	0.179	7.037	0.204	8.044	0.189	7.434
24 hours	0.138	5.447	0.157	6.163	0.138	5.451
12 hours	0.084	3.294	0.095	3.721	0.083	3.268

Table 11. Cumulative precipitation values for winter storms within each upper basin used in DHSVM.

	North Fork		Middle Fork		South Fork	
01/08/2009	Meters	Inches	Meters	Inches	Meters	Inches
	0.243	9.556	0.280	11.034	0.264	10.397
	0.179	7.037	0.204	8.044	0.189	7.434
	0.138	5.447	0.157	6.163	0.138	5.451
	0.084	3.294	0.095	3.721	0.083	3.268
01/13/2018						
72 hours	0.193	7.602	0.219	8.618	0.249	9.797
48 hours	0.184	7.232	0.206	8.102	0.233	9.192
24 hours	0.135	5.316	0.150	5.902	0.165	6.513
12 hours	0.085	3.358	0.094	3.714	0.103	4.039
02/24/2041						
72 hours	0.111	4.366	0.137	5.376	0.119	4.686
48 hours	0.111	4.366	0.137	5.376	0.119	4.686
24 hours	0.103	4.064	0.127	4.991	0.110	4.339
12 hours	0.064	2.513	0.078	3.085	0.068	2.681
01/08/2089						
72 hours	0.200	7.873	0.212	8.356	0.237	9.330
48 hours	0.180	7.072	0.189	7.460	0.212	8.360
24 hours	0.135	5.328	0.143	5.621	0.157	6.187
12 hours	0.081	3.184	0.085	3.360	0.094	3.685
12/10/2096						
72 hours	0.217	8.539	0.207	8.156	0.202	7.961
48 hours	0.216	8.510	0.206	8.130	0.202	7.944
24 hours	0.174	6.865	0.163	6.419	0.151	5.956
12 hours	0.105	4.144	0.098	3.859	0.090	3.545

Table 12. Areal snow coverage (km^2) during the mass-wasting time step of DHSVM storm events within each upper basin.

	1/2009	1/2018	2/2041	1/2089	12/2096	10/2003	10/2089
NF	722	376	178	75.2	45.9	27.1	2.91
MF	247	116	35.7	16.4	11.6	6.85	0.59
SF	442	152	29.0	5.94	2.60	4.58	0

Table 13. Basin saturation extent of each DHSVM storm, expressed as a percentage of pixels with a water table to soil depth ratio (D_w/D) greater than 0.85.

	1/2009	1/2018	2/2041	1/2089	12/2096	10/2003	10/2089
NF	38.8	74.3	57.3	72.3	81.4	72.8	71.6
MF	36.7	73.3	58.6	68.4	75.1	70.4	72.4
SF	55.5	80.7	60.3	76.5	79.1	74.4	73.1

Table 14. Area (km^2) of failure probabilities (0.25 – 1.0) for historical and projected DHSVM storm events within each upper Nooksack basin.

	North Fork	Middle Fork	South Fork
January 2009	0.68	0.22	1.10
January 2018	2.06	1.13	3.01
January 2089	2.17	1.08	2.50
February 2041	0.72	0.55	1.04
December 2096	2.67	1.14	2.70
October 2003	2.01	0.88	2.24
October 2089	2.20	1.11	2.41

Table 15. Change in area (km^2) of noticeable and high failure probabilities between historical and projected DHSVM storm events within each upper basin.

	Failure Probability	North Fork	Middle Fork	South Fork
1/2009 – 1/2018	0.25 – 1.0	1.37	0.91	1.91
	0.75 – 1.0	0.45	0.32	0.71
1/2009 – 2/2041	0.25 – 1.0	0.04	0.33	-0.06
	0.75 – 1.0	-0.02	0.10	-0.03
1/2009 – 1/2089	0.25 – 1.0	1.49	0.86	1.40
	0.75 – 1.0	0.49	0.31	0.49
1/2009 – 12/2096	0.25 – 1.0	1.99	0.92	1.60
	0.75 – 1.0	0.65	0.32	0.54
10/2003 – 10/2089	0.25 – 1.0	0.19	0.22	0.16
	0.75 – 1.0	-0.0004	0.08	0.03

Table 16. InfoVal weights of saturation percent and surficial unit classes calculated from failure probability results (0.25 – 1.0) for winter DHSVM storms within each upper basin.

Classes	January 2009			January 2018			February 2041			January 2089			December 2096		
	NF	MF	SF	NF	MF	SF	NF	MF	SF	NF	MF	SF	NF	MF	SF
Saturation % 0.1 - 0.3	a	a	a	a	a	a	a	-5.37	a	-6.09	-2.42	-5.81	-5.92	a	a
Saturation % 0.3-0.5	-6.13	a	-5.85	-3.94	-2.65	-4.42	-3.81	-4.35	-5.87	-4.73	-1.56	-4.48	-3.69	-3.61	-5.17
Saturation % 0.5-0.7	-4.34	-4.01	-3.42	-2.10	-2.20	-2.75	-2.25	-2.11	-3.54	-3.78	-1.72	-2.96	-2.14	-2.67	-2.94
Saturation % 0.7-1.0	0.53	0.58	0.34	0.15	0.17	0.12	0.29	0.29	0.23	0.18	0.19	0.15	0.12	0.17	0.13
1 (Sand, SW)	-	-	a	-	-	a	-	-	a	-	-	a	-	-	a
2 (Sand, Qgoe)	-0.36	-0.05	0.11	-2.96	-1.55	0.00	a	a	-0.77	-1.98	-2.75	-0.69	-2.27	-2.05	-0.44
3 (Loamy Sand, SM-SG)	a	a	-	a	a	a	a	a	-	a	a	-	a	a	-
4 (Loamy Sand, GP)	0.71	1.54	-2.20	1.84	1.06	2.31	1.90	1.30	3.21	1.73	1.40	2.53	1.47	0.93	2.48
5 (Loamy Sand, GM)	1.70	1.36	1.36	1.82	1.47	1.35	1.64	1.30	1.33	1.79	1.47	1.38	1.82	1.47	1.37
6 (Loamy Sand, Qa)	0.63	1.37	-1.28	-0.37	-0.07	-1.68	-0.33	0.10	-1.15	-0.20	0.05	-1.67	-0.41	-0.03	-1.64
7 (Loamy Sand, Qls)	-1.53	-1.45	-1.88	-1.80	-1.27	-2.29	-1.70	-0.78	-1.61	-1.81	-1.28	-2.21	-1.90	-1.25	-2.26
8 (Sandy Loam, Qaf)	-2.44	a	a	-3.54	a	a	a	a	a	-4.98	a	a	-4.09	a	a
9 (Sandy Loam, SM)	-2.51	-2.91	-3.06	-3.29	-2.98	-3.05	-5.06	-2.87	-2.75	-3.28	-3.22	-2.81	-3.35	-2.96	-2.86
10 (Sandy Loam, ML-MG)	-5.05	a	-5.85	-5.01	-5.06	-3.97	-4.70	-6.74	-3.12	-5.15	-5.62	-3.81	-5.27	-5.86	-3.86
11 (Silty Loam, ML-MS)	-5.93	a	a	-5.65	a	a	-4.60	a	a	-5.14	a	a	-5.50	a	a
12 (Silt, ML)	-1.24	-1.86	-2.98	-2.35	-2.23	-2.77	-2.54	-3.28	-4.63	-2.19	-2.63	-3.12	-2.02	-2.38	-2.93
13 (Silt, Qgt)	-3.17	a	-2.36	-4.53	-4.21	-2.80	-4.69	-4.59	-2.71	-3.71	-4.58	-2.88	-3.92	-4.63	-2.88
14 (Sandy Clay Loam, SM-SC)	a	a	a	a	a	a	a	a	a	a	a	a	a	a	a
15 (Clay Loam, CL)	a	-	a	a	-	a	a	-	a	a	-	a	a	-	a
16 (Sandy Clay, Qad)	-2.03	-2.01	-3.31	-4.09	-3.80	-3.76	-4.04	-4.18	-3.48	-3.01	-3.49	-3.65	-3.77	-3.78	-3.63
17 (Silty Clay, CL-ML)	a	a	-	a	a	-	a	a	-	a	a	-	a	a	-
18 (Organic, OH)	a	a	a	-2.28	a	a	a	a	a	-3.40	a	a	-2.50	a	a
19 (Organic, OL)	-3.66	-4.08	-3.60	-3.37	-3.02	-3.12	-2.90	-2.95	-3.55	-2.90	-2.72	-2.92	-3.15	-2.74	-3.12
22 (Muck, PT)	-3.54	a	-2.57	-6.03	-3.55	-2.56	-3.89	-2.83	-3.21	-4.48	-3.91	-2.66	-5.60	-3.56	-2.53
23 (Talus, Qta)	0.71	-1.40	-2.07	1.14	0.80	0.38	1.90	0.20	0.00	1.29	0.52	0.20	1.24	0.24	0.18
24 (Loamy Sand, Qm)	a	0.13	a	2.44	2.34	a	3.31	3.07	a	2.26	2.41	a	2.27	2.44	a

[a] represents an arbitrary weight equivalent to -3.00 used as a filler

Table 17. InfoVal weights of slope, soil depth, and landcover classes calculated from failure probability results (0.25 – 1.0) for winter DHSVM storms within each upper basin.

Classes	January 2009			January 2018			February 2041			January 2089			December 2096		
	NF	MF	SF	NF	MF	SF	NF	MF	SF	NF	MF	SF	NF	MF	SF
Slopes 0 -15°	-3.10	-3.97	-4.36	-3.32	-3.51	-4.17	-4.32	-3.71	-4.83	-4.30	-5.55	-4.33	-3.41	-3.39	-4.00
Slopes 15-30°	0.11	-0.47	-0.02	-0.54	-0.77	-0.13	-0.95	-0.69	-0.16	-0.51	-0.88	-0.16	-0.67	-0.76	-0.15
Slopes 30-45°	0.71	0.83	1.08	0.99	0.84	1.15	1.04	0.80	1.16	0.98	0.91	1.16	1.01	0.84	1.15
Slopes 45-60°	-0.36	-0.03	-0.45	0.43	0.81	-0.15	1.04	0.89	0.15	0.59	0.53	-0.03	0.68	0.74	-0.01
Slopes 60°+	-2.16	a	-3.35	-0.77	-0.73	-2.05	-0.13	-0.13	-1.91	-1.23	-0.81	-1.28	-0.93	-0.54	-1.95
Soil Depth 0.76 - 1.0 m	-1.10	-2.91	-2.59	0.23	0.02	-0.26	0.69	-0.10	0.12	0.32	-0.04	-0.14	0.31	-0.08	-0.18
Soil Depth 1.0 - 2.0 m	0.40	0.39	0.27	-0.01	-0.10	0.18	-0.73	-0.26	0.12	-0.08	-0.09	0.16	-0.07	-0.07	0.17
Soil Depth 2.0 - 3.5 m	-0.86	-0.39	-3.02	-1.01	0.72	-3.73	-0.17	1.42	-3.51	-1.00	0.80	-3.91	-1.15	0.81	-3.84
Large Conifer	-1.18	-0.80	-1.14	-1.35	-1.53	-1.26	-1.36	-1.69	-1.15	-1.36	-1.52	-1.27	-1.34	-1.51	-1.27
Large Mixed Stand	0.82	1.12	0.35	0.61	0.70	0.27	0.68	0.62	0.29	0.67	0.67	0.26	0.61	0.69	0.26
Developed	-2.26	0.50	-1.92	-2.26	0.35	-1.60	-2.31	-1.50	-1.17	-1.87	0.22	-1.49	-2.08	0.54	-1.72
Broadleaf	0.65	1.02	0.72	0.30	0.69	0.40	0.13	0.92	0.60	0.27	0.68	0.47	0.34	0.73	0.43
Ice	a	a	a	a	-5.78	a	a	-5.06	a	a	a	a	a	-5.79	a
Shrubland	1.18	1.00	1.03	1.34	1.47	1.12	1.39	1.38	1.03	1.37	1.47	1.11	1.32	1.45	1.12
Sparse/Open/Agriculture	-1.11	-0.40	-2.59	-2.11	-0.15	-2.50	-2.27	-1.99	-2.31	-1.69	-0.72	-2.40	-2.27	-0.08	-2.48
Rock	-3.18	-2.11	-4.10	-1.92	-2.04	-2.39	-1.44	-2.03	-1.87	-1.90	-2.22	-2.20	-1.79	-2.06	-2.20
Water	a	-2.73	-3.16	-4.10	-4.35	-3.07	a	-3.63	-3.10	a	-4.31	-3.98	-3.85	-4.36	-4.06
Wetland	0.28	-0.27	-2.52	0.68	1.20	-0.90	0.22	1.78	-0.72	0.37	1.30	-0.91	0.76	1.31	-0.86

[a] represents an arbitrary weight equivalent to -3.00 used as a filler

Table 18. InfoVal weights of factors calculated from failure probability results (0.25 – 1.0) for fall DHSVM storms within each upper basin.

Classes	October 2003			October 2089		
	NF	MF	SF	NF	MF	SF
Slopes 0 -15°	-4.22	-5.45	-5.00	-3.86	-3.60	-4.31
Slopes 15-30°	-0.48	-0.78	-0.03	-0.80	-0.73	-0.14
Slopes 30-45°	0.95	0.88	1.09	1.01	0.83	1.15
Slopes 45-60°	0.74	0.55	-0.29	0.98	0.73	-0.06
Slopes 60°+	-1.39	-0.71	-3.37	-0.71	-0.54	-1.30
Saturation % 0.1 - 0.3	-4.24	a	a	-6.14	a	a
Saturation % 0.3-0.5	-4.34	-4.49	-6.36	-3.71	-3.73	-4.53
Saturation % 0.5-0.7	-3.09	-3.55	-3.58	-2.27	-2.35	-3.04
Saturation % 0.7-1.0	0.20	0.25	0.19	0.13	0.19	0.17
1 (Sand, SW)	-	-	a	-	-	a
2 (Sand, Qgoe)	-1.87	-1.73	-0.72	-3.83	-3.40	-0.79
3 (Loamy Sand, SM-SG)	a	a	-	a	a	-
4 (Loamy Sand, GP)	1.12	1.54	2.17	1.47	1.04	2.53
5 (Loamy Sand, GM)	1.77	1.44	1.38	1.82	1.46	1.38
6 (Loamy Sand, Qa)	-0.18	0.16	-1.45	-0.67	-0.03	-1.74
7 (Loamy Sand, Qls)	-1.99	-1.21	-2.16	-1.98	-1.47	-2.15
8 (Sandy Loam, Qaf)	-3.29	a	a	-3.89	a	a
9 (Sandy Loam, SM)	-3.10	-3.40	-2.84	-3.60	-2.99	-2.77
10 (Sandy Loam, ML-MG)	-4.62	-7.21	-3.57	-5.16	-5.64	-3.72
11 (Silty Loam, ML-MS)	-5.62	a	a	-4.70	a	a
12 (Silt, ML)	-2.10	-2.61	-2.84	-2.76	-2.68	-3.18
13 (Silt, Qgt)	-3.67	-4.66	-2.77	-3.64	-4.59	-2.84
14 (Sandy Clay Loam, SM-SC)	a	a	a	a	a	a
15 (Clay Loam, CL)	a	-	a	a	-	a
16 (Sandy Clay, Qad)	-3.08	-3.34	-3.40	-4.08	-3.75	-3.57
17 (Silty Clay, CL-ML)	a	a	-	a	a	-
18 (Organic, OH)	-5.51	a	a	-3.41	a	a
19 (Organic, OL)	-3.18	-3.03	-3.22	-3.08	-2.61	-2.88
22 (Muck, PT)	-4.40	-3.71	-2.91	-6.10	-3.53	-2.64
23 (Talus, Qta)	1.49	0.36	0.50	1.47	0.74	0.50
24 (Loamy Sand, Qm)	2.34	2.52	a	2.44	2.48	a
Soil Depth 0.76 - 1.0 m	0.36	-0.27	-0.46	0.55	-0.10	-0.17
Soil Depth 1.0 - 2.0 m	-0.12	-0.01	0.19	-0.32	-0.07	0.17
Soil Depth 2.0 - 3.5 m	-0.93	0.90	-3.13	-1.04	0.84	-3.90
Large Conifer	-1.40	-1.50	-1.27	-1.48	-1.51	-1.28
Large Mixed Stand	0.68	0.67	0.26	0.61	0.67	0.25
Developed	-2.82	0.33	-1.53	-2.13	0.37	-2.01
Broadleaf	0.33	0.67	0.38	0.28	0.71	0.43
Ice	-5.05	-5.53	a	-4.44	a	a
Shrubland	1.35	1.45	1.13	1.38	1.45	1.12
Sparse/Open/Agriculture	-1.99	-0.67	-2.74	-2.28	-0.29	-2.56
Rock	-1.61	-2.03	-2.23	-1.46	-1.90	-2.35
Water	-4.07	-3.41	-3.87	-3.88	-4.33	-3.94
Wetland	0.45	1.38	-1.05	0.63	1.35	-0.87

[a] represents an arbitrary weight equivalent to -3.00 used as a filler

Table 19. Area of very high susceptibility (km^2) derived from LSI values in InfoVal method for historical and projected storm events within each upper basin.

	January 2009	January 2089	December 2096	October 2003	October 2089
North Fork	89.5	67.9	80.1	64.7	79.6
Middle Fork	17.9	30.8	13.6	27.7	13.2
South Fork	64.1	73.4	72.0	71.2	70.4

9.0 Figures

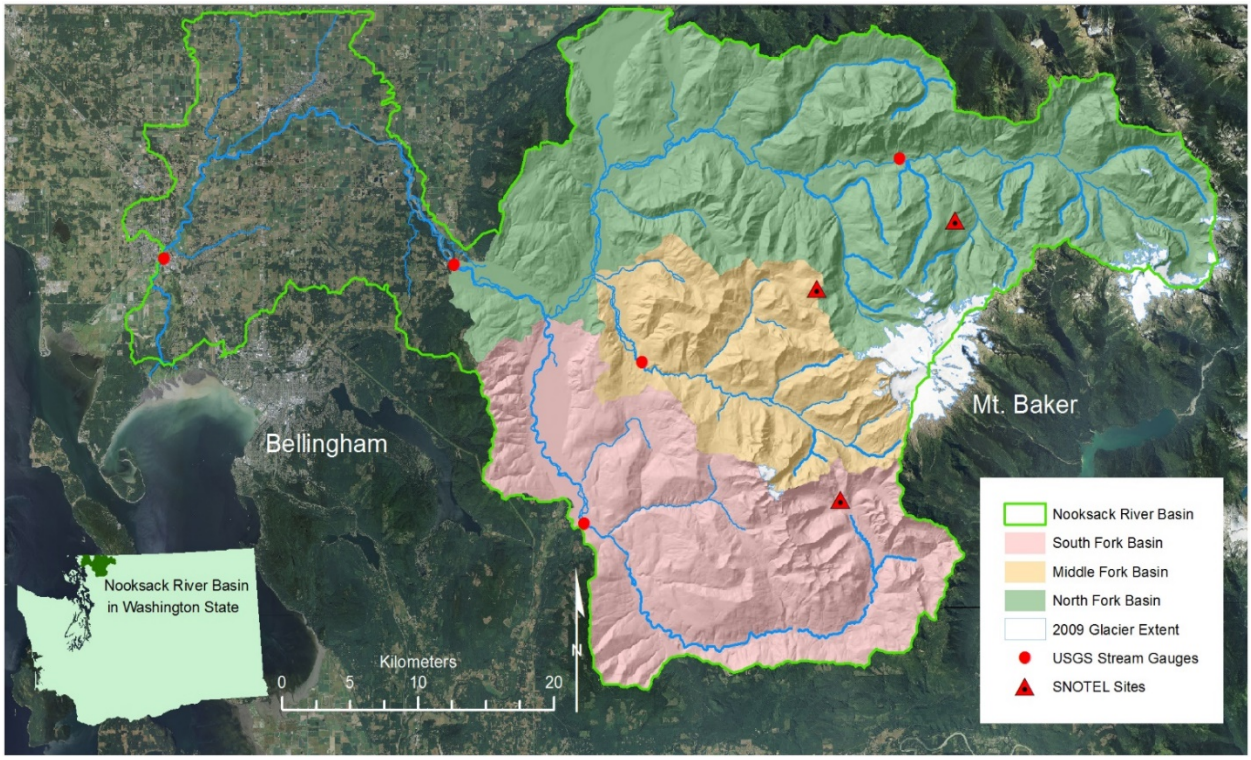

Figure 1. Location of the Nooksack River basin, northwest Washington State, with the North, Middle and South Fork basins.

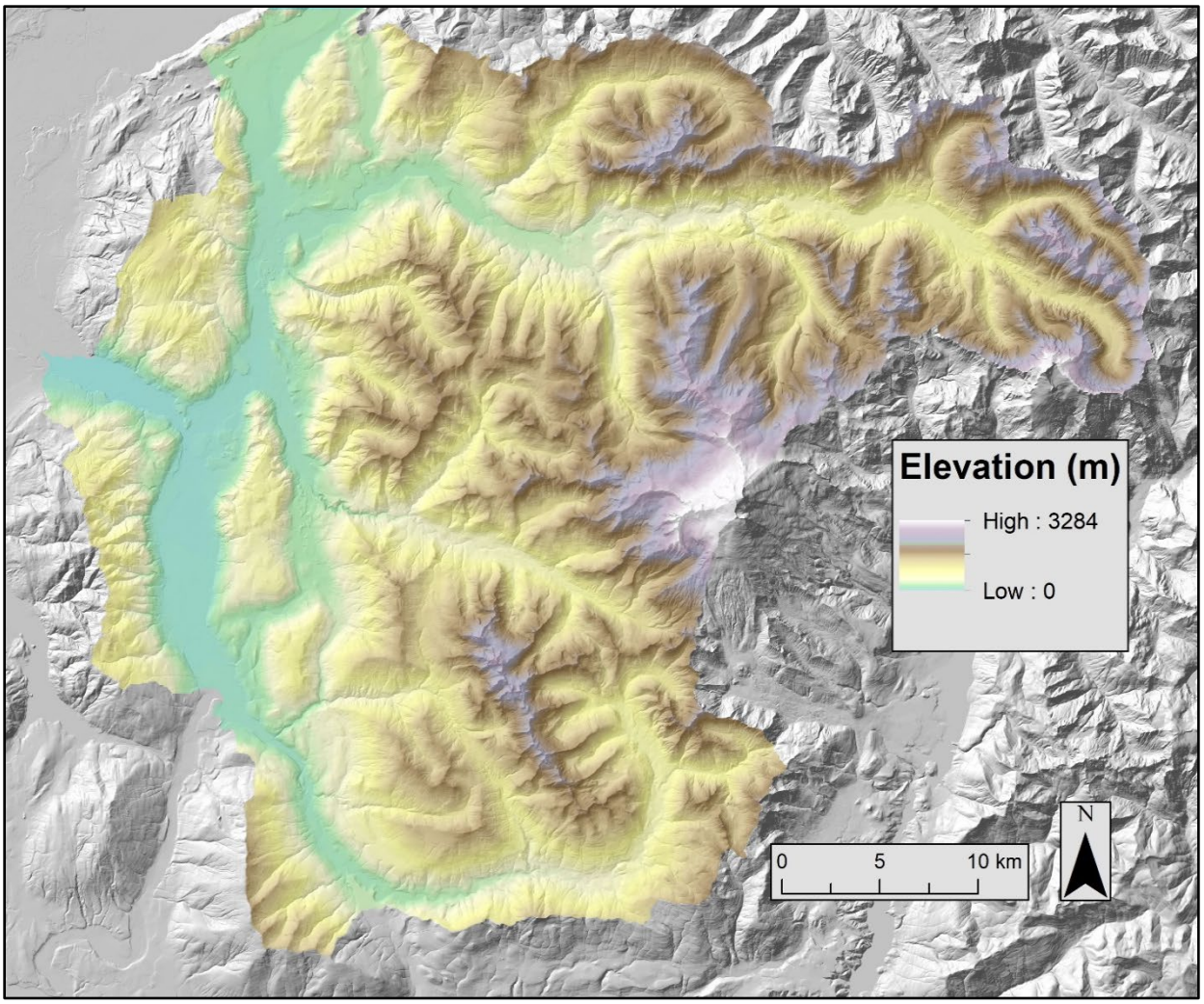

Figure 2. Elevation in the upper Nooksack River basin, represented by a filled 1-m resolution DEM.

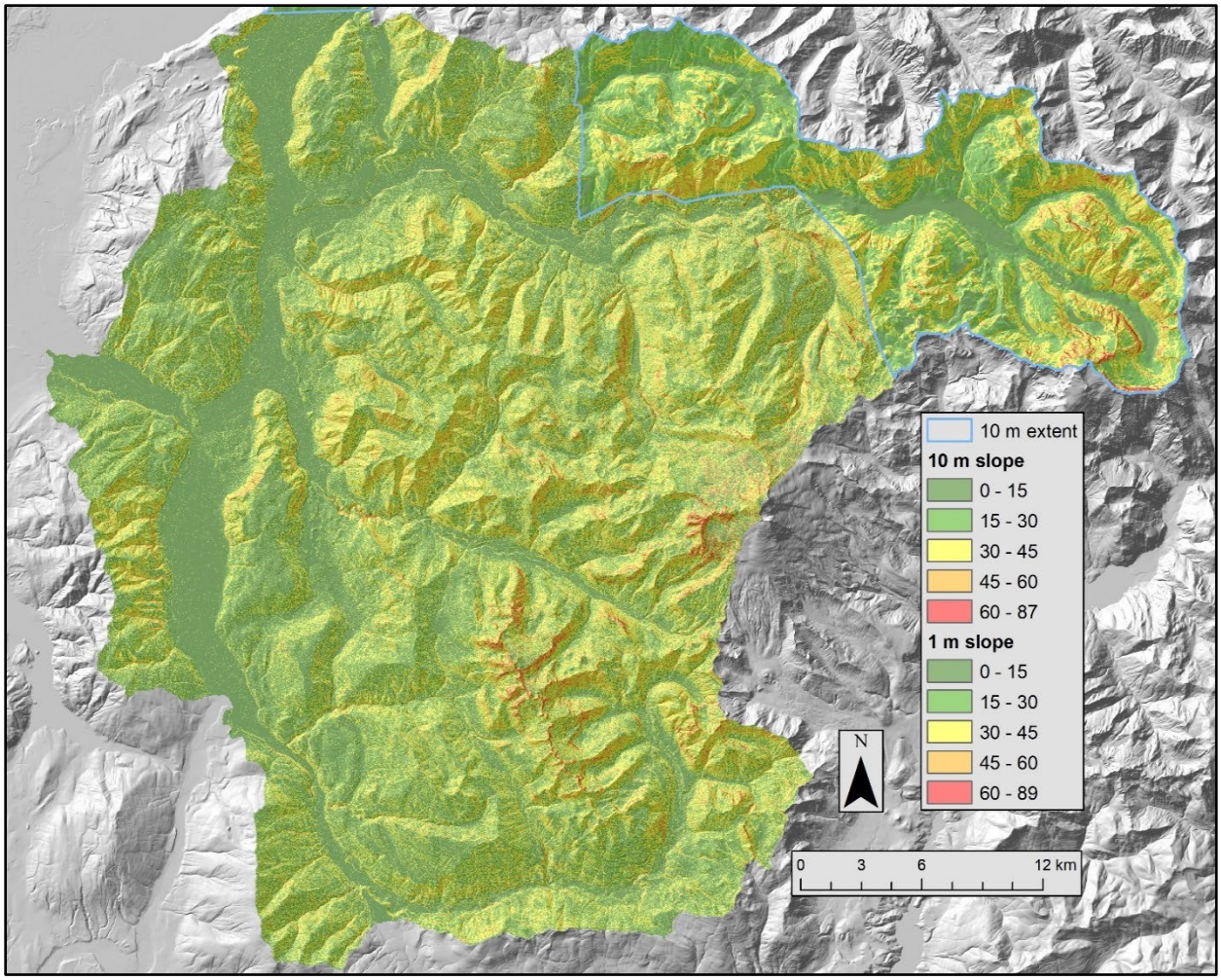

Figure 3. LiDAR derived slope map of the upper Nooksack Basin in degrees. The majority of the study area is covered by 1 m LiDAR, while the remaining NE section is covered by 10 m LiDAR.

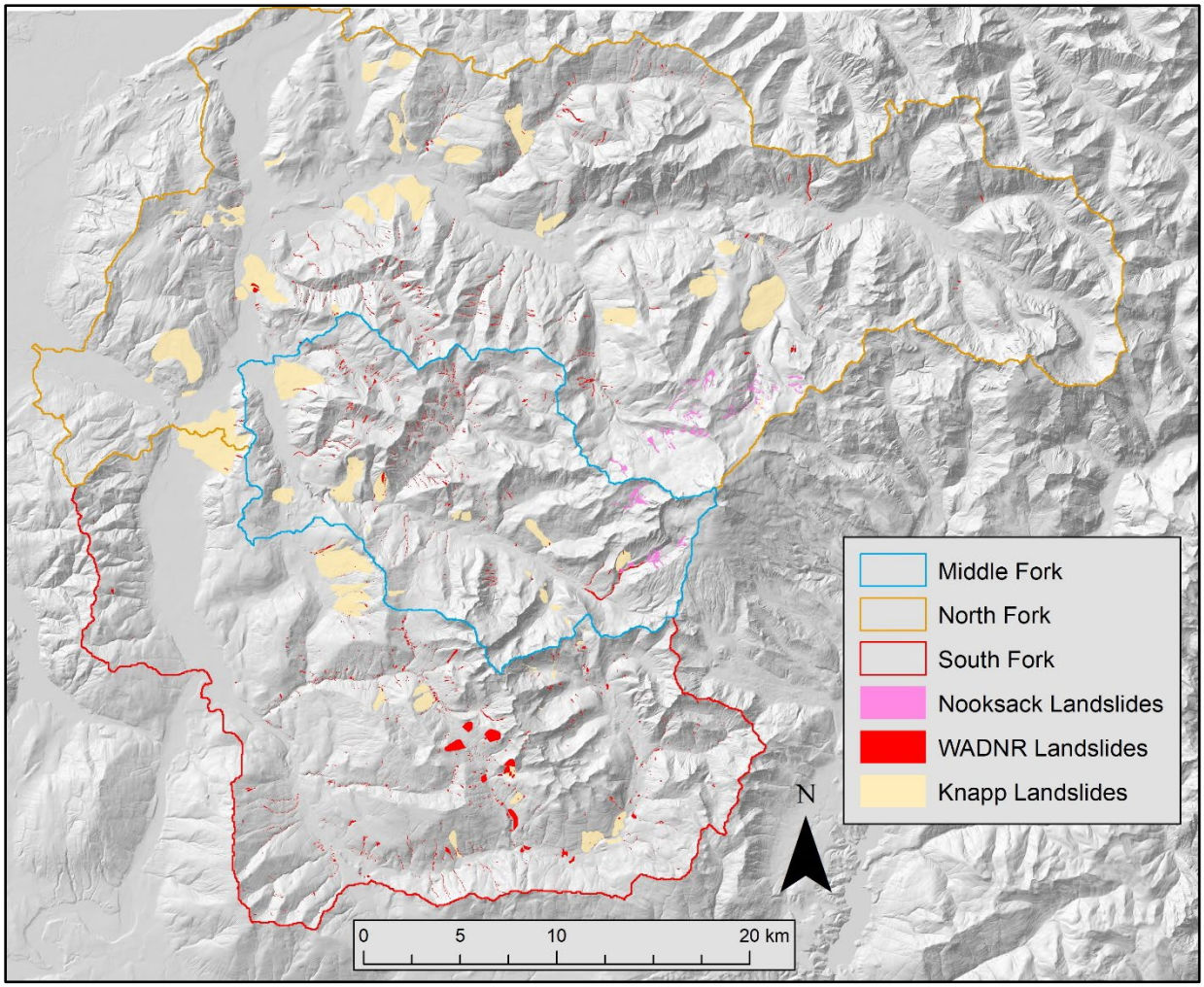

Figure 4. Landslide deposits digitized by WADNR, Nooksack Indian Tribe (Nielsen and Grah, 2015), and Knapp (2017, WADNR SLIP mapping protocol) within the upper Nooksack basin.

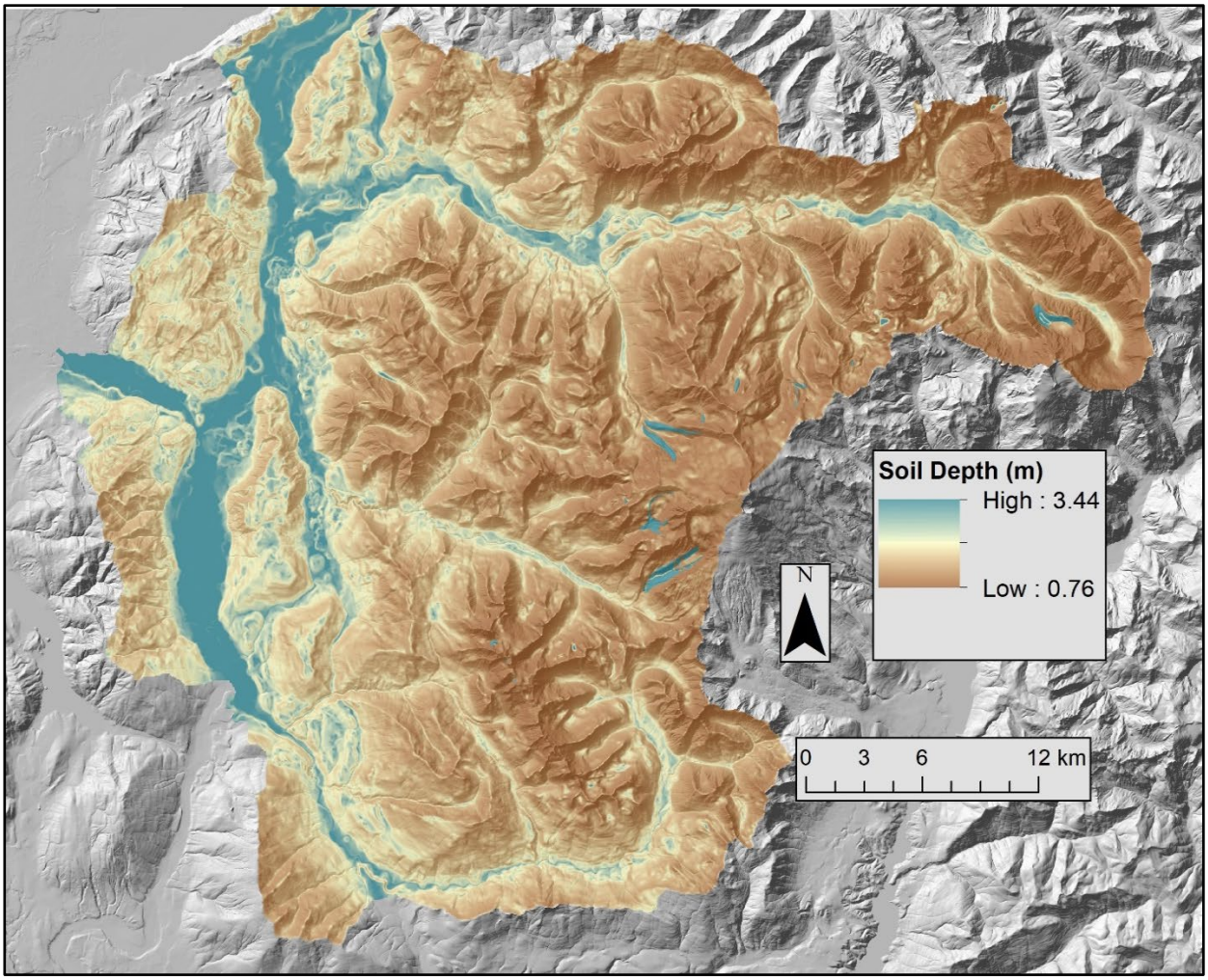

Figure 5. Soil depth raster (meters) derived from a DEM using a Python script for the upper Nooksack Basin. Mapped moraine deposits (Qm) with an assigned constant soil depth of 3 m are shown in the upper elevations of each sub-basin.

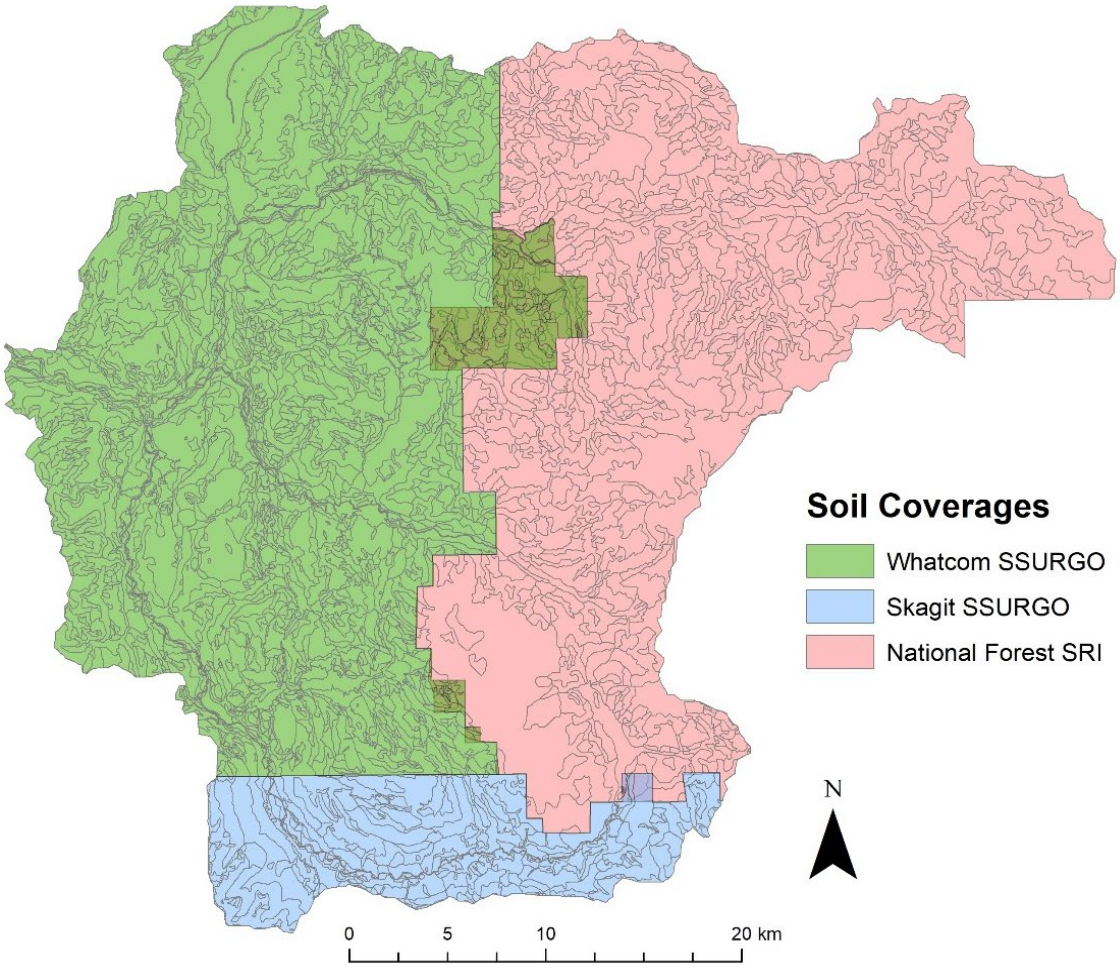

Figure 6. Soil coverage shapefiles used in the upper Nooksack basin: Whatcom County SSURGO (green), Skagit County SSURGO (blue), and Mt. Baker-Snoqualmie National Forest SRI (red). In locations where coverages overlapped, SSURGO coverages were used because of their more detailed attributes.

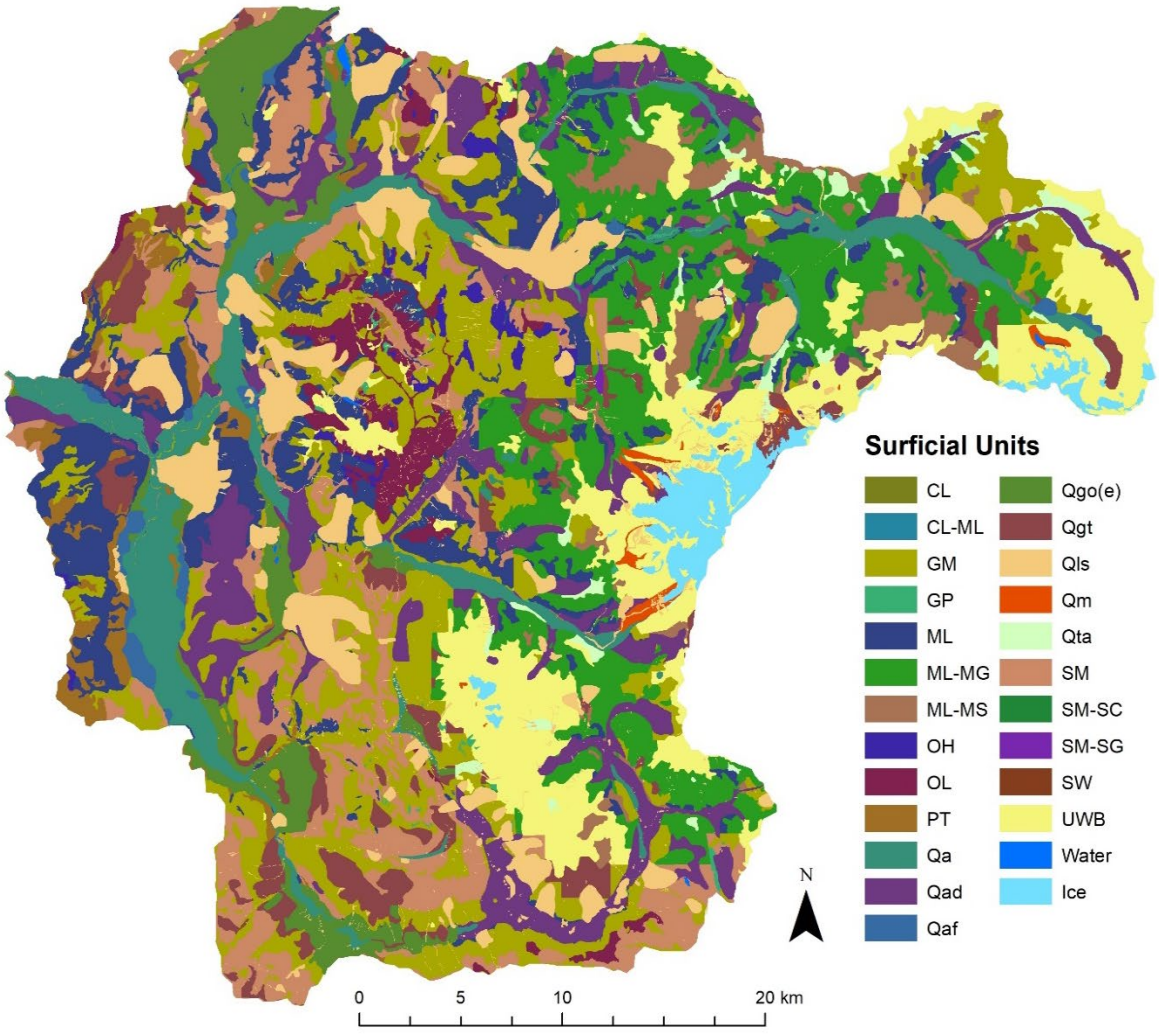

Figure 7. Surficial unit distribution in the upper Nooksack basin with polygons representing USCS classifications (e.g., CL) and geologic units (e.g., Qa).

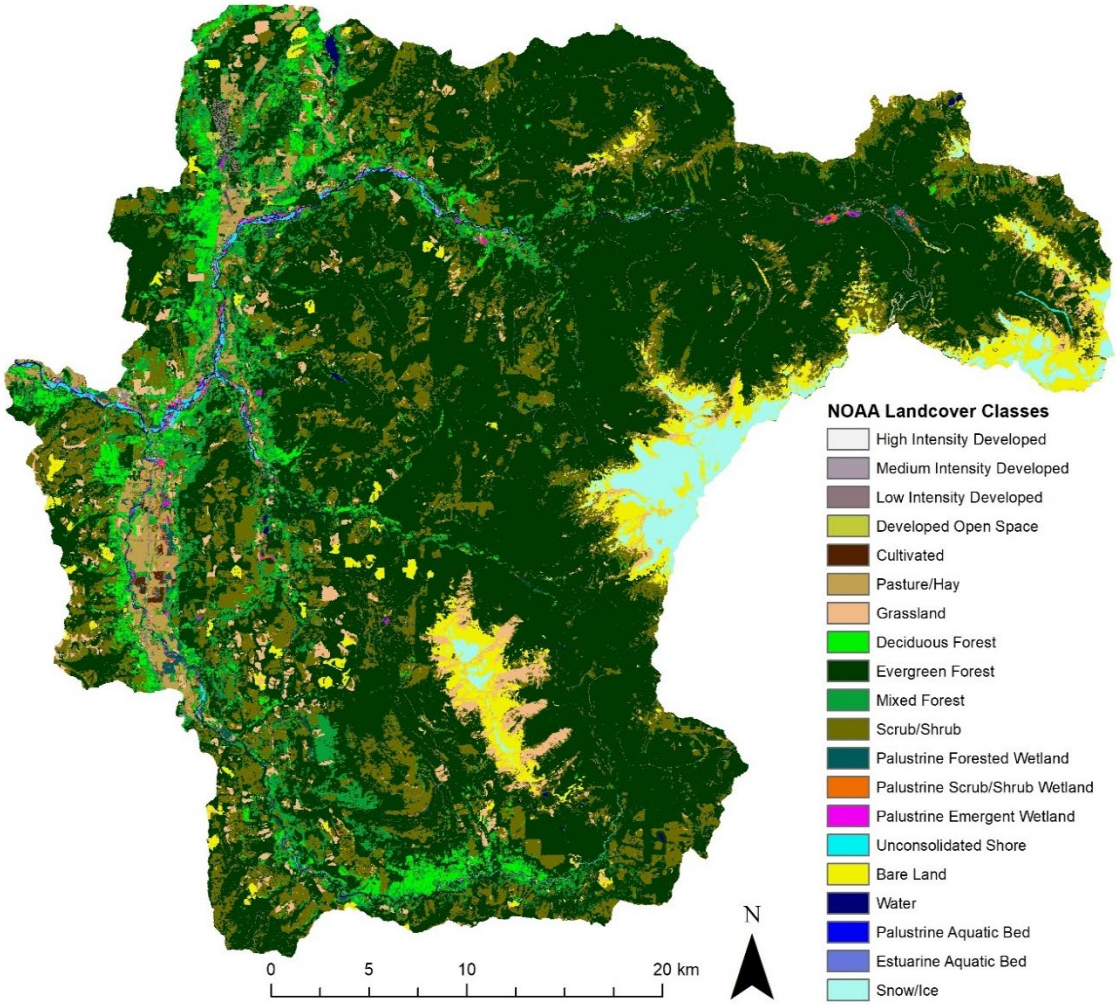

Figure 8. Original 30 m resolution 2011 NOAA landcover classification raster.

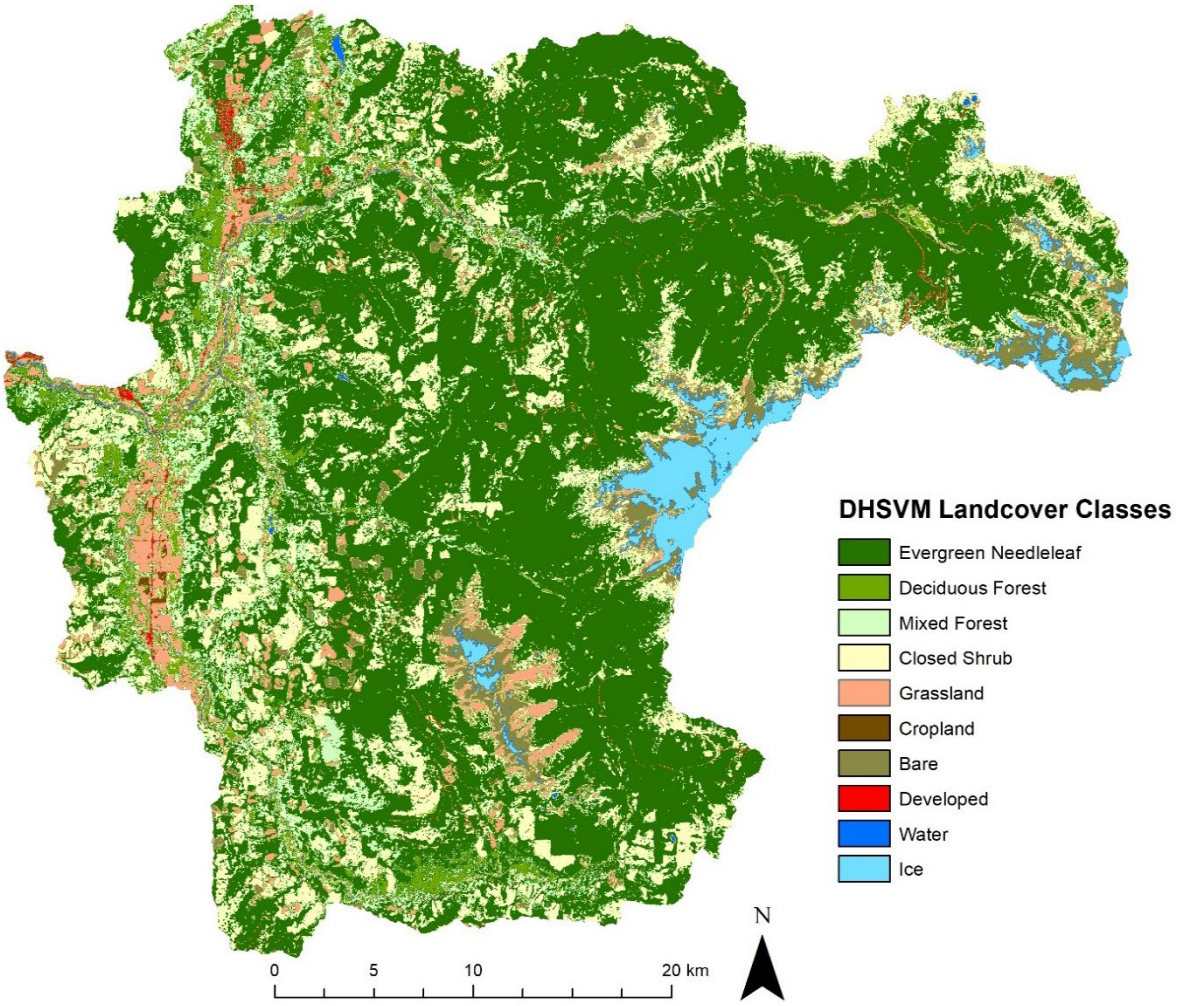

Figure 9. Resampled 10 m DHSVM land cover classification raster based on the 2011 NOAA landcover grid.

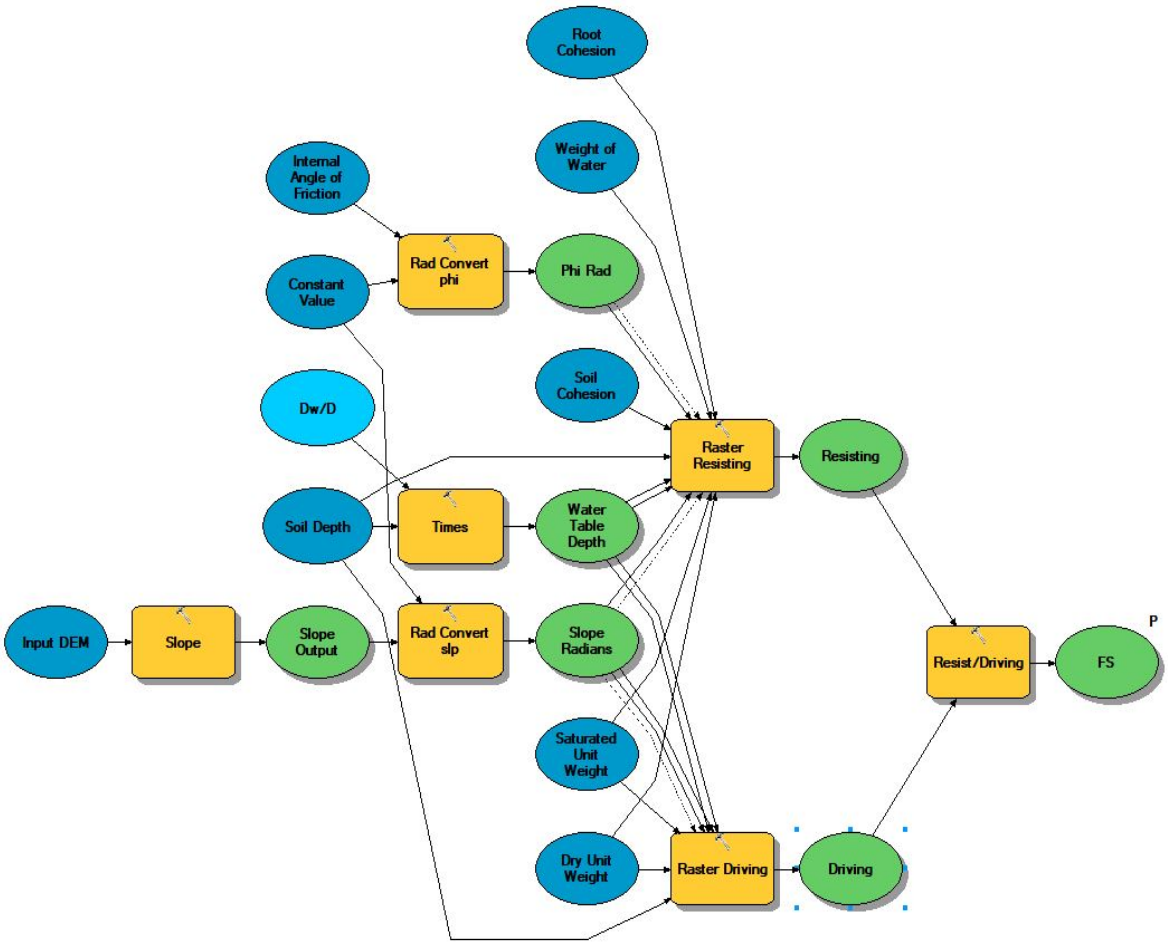

Figure 10. ArcGIS ModelBuilder visual representation of the modified Hammond et al. (1992) static infinite-slope model. Dark blue circles represent input rasters, light blue circles represent constant input values, yellow rectangles represent geoprocessing tools, and green circles represent output raster.

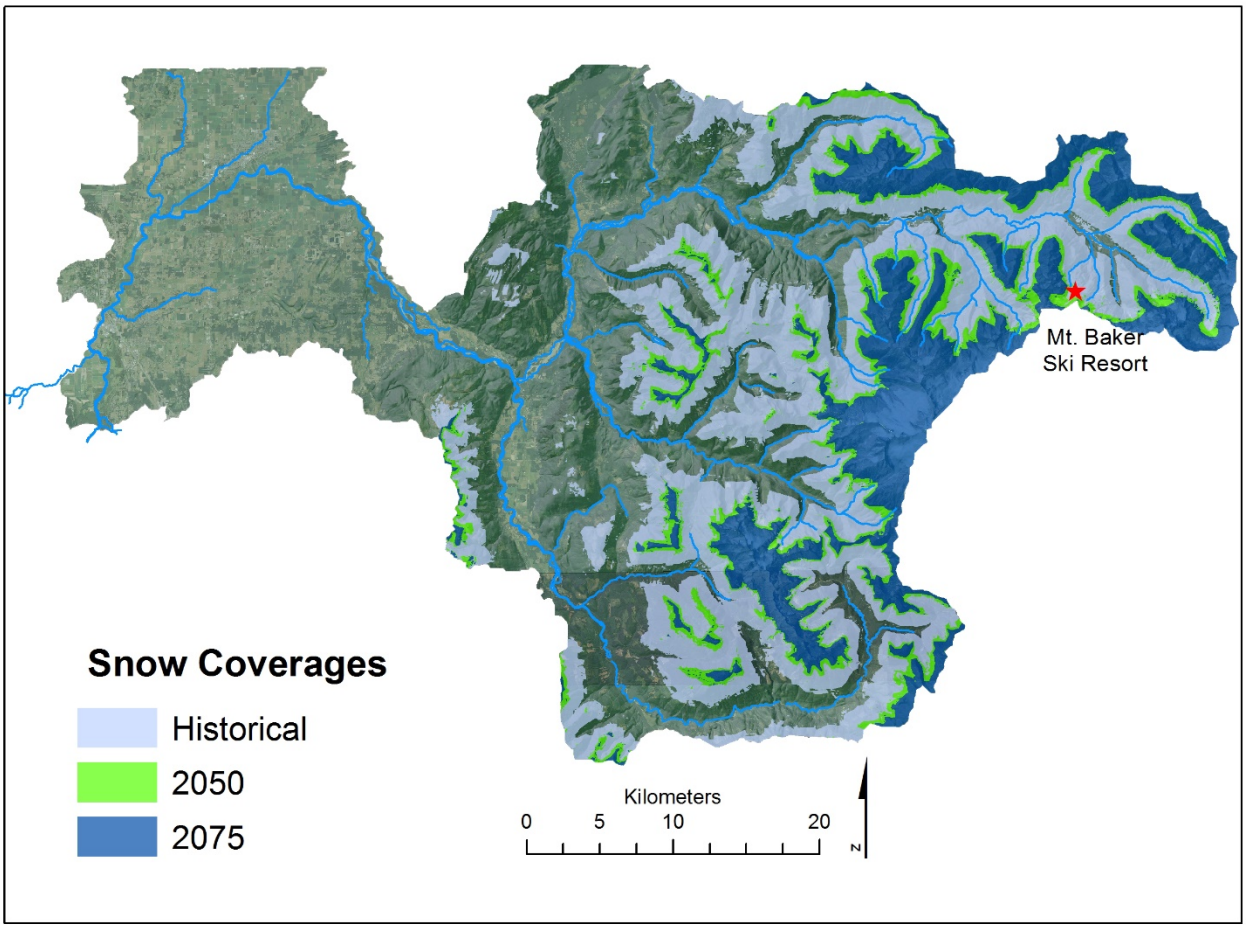

Figure 11. Modeled 30-year median snow coverages in January, centered on 1995 (historical), 2050, and 2075 for RCP 8.5 scenarios using the CSIRO-Mk3-6-0 GCM (Mitchell et al., 2016).

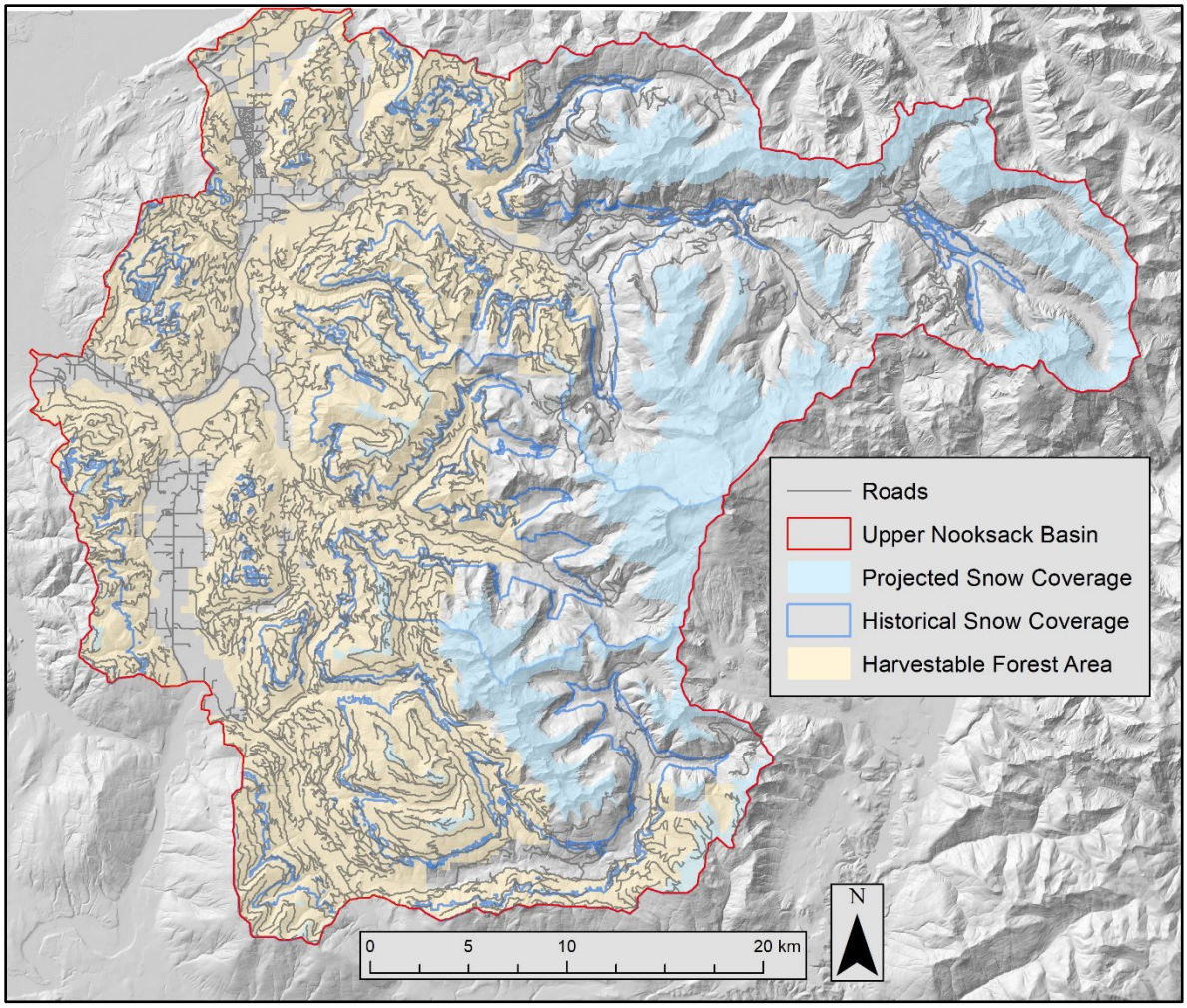

Figure 12. Roads and harvestable forest areas within the upper Nooksack basin with median historical (1995) and projected (2075) snow coverages.

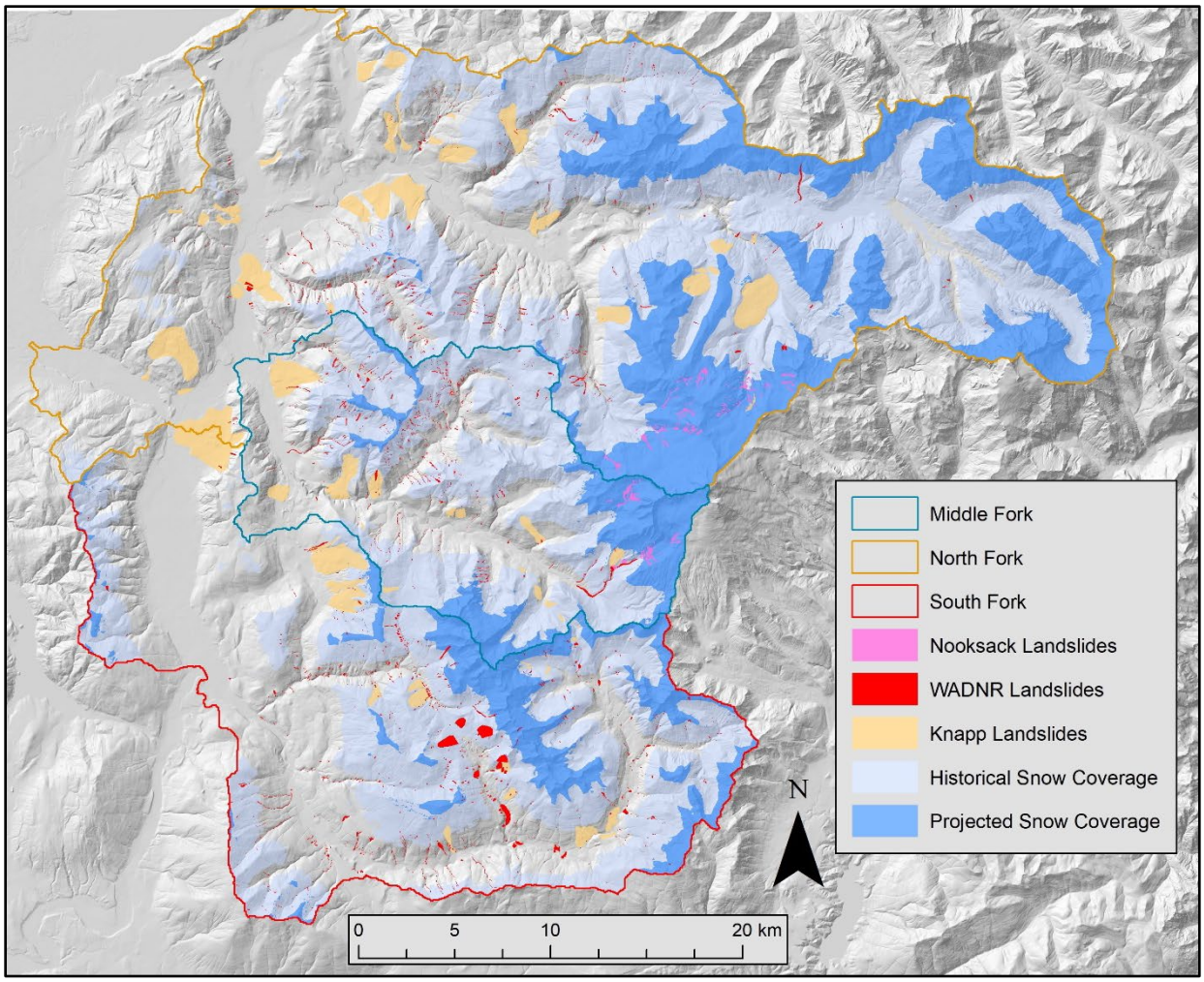

Figure 13. Landslide deposits digitized by WADNR, Nooksack Indian Tribe (Nielsen and Grah, 2015), and Knapp (2017, WADNR SLIP mapping protocol) with median historical (1995) and projected (2075) snow coverages within the upper Nooksack basin.

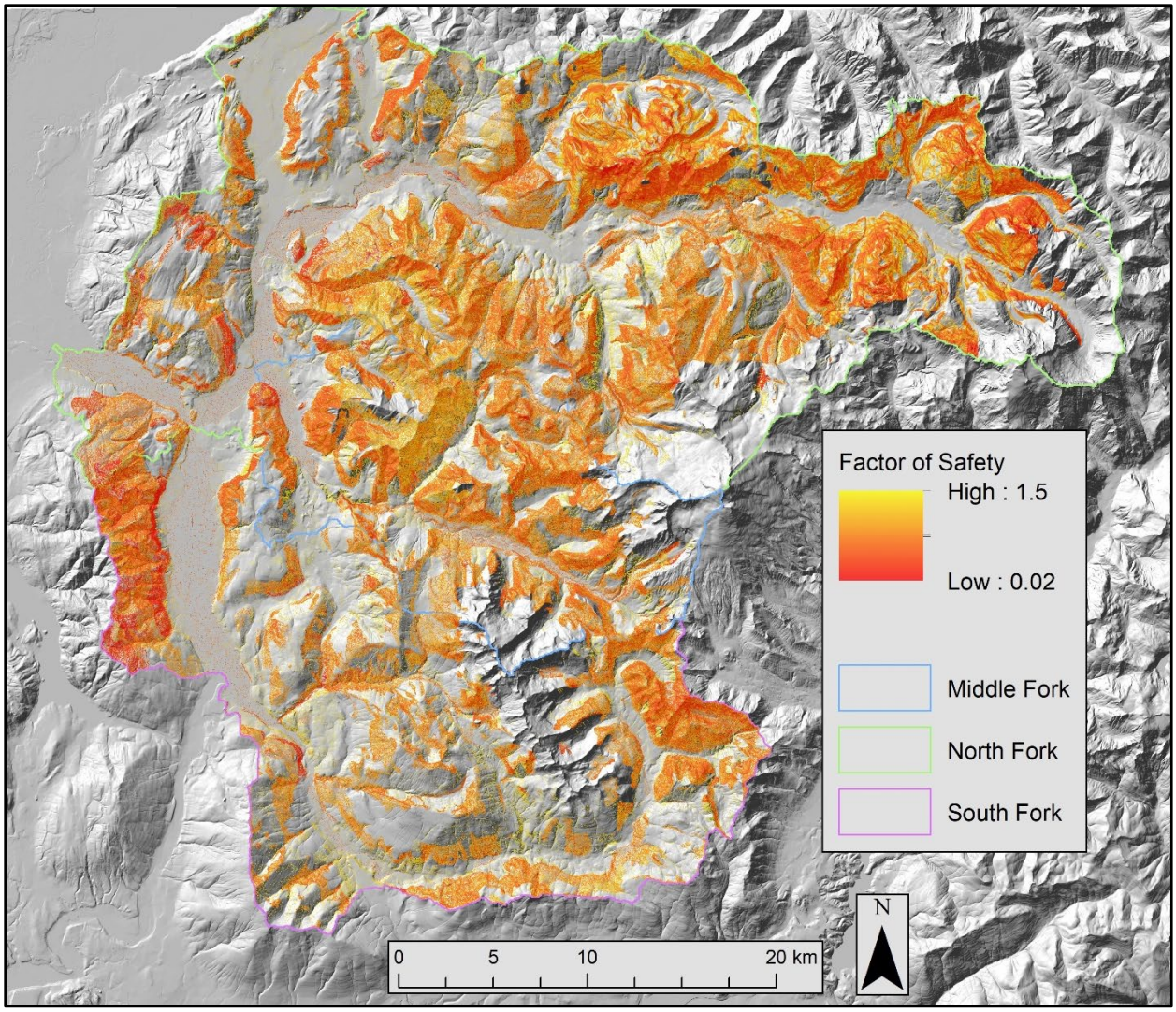

Figure 14. FS results from static modeling associated with a historical scenario using 1-m resolution, $D_w/D = 0.95$, and a soil depth profile of 0.76 – 3.5 m.

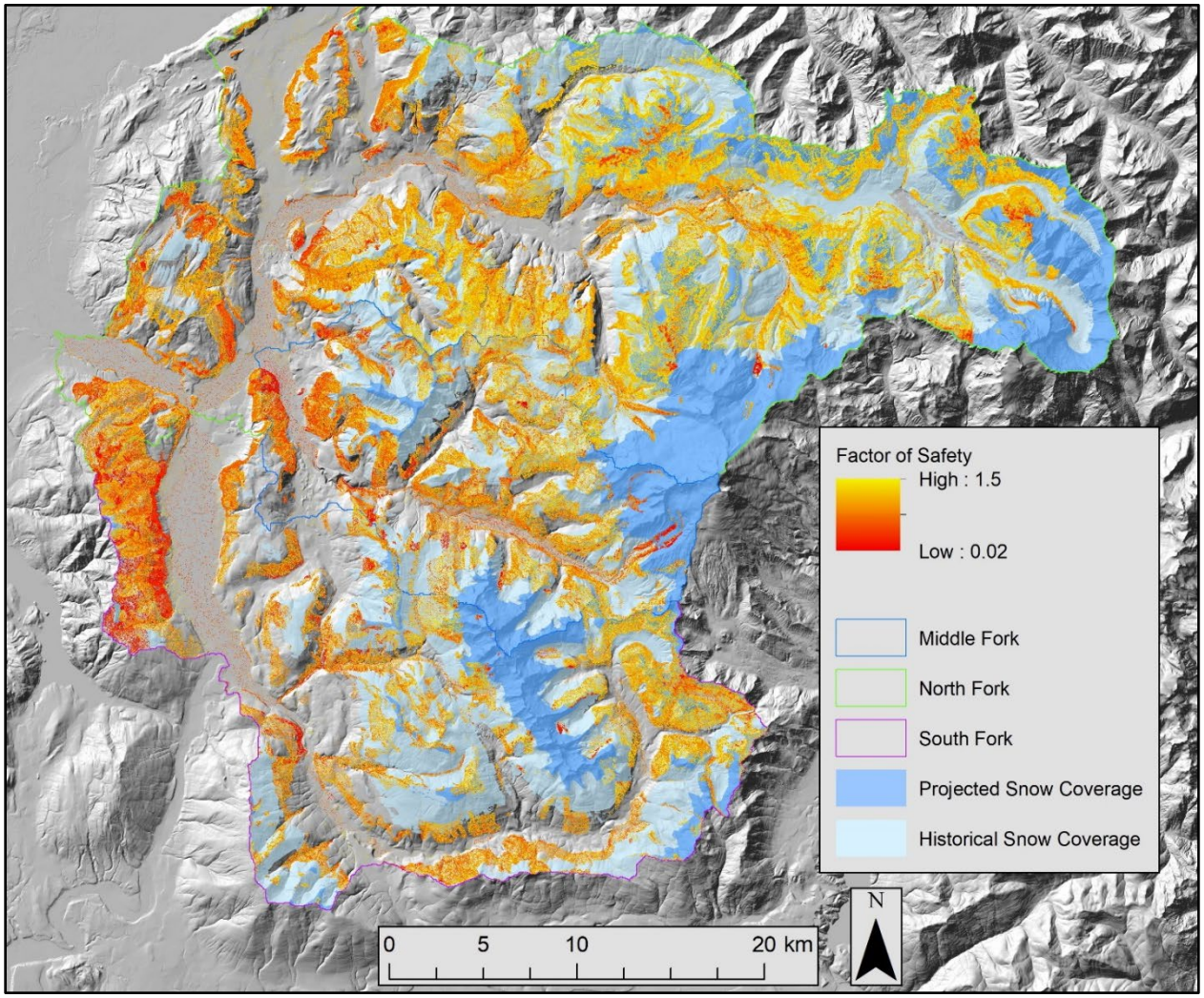

Figure 15. FS results from static modeling associated with a projected moraine deposits using 1-m resolution, $D_w/D = 0.95$ and a soil depth profile of 0.76 – 3.5 m, with historical (1995) and projected (2075) median snow coverages displayed within the upper Nooksack basin.

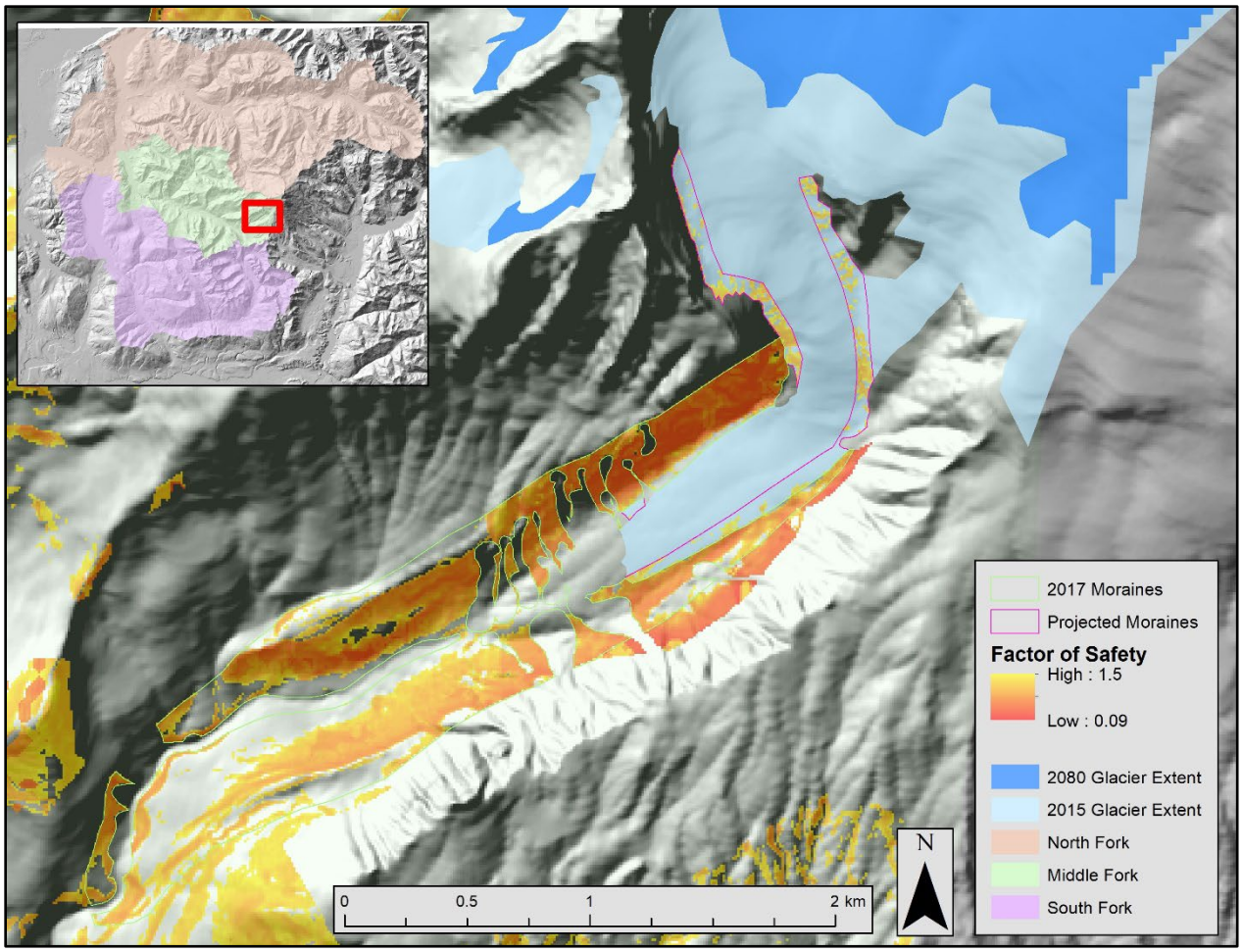

Figure 16. Static results (FS < 1.5) showing both historical and projected glacier extents and moraine deposits at a 10-m resolution.

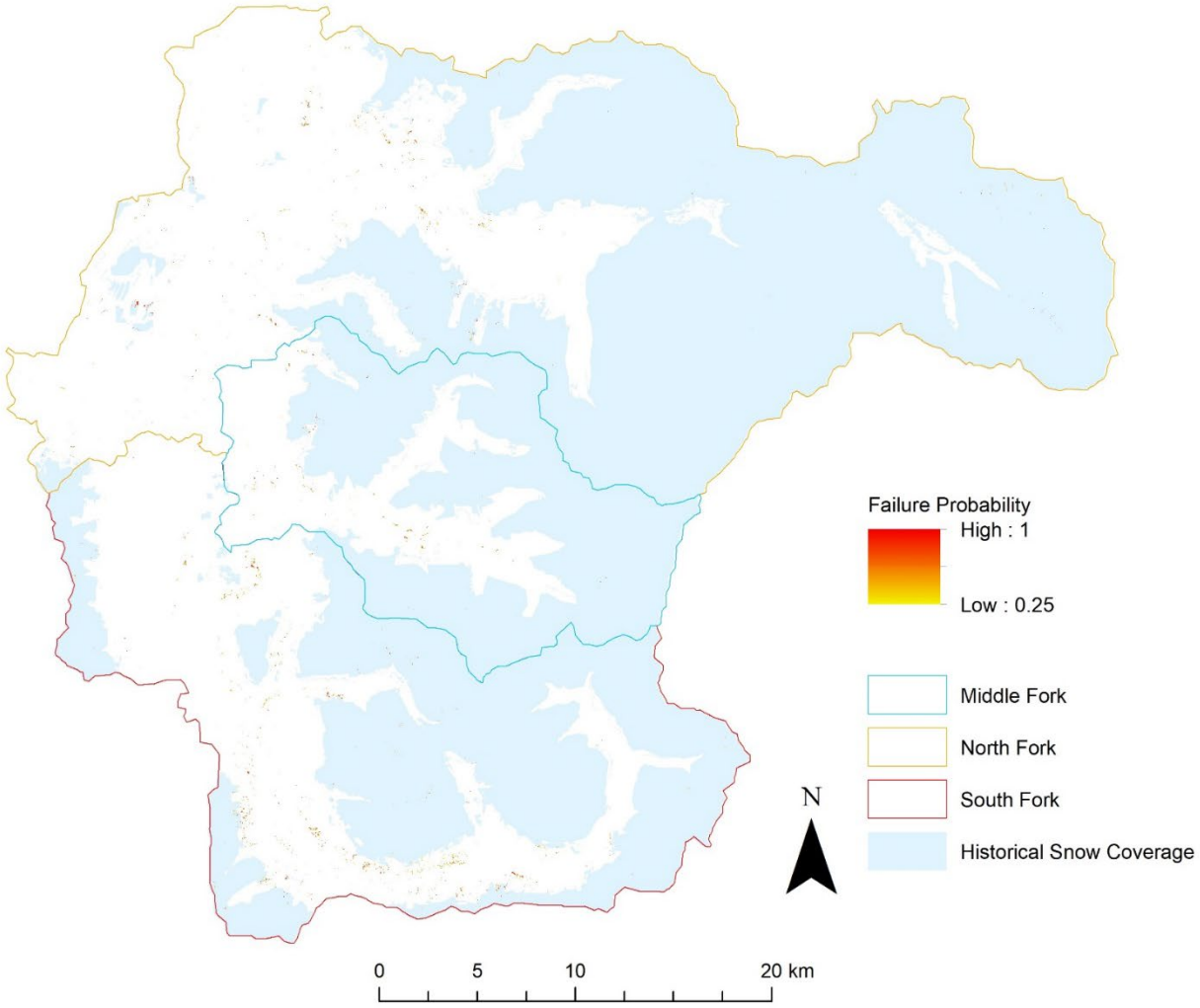

Figure 17. Failure Probability areas (0.25 – 1.0) associated with the January 2009 storm event, with historical median snow coverage (1995) displayed within the upper Nooksack basin.

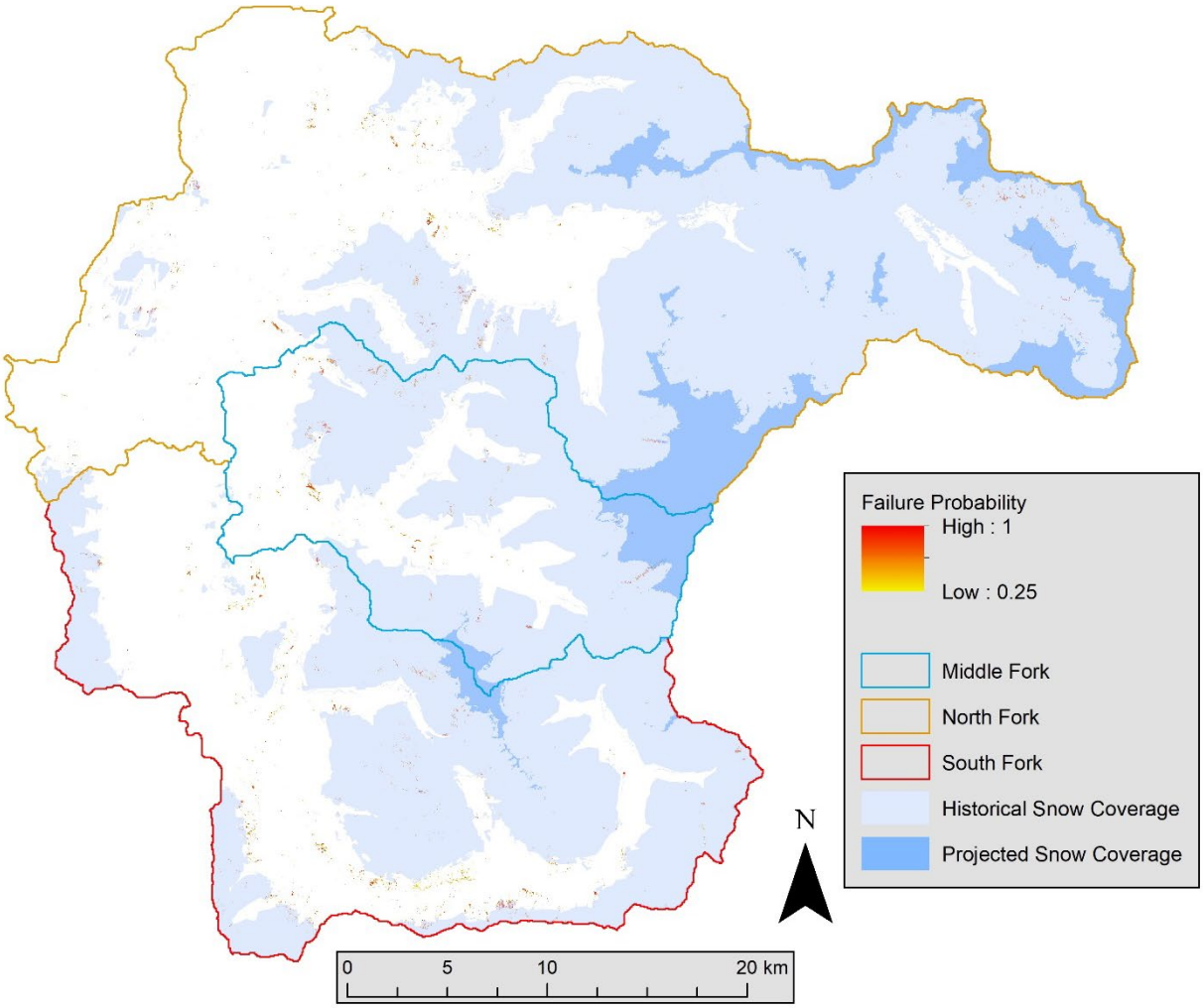

Figure 18. Failure Probability (0.25 – 1.0) associated with the January 2089 storm event, with historical (1995) median snow and the projected 2089 snow coverage displayed within the upper Nooksack basin.

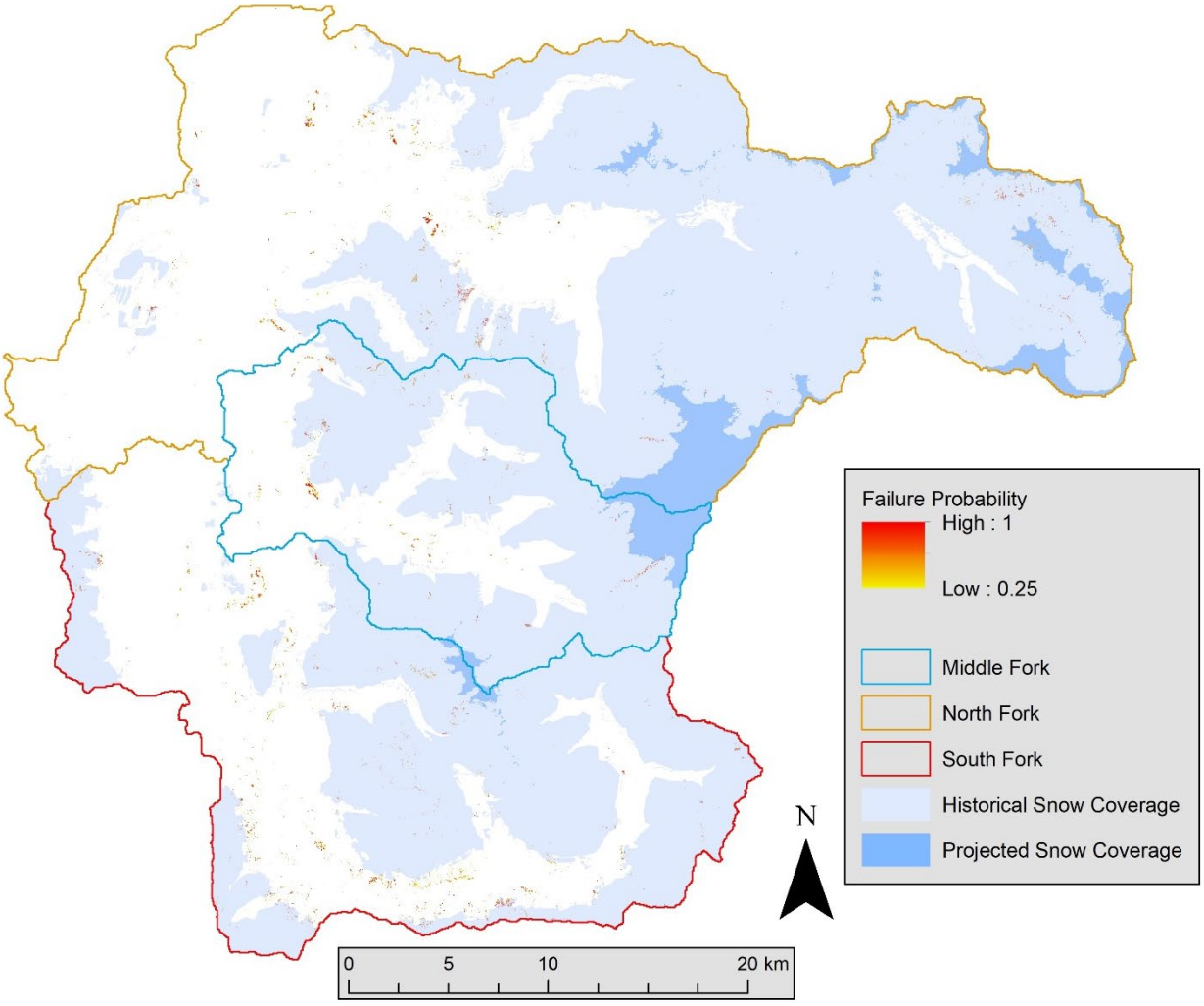

Figure 19. Failure Probability (0.25 – 1.0) associated with the December 2096 storm event, with historical (1995) median snow and the projected 2096 snow coverage displayed within the upper Nooksack basin.

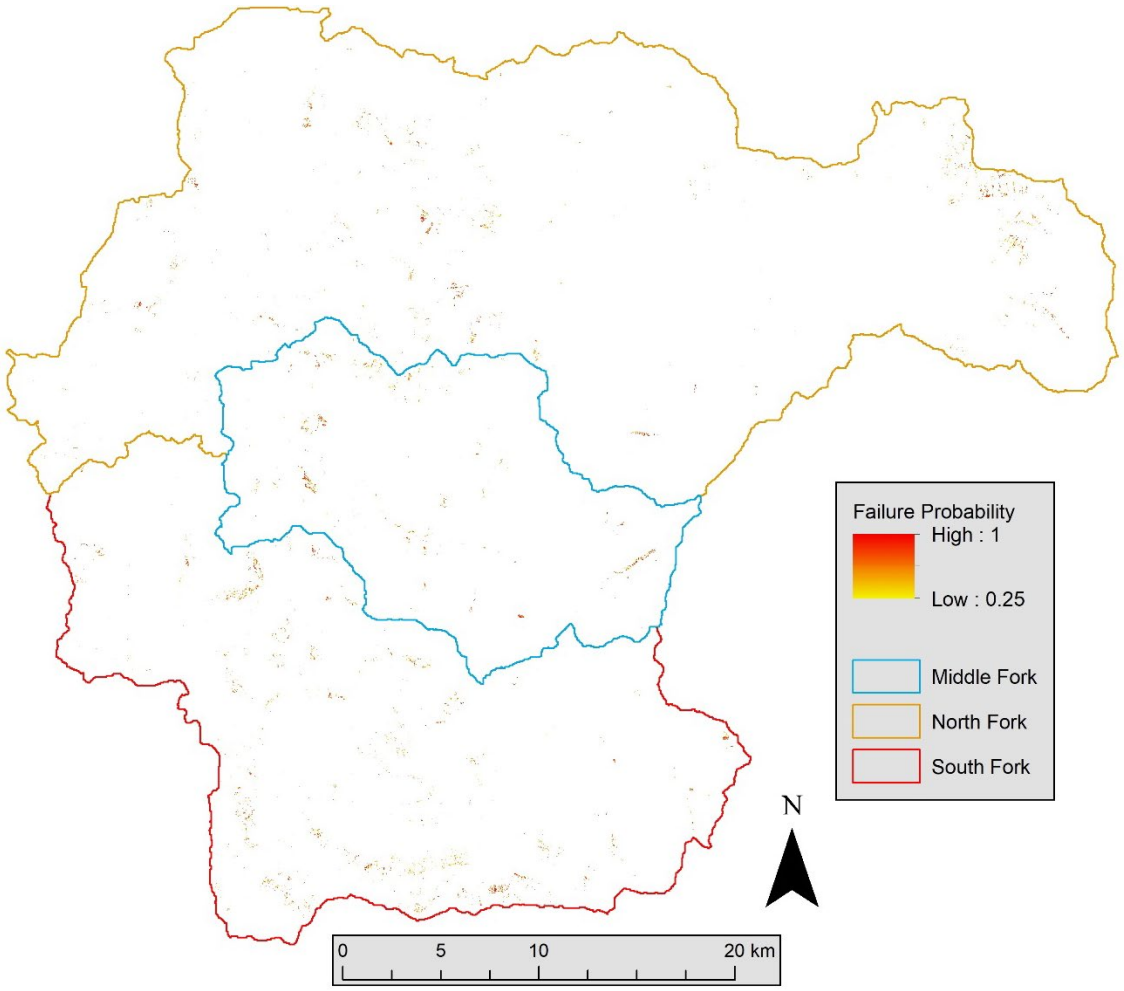

Figure 20. Failure Probability (0.25 – 1.0) associated with the October 2003 storm event.

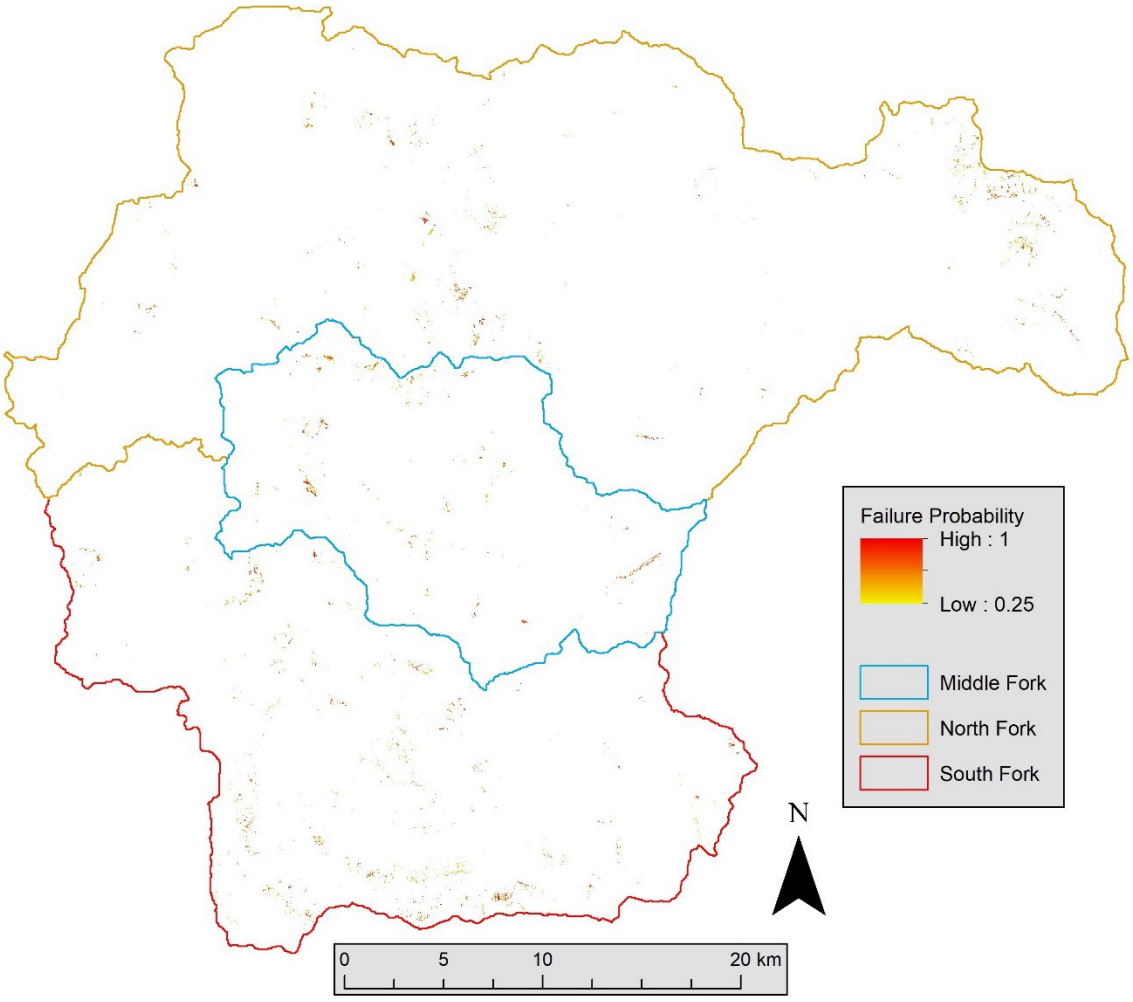

Figure 21. Failure Probability (0.25 – 1.0) associated with the October 2089 storm event.

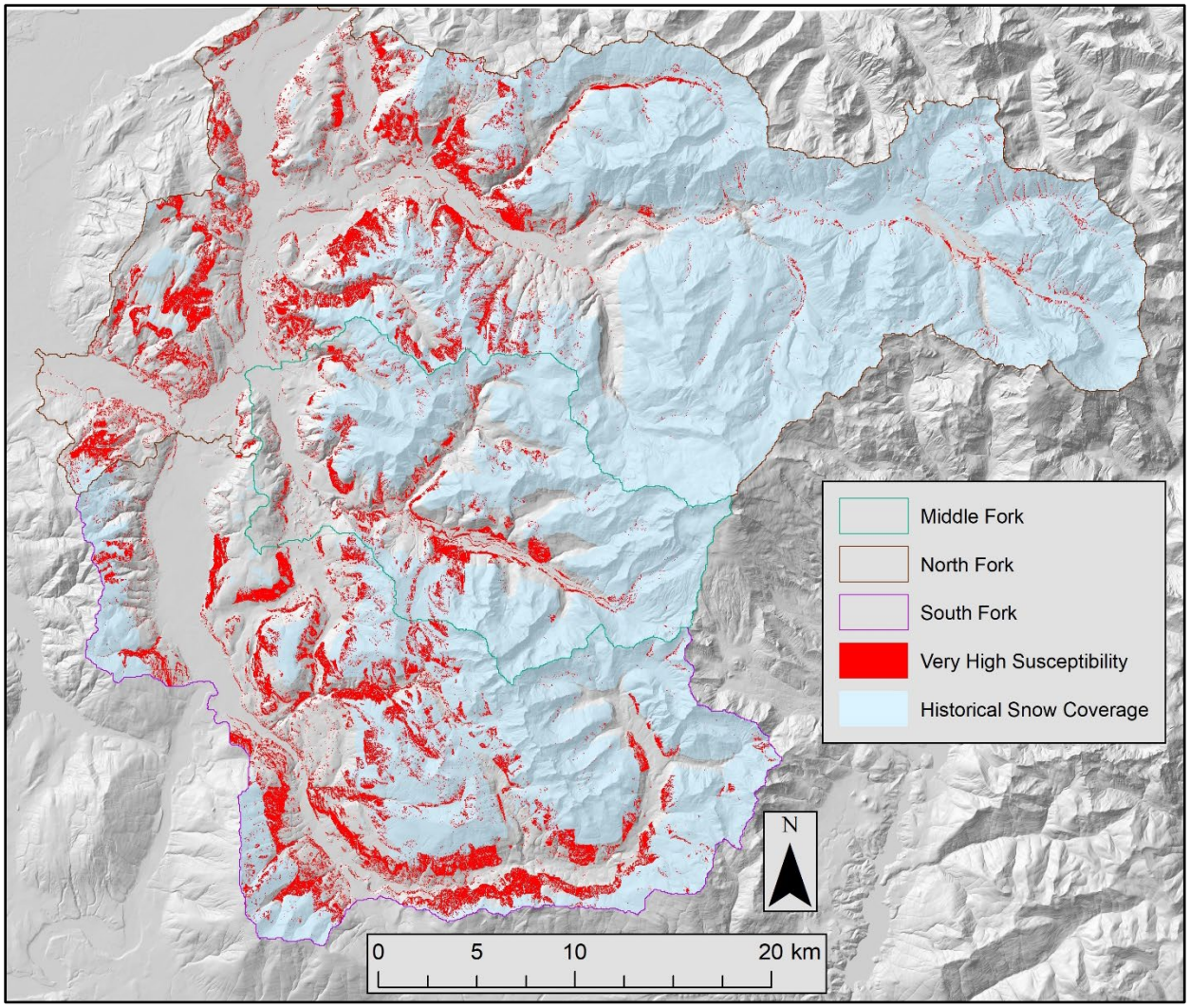

Figure 22. Very high susceptibility associated with the January 2009 storm event, with historical median snow coverage (1995) displayed within the upper Nooksack basin.

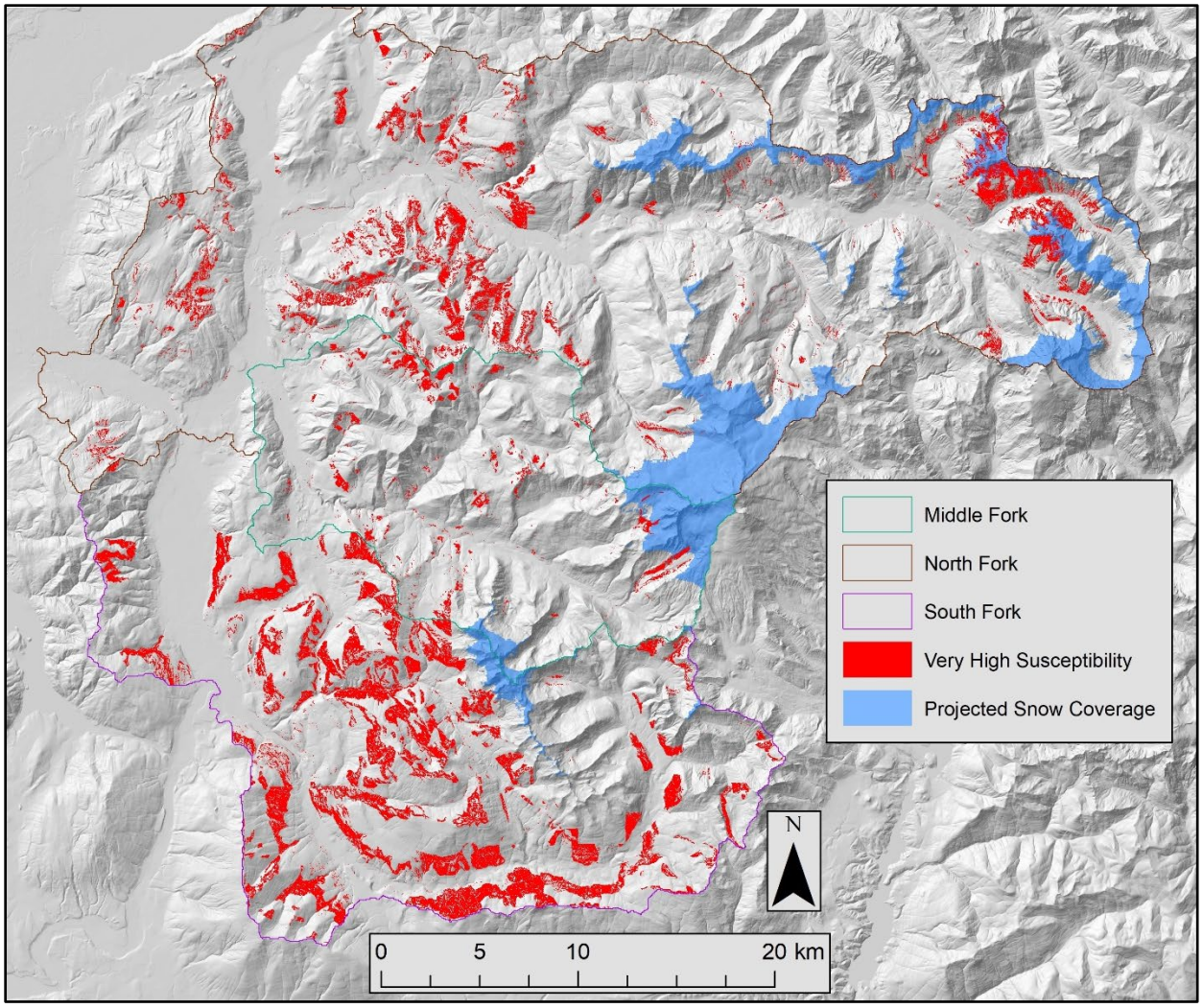

Figure 23. Very high susceptibility associated with the January 2089 storm event, with historical (1995) median snow and the projected 2089 snow coverage displayed within the upper Nooksack basin.

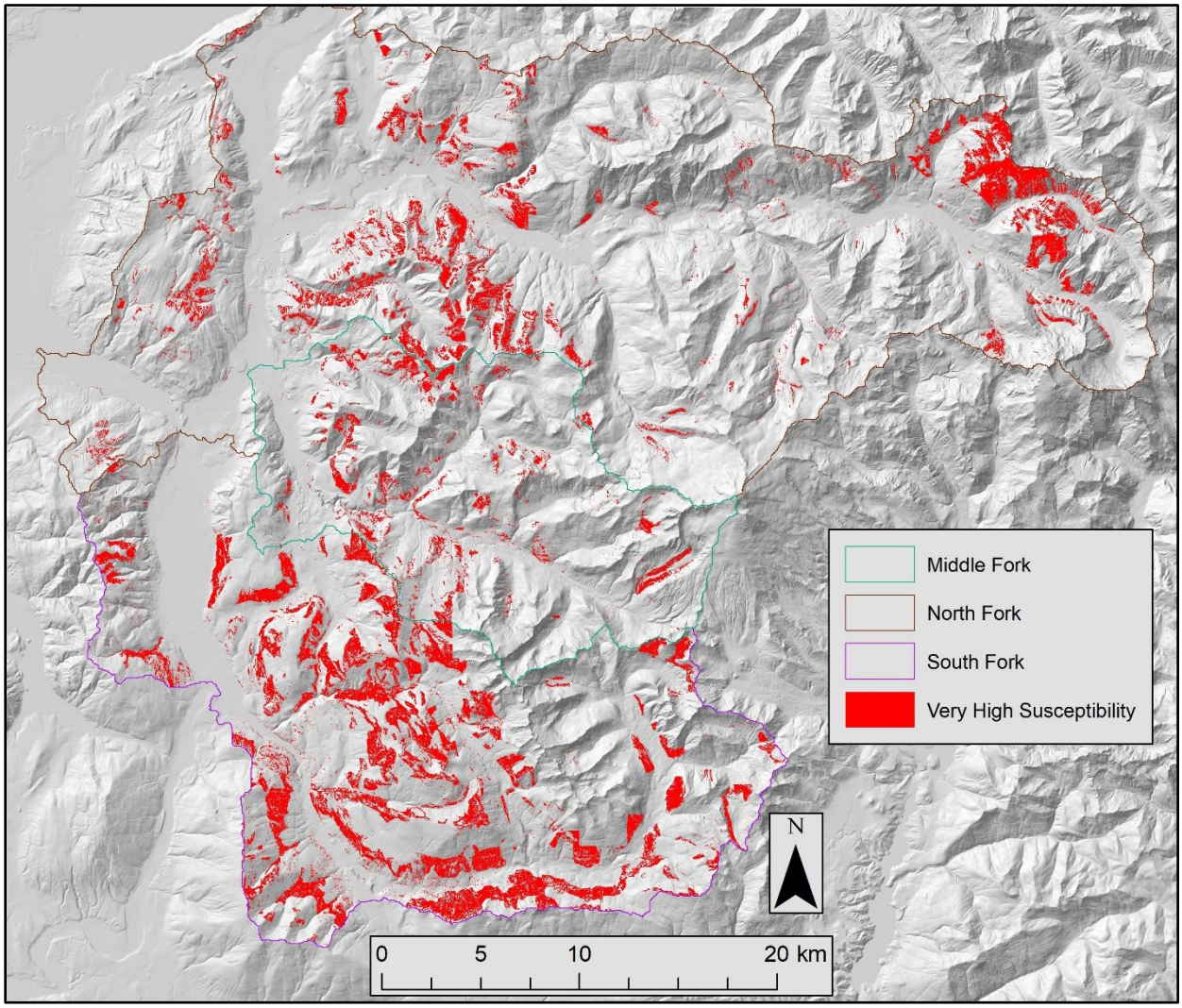

Figure 24. Very high susceptibility associated with the October 2003 storm event displayed within the upper Nooksack basin.

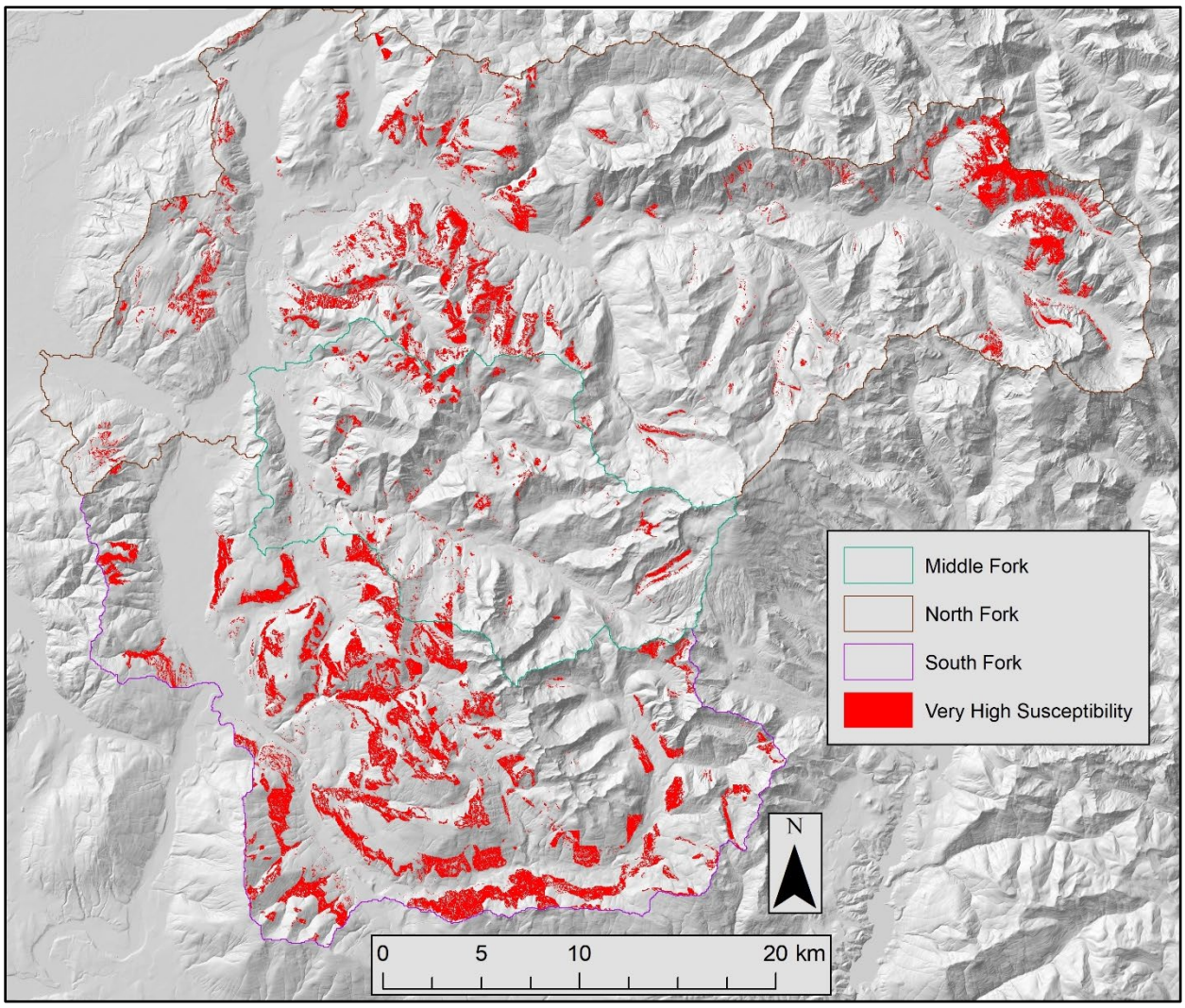

Figure 25. Very high susceptibility associated with the October 2089 storm event displayed within the upper Nooksack basin.

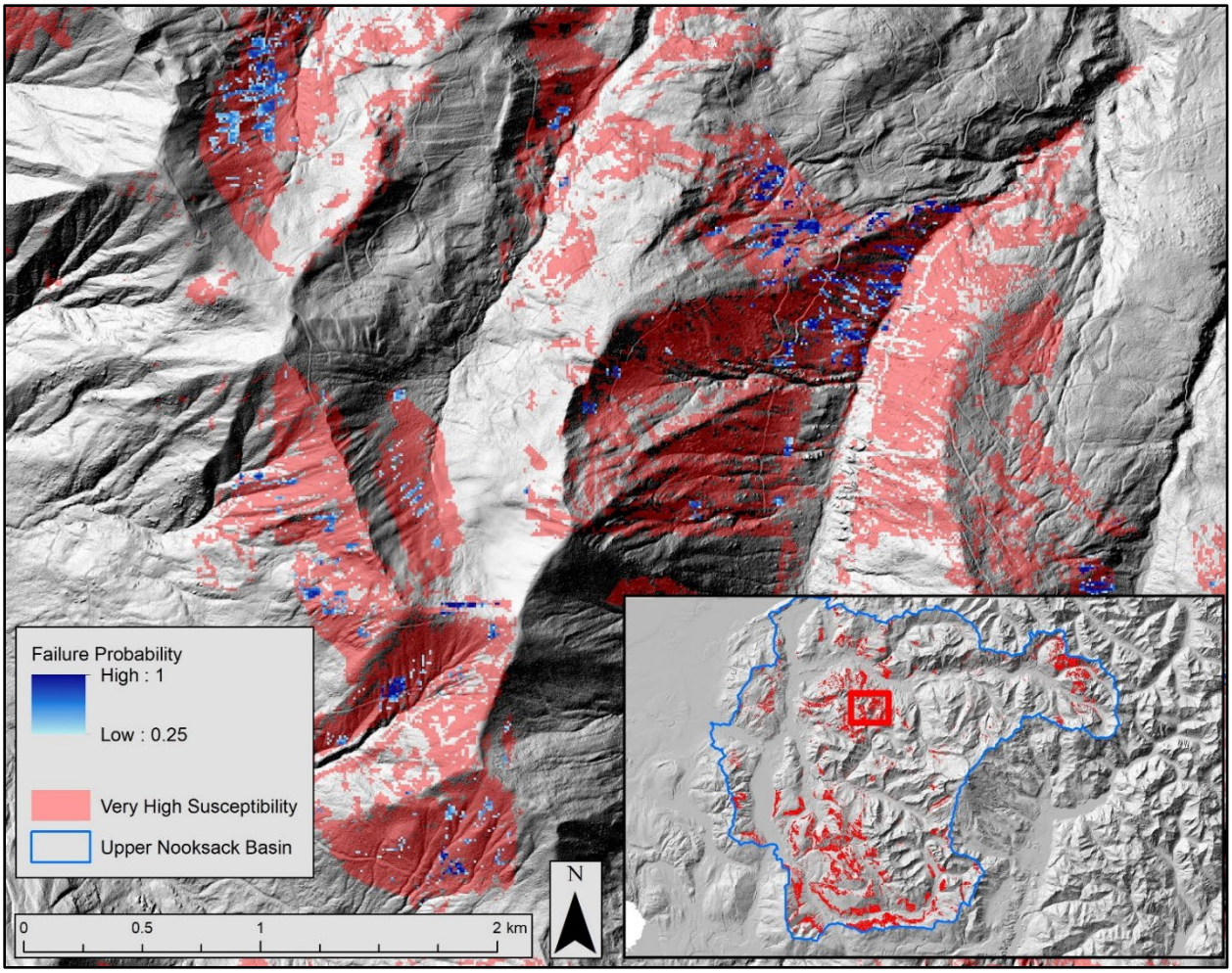

Figure 26. Very high susceptible areas derived from the LSZ map and failure probabilities within the upper Nooksack basin associated with the January 2089 storm event.

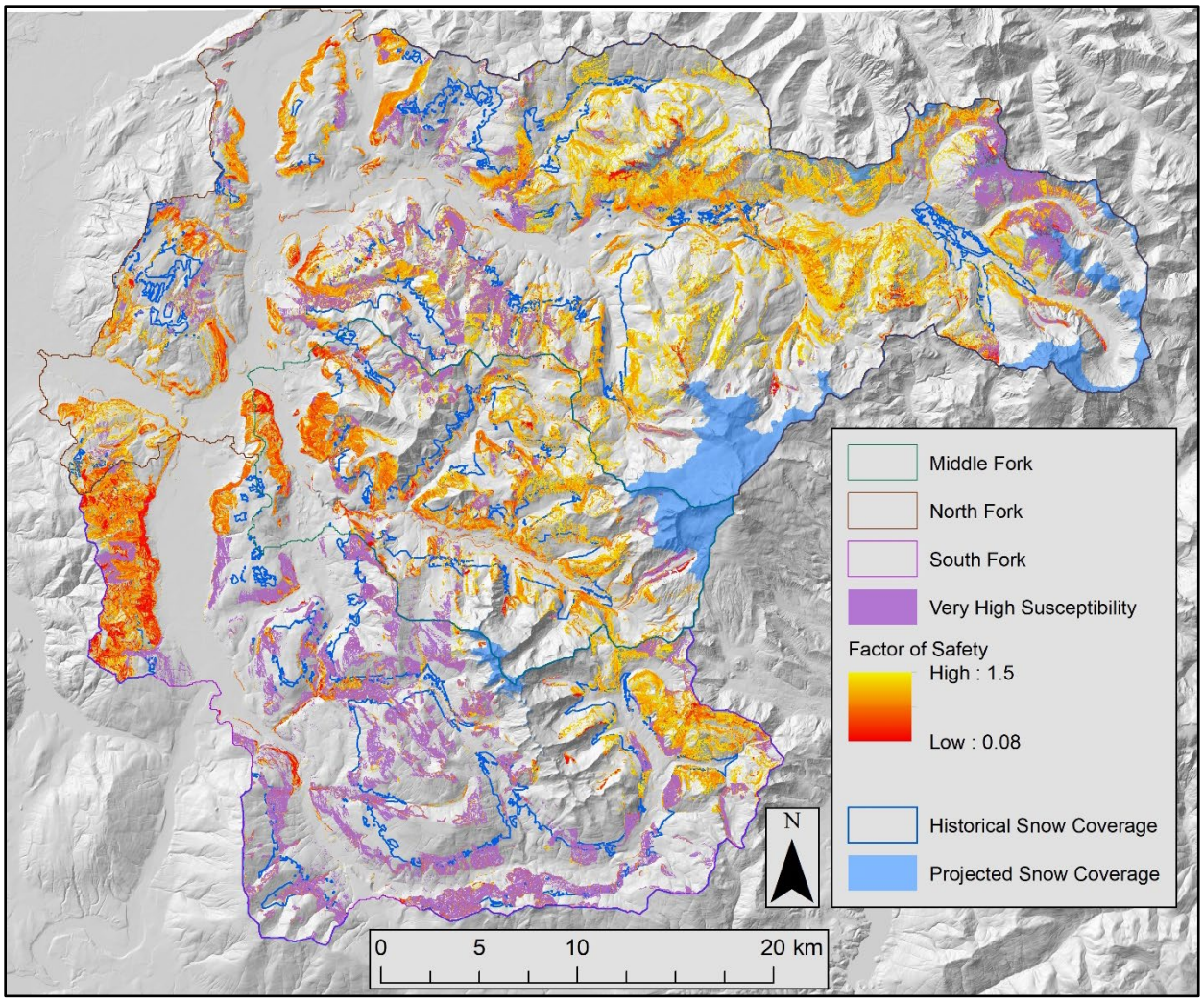

Figure 27. Very high susceptible areas derived from the LSZ map for the December 2096 storm event and susceptible areas derived from static modeling with historical (1995) median snow and the projected 2096 snow coverage displayed within the Upper Nooksack basin.